ISSN 0038-531X

*Russian Original Vol. 58, No. 3, March, 19*

September, 1

SATEAZ 58(3) 177-24. (985)

# SOVIET ATOMIC ENERGY

АТОМНАЯ ЭНЕРГИЯ
(ATOMNAYA ÉNERGIYA)

TRANSLATED FROM RUSSIAN

CONSULTANTS BUREAU, NEW YORK

# SOVIET ATOMIC ENERGY

*Soviet Atomic Energy* is abstracted or indexed in *Chemical Abstracts, Chemical Titles, Pollution Abstracts, Science Research Abstracts, Parts A and B, Safety Science Abstracts Journal, Current Contents, Energy Research Abstracts,* and *Engineering Index.*

Mailed in the USA by Publications Expediting, Inc., 200 Meacham Avenue, Elmont, NY 11003.

**POSTMASTER:** Send address changes to *Soviet Atomic Energy,* Plenum Publishing Corporation, 233 Spring Street, New York, NY 10013.

*Soviet Atomic Energy* is a translation of *Atomnaya Énergiya,* a publication of the Academy of Sciences of the USSR.

An agreement with the Copyright Agency of the USSR (VAAP) makes available both advance copies of the Russian journal and original glossy photographs and artwork. This serves to decrease the necessary time lag between publication of the original and publication of the translation and helps to improve the quality of the latter. The translation began with the first issue of the Russian journal.





Consultants Bureau journals appear about six months after the publication of the original Russian issue. For bibliographic accuracy, the English issue published by Consultants Bureau carries the same number and date as the original Russian from which it was translated. For example, a Russian issue published in December will appear in a Consultants Bureau English translation about the following June, but the translation issue will carry the December date. When ordering any volume or particular issue of a Consultants Bureau journal, please specify the date and, where applicable, the volume and issue numbers of the original Russian. The material you will receive will be a translation of that Russian volume or issue.

Subscription (2 volumes per year)
Vols. 56 & 57: $560 (domestic), $621 (foreign)
Vols. 58 & 59: $645 (domestic), $715 (foreign)
Single Issue: $100
Single Article: $9.50

**CONSULTANTS BUREAU, NEW YORK AND LONDON**

c/b
233 Spring Street
New York, New York 10013

Published monthly. Second-class postage paid at Jamaica, New York 11431.

# SOVIET ATOMIC ENERGY

A translation of *Atomnaya Énergiya*

September, 1985

Volume 58, Number 3 March, 1985

## CONTENTS

# CONTENTS

(continued)

Engl./Russ.



The Russian press date (podpisano k pechati) of this issue was 2/21/1985. Publication therefore did not occur prior to this date, but must be assumed to have taken place reasonably soon thereafter.

# EFFECT OF A BALLAST ZONE ON THE HYDRAULIC STABILITY OF A DIRECT-FLOW STEAM GENERATOR

I. I. Belyakov, M. A. Kvetnyi, and D. A. Loginov

UDC 621.18:039:532.5

Hydraulic stability analysis is an important stage in the design of a direct-flow heat exchanger, in particular a steam generator in a nuclear power plant, as one has to consider the channels in the heating surface and the characteristic working conditions. Two main forms of flow instability occur in a boiling channel: static or aperiodic and dynamic or oscillatory [1, 2]. The numerous factors governing the occurrence of unstable modes include the effects of the mode of heating, about which least is known. The available analytic relationships resemble most experimental results in corresponding to the conditions of radiative or electrical heating, and if one uses them to evaluate the stability in convective heating, there may be substantial quantitative or qualitative errors. When heat is transferred by convection, there is an interaction between the surface temperature and the heat flux, which may, on the one hand, shift the boundaries for unstable modes and on the other may give rise to new mechanisms for instability in the system formed by the hot and cool media.

We have performed an analysis of the hydraulic stability in a direct-flow steam generator heated by liquid sodium, which has shown that puslating states can occur at low loads, which arise by mechanisms different from known ones and which substantially influence these forms of instability. Here we consider this phenomenon, which largely determines the choice of steam-generator working parameters.

The medium in a direct-flow steam generator can be divided into three parts in accordance with the phase state of the working (cooling) medium: the economizer, the evaporator, and the steam superheater. The boundaries between the parts shift in accordance with the mode of operation. When the load on the steam generator falls, there are reductions in the flow rates of the heating medium and the working one and corresponding reductions in the amount of heat transferred, which means that the economizer and evaporator zones tend to shorten and the length of the superheating part increases, since the total surface in the heat exchanger remains constant. Above a certain load, part of the surface is, as it were, switched out of the heat transfer because of temperature reduction in the heating and working media. This part of the surface has small temperature differences and is called the ballast zone. It usually lies in the exit section of the superheating part. In a steam generator employing the countercurrent principle, this form of heating-zone redistribution on load reduction is the most frequently encountered, but not the only one. A certain combination of the temperatures and flow rates of the heating and working media can cause a considerable enlargement of the economizer-evaporator part, while the superheating part shortens. In that case, the ballast zone lies in the region of transition from the economizer to the evaporator. Although the boundaries of the ballast zone are defined only nominally, calculations show that the main section of the ballast zone lies in the economizer part. This is evidently due to a marked increase in the heat-transfer rate in the boiling part. Therefore, this is called the economizer zone.

Figure 1 shows the T–H diagram (T is temperture and H is heating surface), which indicates the limiting possible forms of the heating zones in a direct-flow generator working at low load (with an extensive ballast zone). To demonstrate when the particular forms occur, we consider the heat-balance equations for the evaporator-superheater part for a fixed heating-diagram temperature $T_1$ at the inlet to the generator.

The maximum amount of heat that can be transferred between the media in this part is

$$Q = G(I_1 - I_S), \tag{1}$$

where G is the flow rate of the heating medium and $I_1$ is its enthalpy at $T_1$.

Translated from Atomnaya Énergiya, Vol. 58, No. 3, pp. 155-159, March, 1985. Original article submitted March 20, 1984.

0038-531X/85/5803-0177$09.50  

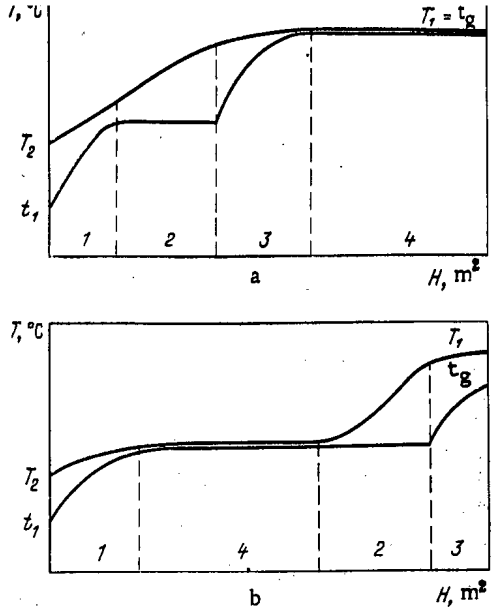


Fig. 1. T–H diagram for a steam generator operting at low power with a ballast zone in the superheating part (a) and in the economizer-evaporator part (b): 1-3) economizer, evaporator, and superheating parts correspondingly; 4) ballast zone.

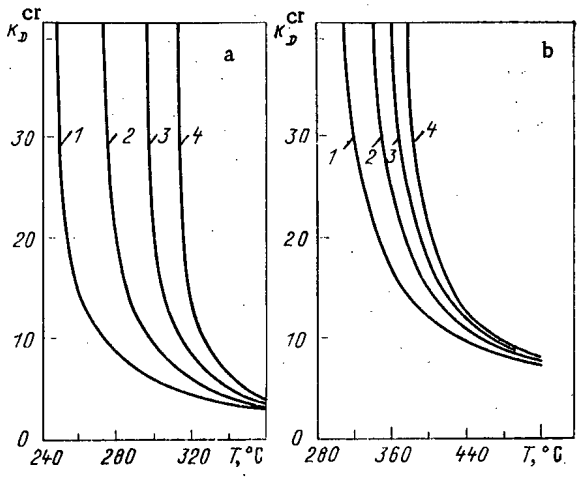


Fig. 2. Dependence of $k_D^{cr}$ on pressure of the working medium p and heating-medium temperature at the inlet to the generator $T_1$; a) heating medium pressurized water, MPa: 1) 3; 2) 5; 3) 7; 4) 9; b) heating medium sodium: 1) 6; 2) 10; 3) 14; 4) 18.

The enthalpy $I_S$ is determined from the saturation temperature of the working medium $t_S$, which is the lower bound to the heating-medium temperature in the evaporator part.

The heat-balance equation for the working medium is

$$Q = D(i_g - i'), \tag{2}$$

where D is the working medium flow rate, while $i_g$ and i' are the enthalpies of the medium at the exit from the generator and of water on the saturation line correspondingly. We equate the right sides of (1) and (2) to get after algebraic transformation that

$$i_g = i' + (G/D)(I_1 - I_S). \quad (3)$$

The temperature of the working medium $t_g$ at the exit from the generator corresponding to $i_g$ may be less than $T_1$; in that case, the temperature of the heating medium tends to $t_S$ in the region of transition from the economizer to the evaporator (near the point i'). This part will also be the zone of small temperature differences, namely the ballast zone (Fig. 1b). The larger $T_1 - t_g$, the shorter the superheating part, and consequently, the larger the ballast zone. As the flow rate of the heating medium increases under otherwise constant conditions, $t_g$ will tend to $T_1$. The superheating part will then enlarge, and at some instant one gets another form of the T–H diagram (Fig. 1a), i.e., the ballast zone transfers from the economizer part to the superheating one. The transition will corresponds to a certain limiting ratio of the flow rates of the heating and working media, which is defined by (3), where the condition is $t_g = T_1$:

$$k_D^{cr} = (G/D)_{cr} = (i_g - i')/(I_1 - I_S), \quad (4)$$

where $i_g$ corresponds to $t_g = T_1$.

It follows from (4) that $k_D^{cr}$ in the general case is dependent on three parameters: the heating-medium temperature at the inlet, the pressure of the working medium, and to a smaller extent the pressure of the heating medium. Figure 2 shows the relationship

$$k_D^{cr} = f(p, T_1),$$

where p is the pressure of the working medium.

If G/D is less than the critical value, there is an economizer ballast zone, while otherwise there is a superheating one.

We consider the mode of operation with an economizer ballast zone subject to the condition that the temperature difference at the outlet is $T_1 - t_g \approx 5°C$; if there is a random rise in $T_1$ by several degrees, $k_D^{cr}$ also alters, and if the condition is initially $G/D < k_D^{cr}$, G/D may exceed the critical value after the temperature rise, so the ballast zone transfers from the economizer part to the superheating one. Therefore, with a given ratio of the flow rates, the displacement of the ballast zone may be caused by temperature change in the heating medium at the inlet.

This means that when the generator works at low load with a ratio of the flow rates close to the critical value, it is possible for the ballast zone to transfer from the superheater part to the economizer one or vice versa in response to random fluctuations in the working parameters (flow rates and temperatures of the heating and working media), i.e., the operation near the point corresponding to the critical ratio with an extended ballast zone is unstable. The displacement of the ballast zone leads to alternating coverage of much of the surface either by two-phase mixture or by superheated steam, as is evident from the forms of T–H diagram in Fig. 1. This causes fluctuations in the tempertures of the generator tubes, as well as a nonstationary heat-transfer crisis, and it may lead to the steam–water mixture being ejected into the collector if the size of the superheating part is small. The latter is dependent on the dynamic characteristics. It is clear that the economizer ballast zone will be of pronounced type for a certain finite temperature difference

$$T_1 - t_g > \Delta t_{min}. \quad (5)$$

One can assume nominally that $\Delta t_{min}$ is 3-5°C, so oscillation is possible in the presence of sign-varying perturbations of finite magnitudes such that (5) is obeyed.

The dynamic characteristics will evidently be determined by the perturbation propagation rate and perturbation duration. If the effect is caused by changes in flow rate in the heating or working media, the perturbation propagation rate will be the speed of sound. The rate of propagation for a temperature perturbation is determined by the transport delay (with allowance for the axial thermal conduction for liquid metal). Therefore, the duration of the transient response and the degree of overshoot may differ substantially between the two cases. As displacement of the ballast zone is related to the conversion of large volumes of liquid to vapor and vice versa, much of the liquid phase may be in the superheated state if the perturbation propagation speed is high, and the process will be accompanied by explosive boiling, which also leads to ejection of the steam–water mixture into the collector.

In a direct-flow generator heated by water under pressure, the ratio of the flow rates usually substantially exceeds the critical value, so in practice modes of operation involving economizer ballast length of the superheater part is then substantially reduced, the

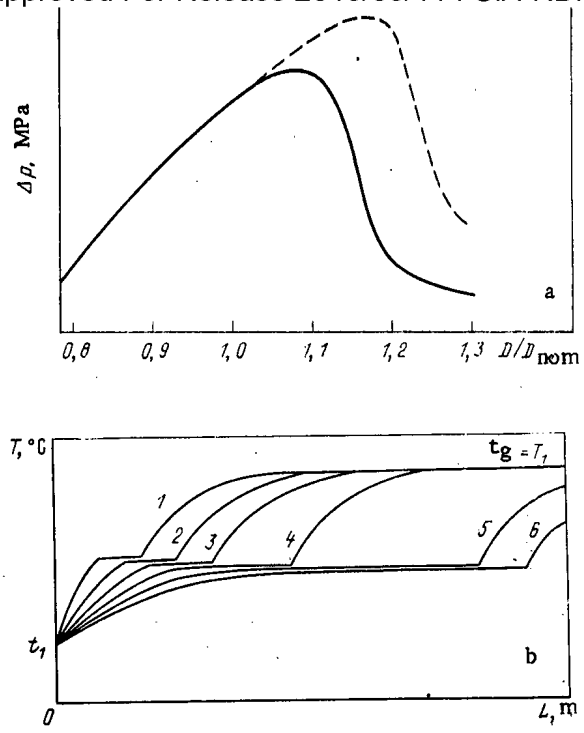


Fig. 3. Effects of ballast-zone displacement on the hydraulic characteristic (a) and temperature distribution in the working medium along the tube as affected by flow-rate change (b): dashed line) heating-medium flow rate G = 1.05 $G_{nom}$; 1-6) values of 0.8, 0.9, 1, 1.1, 1.2, and 1.3 times $D_{nom}$ correspondingly.

pressure difference is reduced, i.e., the hydraulic characteristic has a multivalued region. Figure 3 shows calculations for a direct-flow generator heated by liquid sodium in which the heating surface takes the form of spirals (mean winding diameter 0.15 m) for 25% load [4]. The temperature distribution in the working medium shows that there is a flow-rate range for it (near the critical point) where there is a sharp enlargement in the economizer-evaporator part of the heating surface (Fig. 3b). As the hydraulic resistance in that state is determined by the frictional losses, and the contribution from the other components to the pressure difference is small, the shortening in the superheating part leads to a multiple-valued hydraulic characteristic (Fig. 3a). It is clear that if one evaluates the static stability on existing recommendations at constant heat uptake, one cannot detect the effects of the ballast zone on the hydraulic characteristics.

The steeply falling part on the characteristic makes it difficult to employ any design measures to stabilize the system. For example, when one is choosing throttling devices at the inlet to the heating-surface channels, the necessary local-resistance coefficient may be so large that the generator resistance in the nominal state becomes impermissibly great. In that case, evidently, one should strive not to stabilize the hydraulic characteristic as a whole but to extend the region of single-valued behavior around the working point (with the nominal flow rate for the working medium at the given load). It is then necessary to increase the flow-rate ratio (for example, by altering the flow rate of the heating medium) to provide a large margin from the critical value. Figure 3a (dashed line) shows calculations related to increase in the heating-medium flow rate, which show that an increase of 5% in that rate substantially extends the region of single-valued behavior in the hydraulic characteristic near the working point.

The above results have been obtained from calculations and theoretical analysis of the hydraulic stability at low power. No special experiments have yet been performed on states with unstable ballast zones.

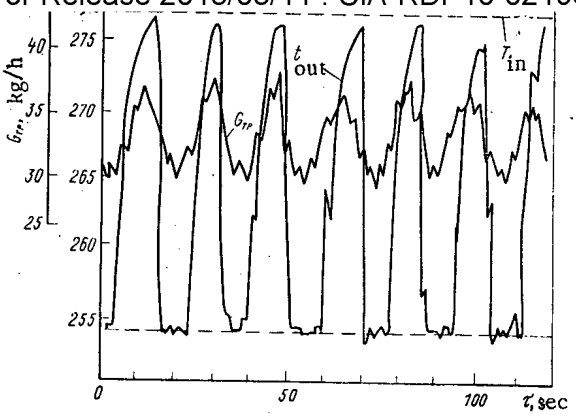


Fig. 4. Character of the pulsations in complete-circuit instability during startup with an elevated sodium flow rate.

However, in [5] results are given from startup conditions in a direct-flow generator heated by liquid sodium.

The generator model involved a Π-shaped scheme and was represented by a section consisting of a seven-tube evaporator module where the medium rises and a separate five-tube superheater section with the working medium descending. In the startup state at constant pressure (startup 5), general instability in the loop was detected (Fig. 4), which was unaffected by the degree of throttling in the water flow rate over the range 0.2-5 MPa. Here the temperature of the medium at the outlet from the superheater tubes $t_{out}$ oscillated in the range between the saturation temperature and the sodium inlet temperature $T_{in}$. Instability was also found with the following working parameters (average ones): heating-medium flow rate G and working-medium rate D of 12,700 and 239 kg/h correspondingly, pressure of working medium 4.2 MPa, sodium temperature at the inlet about 277°C. The data enable one to determine $k_D^{cr}$ which can be compared with the given flow-rate ratio. The calculations show that $k_D^{cr} \approx 56$-57, while the ratio of the flow rates during the experiment was 53-55, i.e., on average it was slightly below the critical value. Features of these nonstationary conditions were that the temperature of the medium varied from $t_S$ and $T_{in}$ and that the amplitude of the fluctuations was independent of the degree of throttling at the inlet, which indicates that the general instability is due to displacement of the ballast zone over the heating surface. Thermal calculations on a generator with a flow-rate ratio close to critical showed considerable numerical instability, which may reflect the unstable position of the ballast zone under real conditions.

Therefore, when one examines the hydraulic stability at low power, it is necessary to consider the possible pulsating states associated with unstable positioning of the ballast zone, which may affect known forms of hydrodynamic flow instability. Therefore, particular attention should be given to choosing the working parameters for startup modes and low loads, in order to eliminate the economizer ballast zone or restrict its occurrence. It is recommended to choose the flow-rate ratio from the condition

$$G/D \geqslant 1.1 k_D^{cr} = \frac{1.1 (i_g - i')}{I_1 - I_S}, \qquad (6)$$

where the generator will work with a stable ballast zone in the superheater. The safety margin in (6) should be chosen to provide an adequate single-valued range in the hydraulic characteristic near the working point.

## LITERATURE CITED

1. I. I. Morozov and V. A. Gerliga, Stability in Boiling Systems [in Russian], Atomizdat, Moscow (1969).
2. F. M. Mitenkov and B. I. Motorov, The Mechanisms of Unstable Processes in Thermal and Nuclear Power Engineering [in Russian], Énergoizdat, Moscow (1981).
3. I. I. Belyakov, M. A. Kvetnyi, D. A. Loginov, and S. I. Mochan, "The static instability of a direct-flow steam generator with convective heating," At. Energ., 56, No. 5, 317-319 (1984).

4. L. N. Artemov, V. N. Grebennikov, V. I. Stogov, and V. B. Belomestnov, "Design ways of improving steam generator reliability by use of modular spiral-design schemes," in: Papers from the Seminar of Comecom Member Countries on Experiences in Developing and Operating Fast-Reactor Steam Generators [in Russian], Dmitrovgrad, 18-21 May (1982), pp. 11-25.
5. G. V. Karetnikov, V. M. Gubanov, A. S. Sokolov, et al., "Recording startup states in a direct-flow sodium steam generator on a model," ibid., pp. 494-505.

# CIRCULATION CHARACTERISTICS OF A NATURAL-CIRCULATION LOOP IN A LARGE-SCALE MODEL FOR A WEAKLY BOILING REACTOR

N. S. Al'ferov, A. S. Babykin, B. F. Balunov, V. V. Vakhrushev, V. S. Kuul', and E. L. Smirnov

UDC 621.039.553.34

There has recently been research on weakly boiling pressurized-water reactors ($x_{co}^{out} < 4\%$) with natural circulation (NC) in the first loop, which has increased interest in the circulation characteristics of NC loops having near-natural heights, hydraulic-resistance coefficients for the individual components, and working parameters (Fig. 1). Table 1 gives the loop characteristics.

The core simulator consisted of 61 uniformly electrically heated pins of diameter 14 mm and height 3 m, which were located in a six-faced jacket with an internal dimension under the keys of 148 mm. The pins were arranged on an equilateral triangle with a pitch of 18.7 mm. Over the height of the simulator there were uniformly placed five spacing grids of honeycomb type with relative transmission cross section $F_{gf}/F_{co} = 0.89$.

The coolant parameters at the inlet to the simulator and at the outlet were as follows: outlet pressure $p_{co}^{out} = 1.7\text{-}2.3$; 3.3-3.8; 4.3-5.0 MPa; water underheating at inlet $(\Delta t_{und})_{co}^{in} = t_n - t_{co}^{in} = 20\text{-}90°C$, and balance weight steam content at outlet $x_{co}^{out}$ from −9 to 3.2%.

In the experiements, the simulator power $N_{co}$ was varied from 0.4 to 1.8 MW, with $q = 50\text{-}230$ kW/m², while the measured water circulation speed in the simulator was from 0.3 to 1.2 m/sec.

To obtain a wider speed range, some of the experiments were performed with the hydraulic resistance increased by a factor 40 not only in the rising column but also in the single-phase

TABLE 1. Geometrical Characteristics and Values of the Reduced Hydraulic Resistance Coefficient $\zeta_{re}$ for the NC Loop in the Model

| Component | Length, m | Cross section, $10^3 \cdot m^2$ | Hydraulic diam., $10^3 \cdot m^2$ | $\zeta_{re}$ |
|---|---|---|---|---|
| Core simulator | 3,0 | 9,35 | 11,7 | 9,4 |
| Simulator for rising part (individual) | 3,5 | 15,0 | 63,7 | 1,28 |
| Simulator for common rising part | 3,7 | 16,5 | 145 | 1,22 |
| Descending part without throttling washer | — | — | — | 2,5 |
| Throttling washer (two forms) | 0,005 | 4,65/2,74 | 77/59 | 6,7/21,8 |
| NC loop | — | — | — | 21,1/36,2 |

Translated from Atomnaya Énergiya, Vol. 58, No. 3, pp. 159-162, March, 1985. Original article submitted January 17, 1984.



0038-531X/85/5803-0182$09.50 

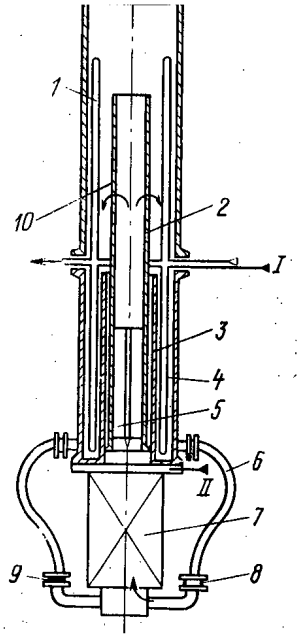


Fig. 1. Design for the experimental NC loop: 1) condenser; 2) common rising part simulator; 3) thermal screen; 4) heat exchanger; 5) simulator for individual rising part; 6) descending bypass tube; 7) core simulator; 8) interchangeable throttle washer; 9) plug; 10) overflow window; I) cooling water inlet; II) air inlet.

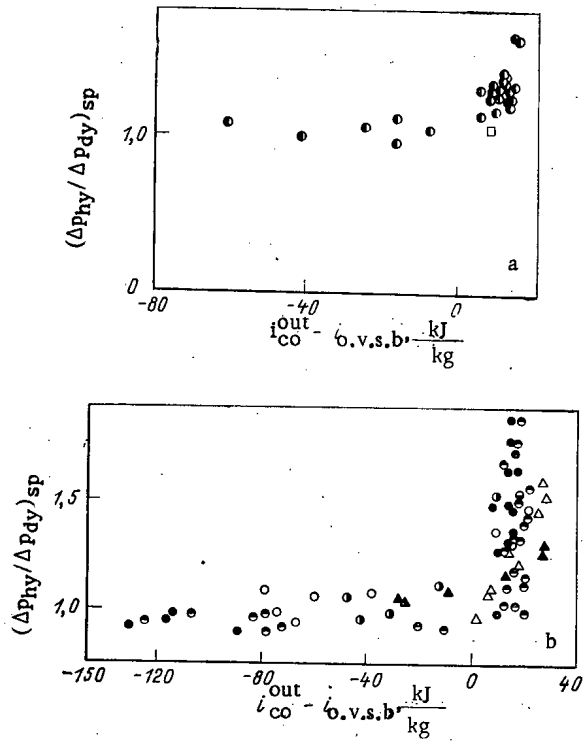


Fig. 2. The $(\Delta p_{hy}/\Delta p_{dy})_{sp} = f(i_{co}^{out} - i_{o.v.s.b.})$ relationship for p = 1.7-5.0 MPa for ρw = 100-110 kg/(m²·sec) (a); ρw = 410-750 kg/(m²·sec) (b); ◐, □, ◒, ●, ◑, ○, △, ▲) q = 25-37; 37-50; 50-75; 75-100; 100-125; 125-150; 150-175; 175-200; 200-225 kW/m² correspondingly.

(water) part of the NC loop. For this purpose, throttling washers were inserted in the lower part of the descending branch in the NC loop (Fig. 1, position 8), and also at the inlet and outlet of the rising prt. Also, the cross section of that part was reduced and the height was reduced somewhat (to 6.1 m). Then the volume of the through section of the part was reduced by a factor 2.81. The experiments were performed in series, in which the through section of the throttling washer was varied. The hydraulic-resistance coefficient in the descending branch of the NC loop varied from 280 to 1130 as referred to the cross section of

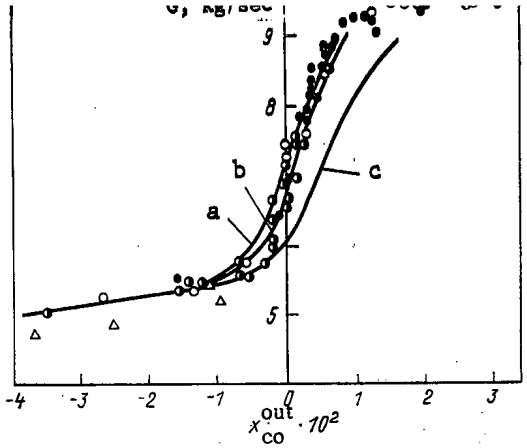


Fig. 3. The $G = f(x_{co}^{out})$ relationship for p = 1.7-2.3 MPa for $N_{co}$ = 1760 (●); 1580-1630 (○); 1430-1560 (◑) and 1110-1340 kW (△); a-c) calculation for p = 2 MPa, $N_{co}$ = 1600 kW: a) calculation of φ [3] and Ψ [1]; b) φ [2, 4] and Ψ [1]; c) φ and Ψ [4].

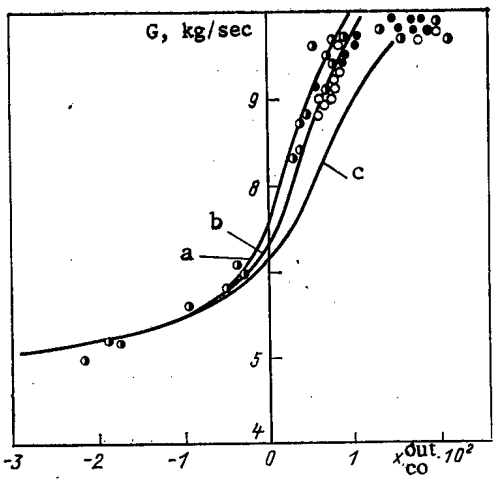


Fig. 4. The $G = f(x_{co}^{out})$: ◑ and ●) $N_{co}$ = 1530 and 1730 kW, p = 3.3-3.8 MPa; ○) $N_{co}$ = 1730 kW, p = 4.3-5.0 MPa (for symbols a-c, see Fig. 3, p = 3.5 MPa).

the core simulator (reduced hydraulic resistance coefficient), which constituted 61-86% of the reduced hydraulic resistance coefficient of the entire NC loop:

$$\zeta_{re}^{a} = F_{co}^{2} \sum_{a} \left[ \left( \lambda_{fr} \frac{l}{d} + \zeta_l \right) \frac{1}{F^2} \right)_i,$$

where $\zeta_{re}^{a}$ is the reduced hydraulic-resistance coefficient for the descending branch of the NC circuit, $F_{co}$ is the cross sectional area of the core simulator, $\lambda_{fr}$ is the frictional coefficient, and $\zeta_l$ is the local hydraulic-resistance coefficient.

This series of experiments was performed with the above ranges in $p_{co}^{out}$, $(\Delta t_{und})_{co}^{in}$, $x_{co}^{out}$, and water circulation speeds of 0.084-0.25 m/sec. With values of $x_{co}^{out}$ close to zero, there was a considerable effect on the circulation characteristics from the nonequilibrium scheme, as recommendations on determining the amount of this had not been thoroughly tested for these conditions.

Programs for the thermohydraulic calculation of stationary NC characteristics were put into correspondence with the experimental data. The algorithm was based on recommendations

for incorporating the effects of equilibrium and nonequilibrium steam [1-5]: for the core simulator (the part generating nonequilibrium steam) we used the recommendations of [2-4], while for the rising part we calculated the true volume steam content $\varphi$ by determining the steam condensation rate in the flow of underheated water by means of [2, 3], while for the equilibrium two-phase flow was calculated by the method of [5].

The program was written in FORTRAN for the ES-1033 computer.

The experiments with the single-phase coolant ($x_{co}^{out} < -2.5\%$) gave satisfactory agreement between the driving head ($\Delta p_{dy}$) and the hydraulic resistance ($\Delta p_{hy}$), where the values were determined from measurements on the flow rate and temperature. The hydraulic resistance coefficients were calculated in accordance with the recommendations of [1, 6, 7].

The discrepancies between $\Delta p_{dy}$ and $\Delta p_{hy}$ were not more than ±8%, while the error in determining the flow rate was ±3% and there is only a small relative density difference in the water $(\rho_{max} - \rho_{min})/(\rho_{max} + \rho_{min}) = 0.02\text{-}0.04$, so this is to be taken as satisfactory.

The small density difference for the coolant in the rising and descending parts of the circuit, as is usual for a single-phase coolant, means that any increase in the flow rate is closely related to the occurrence of nonequilibrium steam in the rising part. To determine the onset of vigorous surface boiling (the start of steam-bubble detachment in the flow of underheated water), we used the formula [6]

$$i' - i_{o.v.s.b.} = 7.5 \frac{q}{\rho w} \left(\frac{q d_h}{r \rho'' \nu'}\right)^{0.08} \left(\frac{W_0 d_h}{\nu'}\right)^{0.2}, \quad (1)$$

where q is the specific heat flux at the heating surface; $\rho$, density; w, speed; r, latent heat of evaportion; $\nu$, kinematic viscosity; and $d_h$, hydraulic diameter; a prime relates to water and two primes to steam, and to check (1) in processing the experimental data for $x_{co}^{out} < 0$, we used the relationship

$$\left(\frac{\Delta p_{hy}}{\Delta p_{dy}}\right)_{sp} = f(i_{co}^{out} - i_{o.v.s.b.}). \quad (2)$$

In determining $\Delta p_{hy}$ and $\Delta p_{dy}$, we neglected the steam in the coolant flow. Vigorous surface boiling corresponds to $(\Delta p_{hy}/\Delta_{dy})_{sp} > 1$, since in this loop the increase in the driving head for the small steam content in the rising part greatly exceeds the relative increase in the hydraulic resistance associated with the steam, i.e., $\Delta p_{hy} = \Delta p_{dy}$ for the NC, which may be written for a two-phase flow as

$$\Delta p_{hy}^{sp} + \delta \Delta p_{hy}^{tp} = \Delta p_{dy}^{sp} + \delta \Delta p_{dy}^{tp},$$

and for $\delta \Delta p_{hy}^{tp} > \delta \Delta p_{dy}^{tp}$ leads to the inequality

$$\Delta p_{hy}^{sp} > \Delta p_{dy}^{sp}.$$

Figure 2 shows the processing results. Formula (1) describes the experimental data accurately throughout the ranges used: p = 1.5-4.0 MPa, q = 25-255 kW/m$^2$, and $\rho w$ = 85-750 kg/m$^2$·sec.

When there is steam in the circuit ($i_{co}^{out} > i_{o.v.s.b.}$), we obtained satisfactory agreement between the calculations and experiment for the flow rate on calculating $\varphi$ in accordance with the recomendations [2-4] and the inhomogeneity coefficient for the two-phase flow $\Psi$ from the recommendations of [1] (Figs. 3 and 4). Less satisfactory results were obtained on calculating $\Psi$ from the recommendations of [4].

## LITERATURE CITED


1. The Normative Method of Hydraulic Calculation for Steam Boilers, Vol. 1, Guideline Statements (TsKTI-VTI) [in Russian], Issue 33, ONTI TsKTI, Leningrad (1973).
2. Yu. S. Molochnikov and G. N. Batashova, in: Advances in Research on Heat Transfer and Hydraulics for Two-Phase Flows in Power Equipment Components [in Russian], Nauka, Leningrad (1973), pp. 79-96.
3. V. I. Plyutinskii and L. L. Fishgoit, "Derivation of the dynamic equation for the steam content in steam-generating channels on the boiling of underheated water," At. Energ., 25, No. 6, 474-479 (1968).
4. V. S. Osmachkin and V. D. Borisov, The Hydraulic Resistance of a Bundle of Heat-Producing Rods in a Flow of Boilng Water [in Russian], Preprint IAÉ-1957, Moscow (1971).

5. L. K. Tikhonenko, [2], pp. 109-119.
6. A. I. Klemin, L. N. Polyanin, and M. M. Strigulin, Thermal and Hydraulic Calculation of Nuclear Reactors and Heat-Engineering Reliability [in Russian], Atomizdat, Moscow (1980).
7. I. E. Idel'chik, Hydraulic Resistance: Physicomechanical Principles [in Russian], Gosénergoizdat, Moscow–Leningrad (1954).

# CORROSION PROTECTION OF A PEARLITIC STEEL IN THE STALLED (SHUTDOWN) AND TRANSIENT (TRANSITORY) REGIMES OF A NUCLEAR POWER SYSTEM

V. V. Prozorov

UDC 620.197.2

The time required for preconditioning the nuclear power plant equipment and systems before putting into operation varies from a few months to a year [1]. All through this period the equipment is under unfavorable corrosive conditions (poor quality of the supplied water, variable thermal and hydrodynamic regimes, exposure to atmosphere, etc.). The existing methods of corrosion protection of the thermal power equipment made from the pearlitic steels must not be mechanically adopted for the nuclear power units because of the intricacy of construction and the more stringent specifications with regard to the corrosion resistance of the materials and the quality of the coolant. In recent years there have been publications [2, 3] indicating high corrosion resistance of the pearlitic steels in high-purity water with oxygen or hydrogen peroxide dosing at a temperature of nearly 300°C. In such studies it has been noted that the corrosion rate of this steel in an oxygen-containing flowing water is less than that of the stainless steels in neutral water [4]. However, the unsolved problem of corrosion in the stalled and the transient regimes sets a limit to the application of the pearlitic steel as a structural material for the nuclear power systems. The use of corrosion inhibitors does not completely solve the problem of equipment protection, since their protective properties become apparent only in a narrow temperature range. Besides this, the necessity of maintaining a high concentration of these inhibitors leads to an increased time loss for their removal (extraction) from the circuit (loop) before changing over to the stationary regime because of the procedure of multiple regeneration (restoration) of the filters. Furthermore, an insufficient concentration of the anodic inhibitors causes pitting corrosion of the metal. Although prior oxidation decreases the corrosion rate, rupture of the protective films occurs in the stalled regimes at a low temperature (20-80°C) leading to pit formation [5]. The corrosion rate of an oxidized metal ranges from 1.4 up to 11.4 g/(m$^2$·day) at 80°C [1, 6].

In spite of numerous publications on the effect of the corrosion inhibitors on the metals in their initial state, there is not enough data on the corrosion behavior of the previously oxidized steels in the inhibitor solutions. The conducted studies revealed a significant difference between the corrosion behavior of the oxidized and the unoxidized pearlitic steels in the inhibitor solutions.

In the present studies on the corrosion of the pearlitic steels in the inhibitor solutions, the "steel 20" specimens were oxidized using:

an ammonium nitrate (5 g/kg) solution at 95°C for a period of 0.5 h at pH = 5.5 and 7.5;

a hydrazine (0.4 g/kg) solution with addition of ammonia to adjust up to pH = 10.5 at 160°C for 16 h; and

an iron nitrate (0.3 g/kg) and hydrogen peroxide (0.05 g/kg) solution at 95°C for 1 h with periodic (supplementary) additions (0.05 g/kg at 15-min intervals) of hydrogen peroxide to the solution [7].

The specimens oxidized in the ammonium nitrate solution at pH = 5.5 were subsequently held in sodium hydroxide solutions (0.16 g/kg) at different temperatures, and also in an aqueous coolant that meets the specification OST 25743-79 ("The coolant quality for the nu-

Translated from Atomnaya Énergiya, Vol. 58, No. 3, pp. 162-166, March, 1985. Original article submitted October 31, 1983.

 0038-531X/85/5803-0186$09.50 

TABLE 1. Protective Inhibitor-Concentration (mg/kg) for the Steel 20 in Desalted Water ( $\varkappa$ = 0.1-0.3 μmho/cm) at 20°C

| Inhibitor | Specimens | | | | |
|---|---|---|---|---|---|
| | machined | oxidized in ammonium nitrate solution at a pH: 5.5 | 7.5 | oxidized by hydrazine-ammoniac method | oxidized in a solution of iron nitrate and hydrogen peroxide |
| $NaNO_2$ | 50 | 5 | 0,3 | 0,1 | 0,02 |
| NaOH | 110 | 10 | 3 | 8 | 0,1 |
| $NH_4OH$ | 115 | 13 | 4 | 15 | 0,15 |
| $K_2CrO_4$ | 70 | 230 | 230 | 200 | 90 |
| $Na_2CO_3$ | 2200 | 600 | 500 | 450 | 300 |
| $Na_4B_4O_7$ | 2000 | 1400 | 1200 | 1100 | 800 |
| $Na_2HPO_4$ | 2500 | 1200 | 1100 | 1000 | 500 |
| $NH_4VO_3$ | 1200 | 250 | 200 | 180 | 80 |
| $(C_2H_5)_3N$ | 800 | 100 | 60 | 55 | 15 |
| $(C_2H_5)_2NH$ | 700 | 80 | 40 | 40 | 10 |
| $K_4[Fe(CN)_6]$ | 1800 | 700 | 700 | 700 | 500 |

TABLE 2. Protective Inhibitor-Concentration (mg/kg) for the Steel 20, Oxidized in Ammonium Nitrate Solution and Held under Different Conditions, in Desalted Water ( $\varkappa$ = 0.1-0.3 μmho/cm) at 20°C

| Oxidized specimens | Inhibitor | | |
|---|---|---|---|
| | $NaNO_2$ | NaOH | $NH_4OH$ |
| Hold in NaOH solution (0.16 g/liter) for a period of 1000 h at a temp., °C: | | | |
| 20 | 0,5 | 4 | 4 |
| 60 | 0,2 | 3 | 3 |
| 200 | 0,03 | 0,7 | 0,8 |
| 270 | 0,001 | 0,3 | 0,5 |
| Hold in the aqueous coolant at the Leningrad NPP at a temp., °C: | | | |
| 160 (8950 h) | 0,4 | 3 | 3 |
| 270 (8030 h) | 0,2 | 2 | 2 |

TABLE 3. Protective Inhibitor-Concentration (mg/kg) for the Steel 20 in Desalted Water ( $\varkappa$ = 0.1-0.3 μmho/cm) at Different Temperatures

| Inhibitor | Surface condition | Temp., °C | | | | | | |
|---|---|---|---|---|---|---|---|---|
| | | 20 | 50 | 100 | 150 | 200 | 250 | 300 |
| $NaNO_2$ | Not oxidized | 50 | 200 | 400 | — | — | — | — |
| | Oxidized in $NH_4NO_3$ | 5 | 7 | 12 | 18 | 25 | 40 | 45 |
| NaOH | Not oxidized | 110 | 170 | 230 | — | — | — | — |
| | Oxidized in $NH_4NO_3$ | 10 | 15 | 35 | 75 | 105 | 115 | 105 |

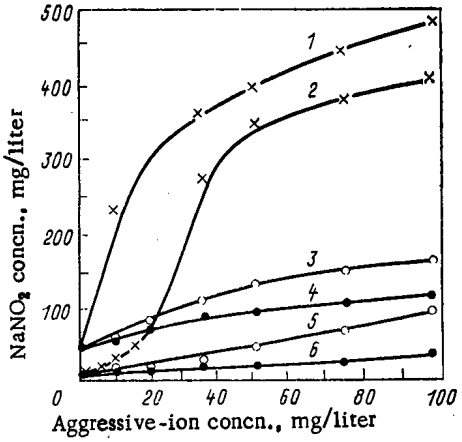


Fig. 1. Dependence of the protective concentration of sodium nitrite on the aggressive-ion concentration for the steel 20 at 20°C: 1, 3, 4) unoxidized specimens; 2, 5, 6) specimens oxidized in ammonium nitrate solution: ×) $Na_2SO_4$; ○) NaCl; ●) $NaNO_3$. The area above the respective curves represents the protective zone (total suppression of corrosion), and the area below the curves represents corrosion zone (corrosive failure of specimens).

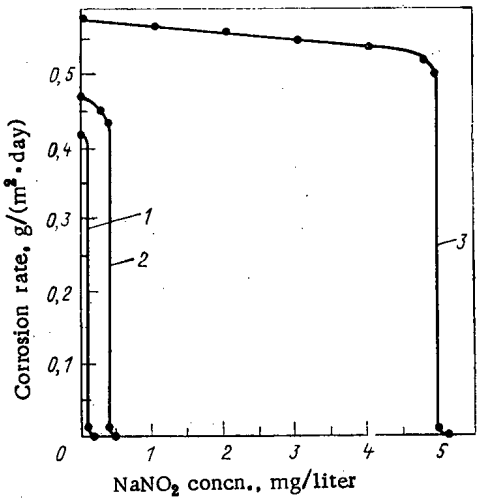


Fig. 2. Effect of sodium nitrite concentration on the corrosion rate of the oxidized steel 20 in desalted water at 20°C for 100 days: oxidized by the hydrazine-ammoniac method (1), in ammonium nitrate solution at pH = 7.5 (2) and pH = 5.5 (3).

clear power plants with the RBMK type reactors, and the methods of ensuring and controlling the quality") in a deaerator at 160°C for a period of 8950 h and in a circuit of multistage forced circulation (at 270°C) for 8030 h, and the specimens were then subjected to the corrosion tests. We determined the corrosion rate of the specimens in the solutions over a period of 100 days and the minimum protective inhibitor-concentration at which complete suppression of corrosion is achieved (i.e., at which there is no change in the specimen weight and the iron content in the solution does not increase). In order to determine the minimum

TABLE 4. Corrosion Rate of the Steel 20, Oxidized in Ammonium Nitrate Solution (pH = 5.5), in Desalted Water ( $\varkappa$ = 0.5-0.8 μmho/cm) and $NaNO_2$ Solutions at 60°C for 10 Days

| Inhibitor concn., mg/liter | Flow rate, m/sec | General corrosion rate, g/(m² · day) | Nature of corrosion |
|---|---|---|---|
| 0 | 0 | 0,51 | Pitting |
| 0 | 1—3 | 0,22 | Pitting |
| 1 | 0 | 0,44 | Pitting |
| 1 | 1—3 | 0,04 | Uniform |
| 5 | 0 | 0,32 | Pitting |
| 5 | 1—3 | ⩽0,005 | Uniform |
| 10 | 0 | 0,01 | Uniform |
| 10 | 1—3 | ⩽0,005 | Uniform |

concentration, the experimental specimens were immersed in the solutions having different inhibitor concentrations, and were held for 15 days. An abrupt transition to complete suppression of corrosion could be observed visually.

The data of Table 1 shows that prior oxidation of the steel sigificantly deceases the protective concentration of all the inhibitors with the exception of chromates in that the nitrites and hydroxides of alkali metals possess the best protective properties. The protective concentration of these inhibitors depends on the method of oxidation, and can be sharply reduced as compared to that used in case of the unoxidized metal (Tables 1 and 2). The most effective protection of the oxidized pearlitic steel is obtained using a solution of the inhibitor in desalted (salt-free) water. The presence of activating ions in the solution necessitates an increase in the protective inhibitor concentration. The sulfate ions present in the inhibitor solutions are particularly aggressive with respect to the pearlitic steel (Fig. 1).

We underline the fact that while the corrosion of a nonpassivated steel can be totally suppressed up to a temperature of 100°C using the inhibitors, we observe total suppression of corrosion of an oxidized steel in the alkali metal nitrite and hydroxide solutions in the entire temperature range of our study (from 20 up to 300°C). The minimum inhibitor concentration required for suppressing corrosion increases with increasing temperature in that the protective concentration is considerably higher for an unoxidized steel as compared to an oxidized steel (Table 3).

The laboratory bench tests showed that the effectiveness of the inhibitor-aided corrosion-protection of the oxidized steel is higher in the dynamic regime than in the static regime. A smaller inhibitor concentration is required for achieving complete suppression of corrosion in the dynamic regime. Corrosion of the specimens is considerably slowed down, and is uniform even when the inhibitor concentration is insufficient for complete suppression of corrosion (Table 4).

When the oxidized specimens are held under static conditions in desalted water or at an insufficient inhibitor concentration, rupture of the oxide films occurs with subsequent loss of their protective properties in that the oxide layer is completely destroyed at some places within the very first 100 h.

In the absence of variations in the temperature and the quality of desalted water, the corrosion process is completely suppressed at a particular inhibitor concentration that depends on the method of oxidation (Fig. 2).

Our studies showed that during the process of holding the specimens in solution having an inhibitor concentration sufficient for suppressing corrosion, the protective properties of the oxide films are gradually improved, and, in particular, suppression of corrosion is observed at a smaller inhibitor concentration (see Table 2) in that an increased solution temperature enhances this improvement. Some improvement in the protective properties of the films is also observed when the "steel 20" specimens, subjected to prior oxidation in ammonium nitrate solution, are held in a flowing aqueous coolant that meets the property specification OST 95743-79. This can be attributed to the high quality of water, the increased temperature, and the corresponding stable passive state of the steel.

Electron microscopic study of the film morphology established that recrystallization of the primary oxide films occurs when the oxidized specimens are held in sodium nitrite (60 mg/kg) and sodium hydroxide (160 mg/kg) solutions at 60°C (i.e., at an inhibitor concentration sufficient for suppressing corrosion). The inhomogeneities of microrelief act as the nucleation sites for recrystallization. With increasing holding period, recrystallization progressively assumes a more general character. During this process, the protective properties of the oxide film are improved (see Table 2). X-ray structural analysis did not reveal any new phases except magnetite.

It is known that at high temperatures the trivalent iron oxide becomes a thermodynamically stable phase [8], and indeed, electron diffraction studies revealed the presence of maghemite (which improves the protective properties of the oxide films) on the surface of the specimens held in NaOH solution (160 mg/kg, 270°C) besides magnetite. In the oxidized specimens held in $NaNO_2$ solution (60 mg/kg) at 270°C, besides magnetite, an insignificant quantity of hematite is present on the specimen surface. In view of the fact that at a temperature exceeding 100°C there occurs partial dissociation of nitrites according to the reaction [9]

$$2NaNO_2 + H_2O \rightleftarrows 2NaOH + {}^1/_2O_2 + N_2,$$

the excess amount of the liberated oxygen can lead to a more complete conversion (rearrangement) of magnetite into hematite which does not have a spinel structure, and in pure form, it does not possess the protective properties. Thus, in case sodium nitrite is used, there is an upper limit of concentration (70 mg/kg) above which one cannot achieve complete suppression of corrosion of an oxidized steel at a temperature exceeding 100°C. Hematite forms even when the specimens are held in NaOH solution if there is a considerable amount of oxygen in the system.

At a temperature above 100°C the upper limit of protective concentration of sodium hydroxide was found to be 200 mg/kg. Corrosion reappears at higher concentrations. The interaction of the oxide films with the alkali produces dissolvable ferrites. In this case, the dissolution process assumes a localized character.

Thus, when the oxidized steel is held in the inhibitor solutions, complex physicochemical processes occur which change the structure and the phase constitution of the oxide films, and thereby, affect their protecting ability. It follows from the data presented here that the protective inhibitor concentration depends on the method of passivation, the temperature, the quality of desalted water, the flow rate, and the duration of holding the steel in the solution. The significant reduction in the protective concentration of the dissolvable nitrites and hydroxides and the widened temperature range in which these inhibitors exhibit protective properties permit us to recommend them for protecting the previously oxidized power-equipment in the stalled and the transient regimes. As the nuclear power system attains the stationary state, the oxide films become dense (thick) and water becomes free from aggressive ions, owing to which the inhibitor can be withdrawn from the circuit (when there is total suppression of corrosion), and at this stage, it is advisable to introduce specific doses of oxygen or hydrogen peroxide into the system. When the nuclear power system is shut down for maintenance, it is essential to add the corrosion inhibitor again for avoiding the rupture of oxide films under the stalled conditions. In this case, the inhibitor concentration required for complete suppression of corrosion, even under the conditions of depressurization and saturation of the system with oxygen and carbon dioxide, can be considerably reduced as compared to the concentration required for the corrosion protection of a nonpassivated metal.

The choice of the inhibitors depends on the specific service conditions of the equipment: the ionizing radiation, tightness of the system, the reactor type, the temperature, the presence of other structural materials in the system, etc.

Among the examined methods of oxidizing the pearlitic steel, using ammonium nitrate solution is not the best because of the formation of a significant quantity of insoluble ferric oxide lepidocrocite compounds which contaminate the circuit during the process of conditioning the equipment. The hydrazine-ammoniac oxidation method requires a high temperature (above 140°C). Hydrazine hydrate is fire hazardous and toxic. Treating the pearlitic steel with iron nitrate and hydrogen peroxide solution does not suffer from these shortcomings and the oxide films formed possess better protective properties.

The given technological solution formed the main postinstallation chemical treatment of the internal surfaces of the condensate supply channel of the fourth block of the Chernobyl'sk Nuclear Power Plant. The equipment and the channel piping (surface area greater than 5000 $m^2$ and volume 1200 $m^3$) made from the pearlitic steel were treated with nitric acid solution of 60 mg/kg concentration at 95°C for 4 h (during this treatment iron nitrate forms in the system). Thereafter, we introduced hyrogen peroxide (5 mg/kg) into the circuit and continued the treatment for 1 h at the same temperature. After water treatment in the ion-exchange filters until an electrical conductivity of 0.6-0.7 μmho/cm is obtained, sodium nitrite was added to the system up to a concentration of 16-18 mg/kg. On treating with nitric acid and hydrogen peroxide, dense black-colored oxide layer, strongly adhering to the metal, formed on the internal surfaces of the equipment of the condensate supply channel. Analysis of the phase constitution using nuclear γ-resonance spectrometry (NGRS) established that this layer totally consists of magnetite. Subsequent conservation of the channel surfaces by sodium nitrite was found to be effective. The circuit was emptied after 6 days. During this period the iron concentration in water, measured at all the sampling points of the channel, remained at the original level. During the postinstallation start-up period, it took only 18 h to obtain the specified quality indices of the coolant when operating at 150-260 MW.

Thus, we can recommend prior oxidation and the subsequent use of desalted water with dissolvable nitrite and hydroxide additions for working out the corrosion protection technology in the stalled and the transient regimes of the equipment of the nuclear power systems made from a pearlitic class steel. Such a technology permits wider application of this steel in lieu of the scarce and costly austenitic stainless steels of the 18-10 type.

## LITERATURE CITED

1. P. G. Krutikov nd V. M. Sedov, Water-Chemical Treatments during the Start-up of Nuclear Power Plants [in Russian], Énergoizdat, Moscow (1981).
2. K. A. Nesmeyanova, E. B. Matskevich, and V. G. Kasatkina, in: Proceedings of the III Internat. Congress on Corrosion of Metals [Russian translation], Vol. IV, Mir, Moscow (1966), p. 278.
3. Ya. N. Kolotyrkin et al., in: Corrosion of Rector Materials [in Russian], Atomizdat, Moscow (1960), p. 29.
4. E. P. Anan'ev, Nuclear Systems in Energetics [in Russian], Atomizdat, Moscow (1978).
5. V. N. Belous, A. I. Gromova, and V. V. Gerasimov, Nuclear Science and Technology, Reactor Physics and Engineering Series [in Russian], Issue 3 (3) (1978), p. 43.
6. V. N. Belous, A. I. Gromova, V. V. Gerasimov, et al., ibid., p. 51.
7. V. V. Prozorov, Inventor's Certificate No. 1027284, Byull. Izobret., No. 25, 105 (1983).
8. R. Biernat and R. Robins, Electrochem. Acta, 17, 1261 (1972).
9. P. A. Akol'zin, Corrosion of Metals in Steam Generators [in Russian], Leningrad (1957).

# IMPLICIT METHOD OF SOLVING MASS-TRANSFER EQUATIONS IN THE VARIABLES VELOCITY–VORTICITY

M. P. Leonchuk, Z. V. Sivak, and Yu. E. Shvetsov

UDC 532.54

In the theortical investigation of heat and mass transfer in a nuclear reactor there has recently been steadily increasing use of the porous-body model [1-3]. The efficiency of this approach is especially apparent in calculating the fields of the heat-carrier velocity and temperature in geometrically complex objects consisting of several elements differing in their hydraulic and thermophysical properties. The motion of a viscous incompressible liquid in an anisotropic porous body is described by the continuity equation

$$\frac{\partial (W_l \varepsilon)}{\partial x_l} = 0 \tag{1}$$

and the equation of motion [1]

$$\frac{\partial W_m}{\partial t} + \left(W_l \frac{\partial}{\partial x_l}\right) W_m = -\frac{1}{\rho} \frac{\partial P}{\partial x_m} - \Lambda_{ml} W_l + \left(\frac{\partial}{\partial x_l} \nu \frac{\partial}{\partial x_l}\right) W_m, \tag{2}$$

where $\ell$, m = 1, 2, 3 (summation is performed over $\ell$).

In the particular case when liquid flow in an unenclosed volume is considered with a porosity of the medium $\varepsilon = 1$ and there are no volume forces, i.e., $\Lambda_{m\ell} = 0$, this system of equations transforms to the Navier–Stokes system of equations, numerical solution of which is associated with a series of well-known difficulties. However, if volume friction forces predominate over viscous and inertial forces, the structure of the solution of Eqs. (1) and (2) is considerably simplified. In the limiting case, the steady problem may be reduced to the solution of a single quasiliner equation of parabolic type. Numerical solution of this problem is possible, as a rule, using fewer iteration than for the Navier–Stokes problem. However, the problem of constructing a more effective algorithm remains pressing in this case too.

One widespread approach to solving the system of fluid-dynamic equations is to pass to new functions: the current function $\psi$ and the vorticity w. The principal advantage of methods based on the use of these functions is that the continuity equation is automatically satisfied at each step of the iterative process at internal points of the calculation region. In a series of problems, this ensures a benefit in terms of the rate of convergence. However, solving the problem in ($\psi$, w) variables entails specifying boundary conditions for the vorticity at a solid wall absent in the physical formulation of the problem. The rate of convergence of the numerical method is found to depend on the method of specifying the boundary condition for the vorticity and the accuracy of its approximation [4]. This deficiency is eliminated by numerical methods of solving the system of Navier–Stokes equations in the "natural" variables velocity–pressure. In addition, in solving three-dimensional problems in the natural variables, it is required to solve fewer differential equations. Finally, they are more simply generalized to the case of inhomogeneous calculation regions. The method of solving the equations of the porous-body model in the variables velocity–vorticity which is outlined below combines the advantages of both approaches. The method has a high rate of convergence thanks to the precise satisfaction of the continuity equation at each iteration and has practically absolute stability, since it is based on the use of implicit difference approximations of the equations being solved.

In r–z geometry, after introducing the vorticity

$$\omega = \frac{\partial u}{\partial r} - \frac{\partial v}{\partial z} \tag{3}$$

Eqs. (1) and (2) may be reduced to the form

Translated from Atomnaya Énergiya, Vol. 58, No. 3, pp. 166-170, March, 1985. Original article submitted July 22, 1984.

 0038-531X/85/5803-0192$09.50 

$$\frac{\partial rv}{\partial z}+\frac{\partial ru}{\partial z}=0^{*}; \tag{4}$$

$$\frac{\partial \omega}{\partial t}+\frac{\partial v\omega}{\partial r}+\frac{\partial u\omega}{\partial z}=-\frac{\partial}{\partial r}(\Lambda_z u)+\frac{\partial}{\partial z}(\Lambda_r v)+\nu\left\{\frac{\partial}{\partial r}\left(\frac{1}{r}\frac{\partial r\omega}{\partial r}+\frac{\partial^2\omega}{\partial z^2}\right)\right\}. \tag{5}$$

The diagonal components $\Lambda_r$ and $\Lambda_z$ of the tensor of volume frictional forces are not equal in the general case, and depend on the velocity vector; the other components are assumed to be zero. On the external contour $\Gamma$ of the calculation region ($R_0 \leqslant r \leqslant R_I$, $0 \leqslant z \leqslant H$), the radial v and axial u velocity components

$$v|_\Gamma = v_\Gamma(r, z); \quad u|_\Gamma = u_\Gamma(r, z) \tag{6}$$

or else their derivatives are specified. The initial conditions are also specified for velocity components

$$u|_{t=0} = u_0(r, z); \quad v|_{t=0} = v_0(r, z), \tag{7}$$

and then the initial conditions for w are calculated using Eq. (3).

To obtain the difference analog of the system in Eqs. (3)-(5), the calculation region is overlaid with a basic grid with integer indices i and k (i = 0, 1, ..., I; k = 0, 1, ..., K) and two auxiliary grids with semiinteger values of one of the indices $i \pm 1/2$ or $k \pm 1/2$ (Fig. 1). In the general case, the steps of the basic grid over the radius $\Delta r_{i+1/2}$ and over the height $\Delta z_{k+1/2}$ depend on the coordinate. Values of the vorticity are assigned to points of the basic grid $\omega_{ik}$, and the values of the velocity components $u_{i\pm1/2\,k}$ and $v_{ik\pm1/2}$ are calculated at points of the corresonding auxiliary grid.

Integrating Eq. (4) with respect to the cell of the basic grid, a different form of the continuity equation is obtained

$$u_{i-1/2\,k} = u_{i-1/2\,k-1} - \frac{2\Delta z_{k-1/2}}{r_i^2 - r_{i-1}^2}(r_i v_{i\,k-1/2} - r_{i-1} v_{i-1\,k-1/2}), \tag{8}$$

where i = 1, 2, .., I; k = 1, 2, ..., K.

The subsequent calculations demand an expression for the axial velocity component at the next point on the radius

$$u_{i+1/2\,k} = u_{i+1/2\,k-1} - \frac{2\Delta z_{k-1/2}}{r_{i+1}^2 - r_i^2}(r_{i+1} v^j_{i+1\,k-1/2} - r_i v_{i\,k-1/2}). \tag{9}$$

The superscript j denotes that the value of the given quantity is taken at the preceding iteration. For the sake of simplicity, the index (j + 1) is omitted; i = 0, 1, 2, ..., I − 1; k = 1, 2, ..., K.

The difference expression for Eq. (3) defining the vorticity at internal points of the region is written in the following form, with $v_{ik+1/2}$ isolated:

$$v_{i\,k+1/2} = v_{i\,k-1/2} + \frac{\Delta z_k}{\Delta r_i}(u_{i+1/2\,k} - u_{i-1/2\,k}) - \Delta z_k \omega_{ik}, \tag{10}$$

$$\Delta z_k = (\Delta z_{k+1/2} + \Delta z_{k-1/2})/2;$$

$$\Delta r_i = (\Delta r_{i+1/2} + \Delta r_{i-1/2})/2,$$

$$i = 1, 2, \ldots, I-1; \quad k = 1, 2, \ldots, K-1.$$

In determining the vorticity at the boundaries of the region the first-order approximation at a halfstep from the boundary is used. For example, when z = 0

$$\omega_{i0} = \frac{u_{i+1/2\,0} - u_{i-1/2\,0}}{\Delta r_i} - \frac{2(v_{i\,1/2} - v_{i0})}{\Delta z_{1/2}}; \tag{11}$$

$$i = 1, 2, \ldots, I-1.$$

Within the framework of the method outlined, the accuracy of the approximation at the boundaries of the region may be increased to second order without significant complication of the algorithm if Eq. (11) for the vorticity is replaced by the expression

$$\omega_{i0} = \frac{8v_{i0} - 9v_{i\,1/2} + v_{i\,3/2}}{3\Delta z_{1/2}} + \frac{u_{i+1/2\,0} - u_{i-1/2\,0}}{\Delta r_i}.$$

*To simplify the calculations, ε = const and ν = const is assumed here and below.

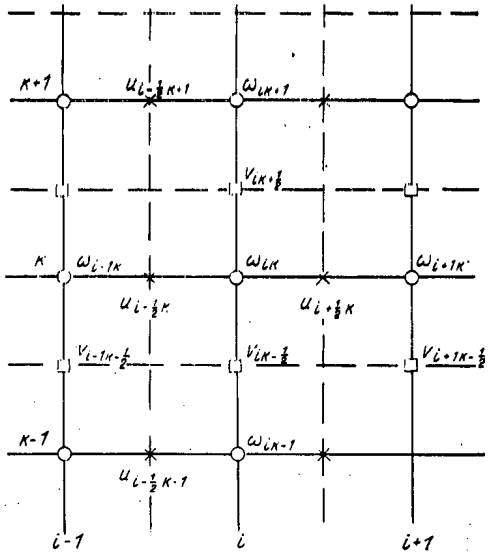


Fig. 1. Calculation grid.

Analogous relations determine the vorticity in cells adjacent to the other boundaries.

For a difference representation of the vorticity-transfer equation, Eq. (5) is integrated in the vicinity ($r_{i-1/2} < r < r_{i+1/2}$; $z_{k-1/2} < z < z_{k+1/2}$) of each internal point over the element drdz. After calculating the integrals, a conservative difference scheme with a near-second-order approximation with respect to the spatial variable is obtained:

$$\frac{\omega_{ik}-\omega_{ik}^{t}}{\Delta t}+\frac{1}{\Delta r_i}\left\{v^j_{i+1/2\,k}\begin{bmatrix}\omega_{ik}\\ \omega_{i+1\,k}\end{bmatrix}-v^j_{i-1/2\,k}\begin{bmatrix}\omega_{i-1\,k}\\ \omega_{ik}\end{bmatrix}\right\}+\frac{1}{\Delta z_k}\left\{u^j_{i\,k+1/2}\begin{bmatrix}\omega_{ik}\\ \omega_{ik+1}\end{bmatrix}-u^j_{i\,k-1/2}\begin{bmatrix}\omega_{ik-1}\\ \omega_{ik}\end{bmatrix}\right\}=\frac{\nu}{\Delta r_i}\times$$

$$\times\left\{\frac{r_{i+1}\omega_{i+1\,k}-r_i\omega_{ik}}{\Delta r_{i+1/2}r_{i+1/2}}-\frac{r_i\omega_{ik}-r_{i-1}\omega_{i-1\,k}}{\Delta r_{i-1/2}r_{i-1/2}}\right\}+\frac{\nu}{\Delta z_k}\left\{\frac{\omega_{i\,k+1}-\omega_{ik}}{\Delta z_{k+1/2}}-\frac{\omega_{ik}-\omega_{i\,k+1}}{\Delta z_{k-1/2}}\right\}+$$

$$+\frac{1}{\Delta z_k}\{\Lambda^j_{r_{i\,k+1/2}}v_{i\,k+1/2}-\Lambda^j_{r_{i\,k-1/2}}v_{i\,k-1/2}\}-\frac{1}{\Delta r_i}\{\Lambda^j_{z_{i+1/2k}}u_{i+1/2\,k}-\Lambda^j_{z_{i-1/2\,k}}u_{i-1/2\,k}\}. \qquad (12)$$

Here the mean velocity values are determined by linear interpolation over four adjacent values of the corresponding velocities from the preceding step of the iteration (for example, $v_{i+1/2k}$ is determined in terms of $v^j_{i\pm1k\pm1/2}$). This means linearization of the vorticity-transfer equation at each step of the iterative process. The upper value in the square brackets is taken when the mean velocity preceding the brackets is positive and the lower value when this mean velocity is negative.

In solving the difference system in Eqs. (8), (10), and (12), the following method of longitudinal-transverse "fitting" is employed. In fitting along the coodinate z, the variables of the preceding layer k − 1 are expressed in terms of the variables v and ω of the following layer k, and in fitting along the coordinate r, the variables of the preceding layer i − 1 are expressed in terms of the variables u and ω of the following layer i. The sequence of calculations is outlined for the example of fitting along z for a fixed layer with respect to the radius $r_i$. Suppose in the k-th layer

$$u_{i-1/2\,k-1}=A_1^{(k)}v_{i\,k-1/2}+B_1^{(k)}\omega_{ik}+D_1^{(k)}; \qquad (13)$$

$$u_{i+1/2\,k-1}=A_2^{(k)}v_{i\,k-1/2}+B_2^{(k)}\omega_{ik}+D_2^{(k)}; \qquad (14)$$

$$v_{i\,k-3/2}=A_3^{(k)}v_{i\,k-1/2}+B_3^{(k)}\omega_{ik}+D_3^{(k)}; \qquad (15)$$

$$\omega_{i\,k-1}=A_4^{(k)}v_{i\,k-1/2}+B_4^{(k)}\omega_{ik}+D_4^{(k)}, \qquad (16)$$

where i = 1, 2, ..., I − 1; k = 1, 2, ..., K − 1.

The values of the "fitting" coefficients $A_\ell$, $B_\ell$, $D_\ell$ ($\ell$ = 1-4) are determined for the following (k + 1)-th layer. To this end, the explicit dependence on $u_{i\pm1/2k-1}$ is first eliminated using the fitting relations in Eqs. (13) and (14). Then it is found that

$$u_{i+1/2\,k} = A_2 v_{i\,k-1/2} + B_2 \omega_{ik} + D_2, \quad (17)$$

$$k = 1, 2, \ldots, K. \quad (18)$$

where

$$A_1 = A_1^{(k)} - \frac{2\Delta z_{k-1/2} r_i}{r_i^2 - r_{i-1}^2}; \quad B_1 = B_1^{(k)};$$

$$D_1 = D_1^{(k)} + \frac{2\Delta z_{k-1/2} r_{i-1}}{r_i^2 - r_{i-1}^2} v_{i-1\,k-1/2};$$

$$A_2 = A_2^{(k)} + \frac{2\Delta z_{k-1/2} r_i}{r_{i+1}^2 - r_i^2}; \quad B_2 = B_2^{(k)};$$

$$D_2 = D_2^{(k)} - \frac{2\Delta z_{k-1/2} r_{i+1}}{r_{i+1}^2 - r_i^2} v_{i+1\,k-1/2}^j.$$

Note that, when z = H(k = K), it should be assumed in these formulas that $\Delta z_k = \Delta z_{k-1/2}/2$ in accordance with the definition of the vorticity for the boundary cell.

New expressions for $u_{i\pm1/2k}$ are substituted into the equation for the vorticity and it is solved for $v_{ik-1/2}$:

$$v_{i\,k-1/2} = a_3 v_{i\,k+1/2} + b_3 \omega_{ik} + d_3$$

$$k = 1, 2, \ldots, K;$$

$$a_3 = \frac{1}{1 + \xi (A_2 - A_1)}; \quad b_3 = \frac{\Delta z_k - \zeta (B_2 - B_1)}{1 + \zeta (A_2 - A_1)}; \quad (19)$$

$$d_3 = \frac{\zeta (D_1 - D_2)}{1 + \zeta (A_2 - A_1)}; \quad \zeta = \frac{\Delta z_k}{\Delta r_i}.$$

Using Eq. (19), the expression for the velocities $u_{i\pm1/2k}$ is transformed to the form

$$u_{i-1/2\,k} = a_1 v_{i\,k+1/2} + b_1 \omega_{ik} + d_1$$

$$k = 1, 2, \ldots, K; \quad (20)$$

$$u_{i+1/2\,k} = a_2 v_{i\,k+1/2} + b_2 \omega_{ik} + d_2, \quad (21)$$

where

$$a_1 = A_1 a_3; \quad b_1 = A_1 b_3 + B_1; \quad d_1 = D_1 + A_1 d_3;$$

$$a_2 = A_2 a_3; \quad b_2 = A_2 b_3 + B_2; \quad d_2 = D_2 + A_2 d_3.$$

Further, in the vorticity-transfer Eq. (12), Eq. (16) for $\omega_{ik-1}$ of the preceding step is first substituted, followed by the expression for $\omega_{i-1k}$ and $\omega_{i+1k}$

$$\omega_{i-1\,k} = \frac{u_{i-1/2\,k} - u_{i-3/2\,k}}{\Delta r_{i-1}} - \frac{v_{i-1\,k+1/2} - v_{i-1\,k-1/2}}{\Delta z_k};$$

$$\omega_{i+1\,k} = \frac{u_{i+3/2\,k} - u_{i+1/2\,k}}{\Delta r_{i+1}} - \frac{v_{i+1\,k+1/2} - v_{i+1\,k-1/2}}{\Delta z_k},$$

deriving from Eq. (10) for the vorticity. Finally, the velocities $v_{ik-1/2}$, $u_{i\pm1/2k}$ are eliminated from the resulting equation using Eqs. (19)-(21) and it is solved for $\omega_{ik}$ to give finally the fitting relation for the vorticity in the (k + 1)-th layer:

$$\omega_{ik} = A_4^{(k+1)} v_{i\,k+1/2} + B_4^{(k+1)} \omega_{i\,k+1} + D_4^{(k+1)}, \quad (22)$$

$$k = 1, 2, \ldots, K-1.$$

Expressions for the coefficients in Eq. (22) may be found in [5], where the give method is outlined in detail. The other fitting factors in the (k + 1)-th layer are determined by substituting Eq. (22) for $\omega_{ik}$ into the corresponding Eqs. (19)-(21). Then, for example, the coefficients of the fitting relation determining $u_{i-1/2k}$ are found to be

$$A_1^{(k+1)} = a_1 + b_1 A_4^{(k+1)}; \quad B_1^{(k+1)} = b_1 B_4^{(k+1)};$$

$$D_1^{(k+1)} = d_1 + b_1 D_4^{(k+1)}.$$

Thus, if the fitting factors $A_l^{(k)}, B_l^{(k)}, D_l^{(k)}$ in the k-th layer are known, successive use of the above formulas permits the calculation of $A_l^{(k+1)}, B_l^{(k+1)}, D_l^{(k+1)}$ in the (k + 1)-th layer, then in the (k + 2)-th layer, etc. The initial values of the fitting factors when z = 0 are calculated from the corresponding boundary conditions

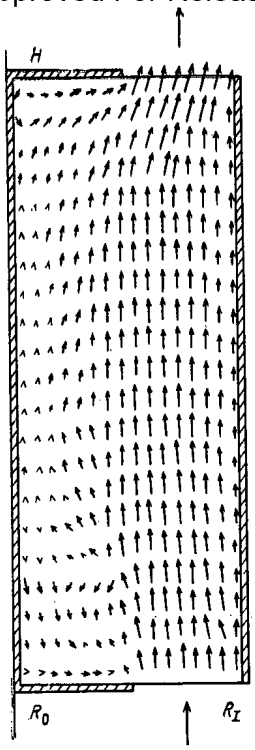


Fig. 2

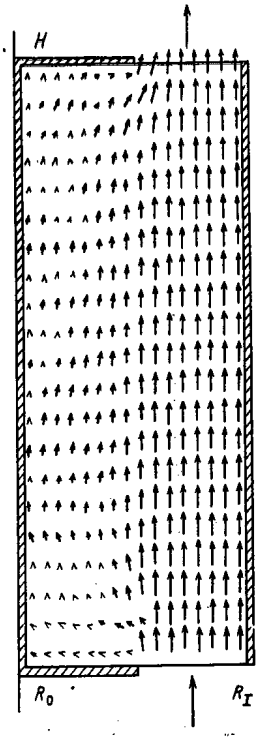


Fig. 3

Fig. 2. Velocity field in the unenclosed cylinder with an obstacle at the inlet and outlet ($\Lambda_r = 0$, $\Lambda_z = 0$).

Fig. 3. Velocity field in the active zone with obstacles at the cylinder inlet and outlet ($\Lambda_r \gg \Lambda_z \gg 0$).

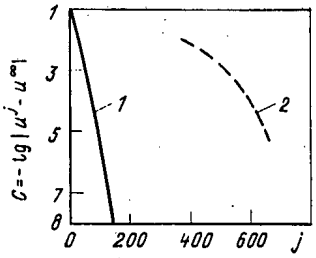


Fig. 4. Establishing the solution: 1) (u, v, ω) method; 2) (u, v, p) method.

$$A_1^{(1)} = 0; \qquad B_1^{(1)} = 0; \; D_1^{(1)} = u_{i-1/2\,0};$$

$$A_2^{(1)} = 0; \qquad B_2^{(1)} = 0; \; D_2^{(1)} = u_{i+1/2\,0};$$

$$A_3^{(1)} = 0; \qquad B_3^{(1)} = 0; \; D_3^{(1)} = v_{i0};$$

$$A_4^{(1)} = -\frac{2}{\Delta z_{1/2}}; \; B_4^{(1)} = 0; \; D_4^{(1)} = \frac{u_{i+1/2\,0} u_{i-1/2\,0}}{\Delta r_i} + \frac{2v_{i0}}{\Delta z_{1/2}}.$$

At the upper boundary with z = H, the velocity is known from the boundary conditions. The boundary value of the vorticity $\omega_{ik}$ may be found from Eq. (20), taking $u_{i-1/2k} = u_{i-1/2K}$ and $v_{ik+1/2} = v_{iK}$ according to the formula

$$\omega_{iK} = (u_{i-1/2K} - a_i v_{iK} - d_i)/b_i.$$

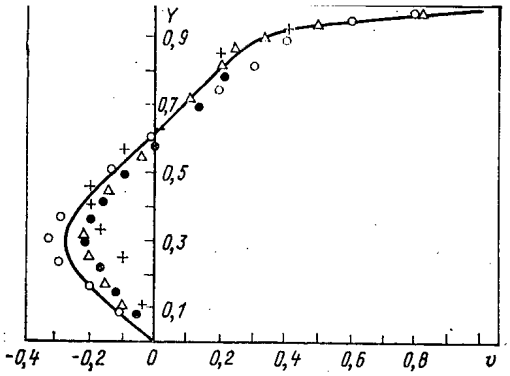


Fig. 5. Horizontal-velocity profile in the central vertical cross section of a cavity with Re = 400: the continuous curve corresponds to the data of [8], uniform grid 57 × 57, nonuniform grid 29 × 29 and the data of [9], uniform grid 41 × 41; the crosses to [10], finite-element method (FEM), grid 15 × 15; the circles to [11], FEM, grid 51 × 51; the filled circles to [12], grid 40 × 40; triangles to the (u, v, ω) method, grid 31 × 31.

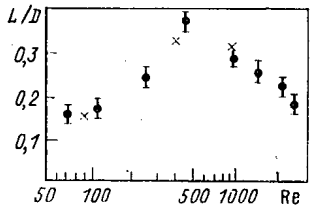


Fig. 6. Dependence of the vortex height at an upstream point of the cavity on the Reynolds number: filled circles correspond to the experimental data of [13] and crosses to the results of calculation by the (u, v, ω) method.

After inverse fitting according to Eqs. (13)-(16), the vorticity and radial velocity component at the i-th radius are determined, as well as the axial velocity component at the radii i + 1/2 and i − 1/2. This means that the velocity component u is actually calculated twice at each internal point: first as $u_{i+1/2k}$ at the i-th radius and secondly as $u_{i-1/2k}$ at the (i + 1)-th radius. All the velocity values appearing in Eq. (8) belong to the next iteration, i.e., Eq. (8) is a purely implicit relation. Hence, after repeated calculation of the velocity $u_{i-1/2k}$, the continuity equation for the corresponding cell is solved accurately. The solution of Eqs. (10) and (12) for the vorticity is iterative.

The formulas given for the fitting factors are used in the layers i = 1, 2, 3, ..., I − 1. For the layer i = 1 with which the calculation begins, it must be taken into account that $\omega_{i-1}$ is calculated for the corresponding halfcell, taking account of boundary conditions according to formulas of the type in Eq. (11) but for the boundary $r = R_0$. For the last fitting layer i = I − 1, the vorticity $\omega_{i+1k}$ is determined taking account of the boundary conditions for $r = R_I$.

The fitting in the radial direction is organized analogously. But in this case the variables $v_{i-1k-1/2}$, $v_{i-1k+1/2}$, $\omega_{i-1k}$, $u_{i-3/2k}$ of the preceding (i − 1)-th layer are expressed in terms of the parameters $u_{i-1/2k}$ and $\omega_{ik}$ of the next layer i. Crossed fitting is continued until an iterative process with specified accuracy is established.

Numerical experiments show that the stability of the given method is practically absolute. In particular, the integration step is varied over the range $10^{-3} \leq \Delta t \leq 1$. The convergence rate of the iterative process decreases with increase in Reynolds number. However, the formally stable solutions are obtained with an arbitrary Reynolds number, for example, for an ideal liquid. At sufficiently large frictional coefficients, the rate of convergence is approximately an order of magnitude larger than for the Navier–Stokes problem. This is a consequence of the simpler structure of flow in the presence of volume frictional forces. Whereas when $\Lambda_r = 0$ and $\Lambda_z = 0$ there are vortex zones behind the obstacle at the inlet and in front of the obstacle at the cylinder outlet (Fig. 2), when $\Lambda_r$ and $\Lambda_z$ are sufficiently large (Fig. 3), the flow pattern becomes close to potential flow.

The advantage of this method in solving problems on friction in comparison with the implicit methods formulated in the variables velocity–pressure [6] is obvious from Fig. 4, where the dependence of the accuracy $C = -\log(u^j - u^\infty)$ on the number of iterations in both methods in solving the same problem for liquid flow in a cylindrical region with obstacles at the inlet and outlet is shown. It follows from Fig. 4 that in the (u, v, ω) method the relaxation of the perturbation introduced by the initial data occurs considerably more rapidly. This is especially significant when high accuracy of the solution is not required. In particular, almost an order of magnitude fewer iterations are required to obtain a solution with an error of 0.1% in the given sample for the (u, v, ω) method.

The difference in convergence rate for the two methods becomes less considerable for the Navier–Stokes problem. Also in this case, however, the (u, v, ω) method allows a solution of specified accuracy to be obtained 2-3 times faster. The accuracy of the method is checked in solving a series of test problems for the Navier–Stokes equations ($\Lambda_r = 0$, $\Lambda_z = 0$): flow in a tube with sudden expansion at Re = 0-200, liquid flow in a square cavity with Re = 100-1000, longitudinal flow around a cylinder and a disk with Re = 40-1000. The theoretical data are in good agreement with experimental data and the results of other authors; see [7] for more details. The accuracy of the (u, v, ω) method may be judged from a comparison of the results of solving a typical test problem for liquid flow in a square cavity by the method here proposed with theoretical [8-12] and experimental [13] literature data (Figs. 5 and 6).

Note, in conclusion, that the method here proposed may also be formulated solely in "velocity" variables, without explicit use of the vorticity. It is sufficient to eliminate the vorticity from Eq. (12) using Eq. (10) and to transform the fitting relations to the form where the velocities $u_{i\pm1/2k}$, $v_{ik-1/2}$ being determined may be expressed in terms of $v_{ik+1/2}$ and $v_{ik+3/2}$.

## LITERATURE CITED


1. M. K. Gorchakov, V. M. Koshcheev, A. G. Kolmakov, and Yu. S. Yur'ev, Teplcfiz. Vys. Temp., 14, No. 4, 866 (1976).
2. M. P. Leonchuk, N. S. Smirnova, and Yu. E. Shvetsov, At. Energ., 52, No. 3, 187 (1982).
3. H. Domanus et al., Nucl. Eng. Des., 62, 81 (1980).
4. P. J. Roache, Computational Fluid Dynamics, Hermosa (1976).
5. M. P. Leonchuk, Z. V. Sivak, Yu. E. Shvetsov, Preprint FEI-1434 [in Russian], Obninsk (1983).
6. M. P. Leonchuk and Yu. E. Shvetsov, Preprint FEI-1100 [in Russian], Obninsk (1980).
7. M. P. Leonchuk, Z. V. Sivak, and Yu. E. Shvetsov, Preprint FEI-1433 [in Russian], Obninsk (1983).
8. K. Gkhia, V. Khénki, and Dzh. Khodzh, Raket. Tekh. Kosmon., 17, No. 3, 89-92 (1979).
9. O. R. Burggraf, in: Collection of Reviews and Translations of Foreign Periodical Literature, Mechanics [Russian translation], Mir, Moscow (1966), No. 6(100), pp. 51-90.
10. A. G. Daikovskii, V. I. Polezhaev, and A. I. Fedoseev, in: Numerical Methods of Continuum Mechanics [in Russian], Vol. 11, No. 1, Novosibirsk (1980), p. 37.
11. V. I. Kopchenov, A. I. Kraiko, and M. P. Levin, Zh. Vychisl. Mat. Mat. Fiz., 22, No. 6, 1457-1467 (1982).
12. S. Ozawa, J. Phys. Soc. Jpn., 38, No. 3, 889-895 (1975).
13. F. Pan and A. Acrivos, J. Fluid Mech., 28, No. 4, 643-655 (1967).

# TRENDS IN THE GLOBAL SPREAD OF $^{129}I$ AND FORECASTING THE ACCUMULATION DUE TO RELEASE FROM NUCLEAR FUEL CYCLE FACILITIES

B. I. Styro, T. N. Nedvetskaite,
and V. I. Filistovich

UDC 551.464.6:551.510.7

Research on man-made environmental pollution is a major task in current science. It has recently been found that certain radionuclides accumulating in the environment may affect geophysical processes [1], whose changes may affect man. These nuclides include not only the radioactive noble gases but also $^{129}I$, whose half-life is about $10^7$ years. This nuclide continuously accumulates in the environment from the operations of fuel processing facilities (FPF) throughout the world. Here we consider this accumulation and forecast the possible increase, which provides specifications for systems for restricting the entry of $^{129}I$ into the environment.

One assumes that the geochemical circulation of $^{129}I$ follows the same laws as that for stable $^{127}I$ [2, 3]. No allowance is made for isotopic fractionation because we lack any information on the process.

In researching th $^{127}I$ mass balance, it was assumed that there are no additional sources of it and there are only transitions from one sphere to another, where the fluxes should be equal. With regard to the $^{129}I$ balance, however, there are additional sources and sinks in each pool: the spontaneous fission of $^{238}U$ [4], the formation of $^{129}I$ by the interaction of cosmic radiation with atmospheric xenon [5], and radioactive decay.

We have introduced nine pools in examining the iodine circulation (Fig. 1). The symbols are: $C_i$, the $^{129}I$ concentrations in the steady state in the individual pools, the constants $\mu_{ij}$ for passage from one pool to another, the constants $\mu_i$ for passage from one pool to all the others, the rates of formation $Q_i$ of $^{129}I$ in the individual pools, and the decay constant $\lambda$. Then in accordance with the scheme of Fig. 1, we have the following system of equations for the global equilibrium distribution of $^{129}I$ in the environment:

$$\begin{aligned}
Q_1 &= \mu_1 C_1 - \mu_{21} C_2 - \mu_{31} C_3;\\
Q_2 &= \mu_2 C_2 - \mu_{12} C_1 - \mu_{52} C_5;\\
Q_3 &= \mu_3 C_3 - \mu_{13} C_1 - \mu_{43} C_4 - \mu_{63} C_6 - \\
&\quad - \mu_{83} C_8 - \mu_{93} C_9;\\
Q_4 &= \mu_4 C_4 - \mu_{24} C_2 - \mu_{54} C_5;\\
Q_5 &= \mu_5 C_5 - \mu_{45} C_4;\\
Q_6 &= \mu_6 C_6 - \mu_{36} C_3 - \mu_{76} C_7;\\
Q_7 &= \mu_7 C_7 - \mu_{67} C_6;\\
Q_8 &= \mu_8 C_8 - \mu_{48} C_4;\\
Q_9 &= \mu_9 C_9 - \mu_{49} C_4.
\end{aligned} \tag{1}$$

The overall transfer coefficients for the individual pools take the values

$$\begin{aligned}
&\mu_1 = \lambda + \mu_{12} + \mu_{13},\ \mu_2 = \lambda + \mu_{21} + \mu_{24},\\
&\mu_3 = \lambda + \mu_{31} + \mu_{36},\ \mu_4 = \lambda + \mu_{43} + \mu_{45} + \mu_{48} + \mu_{49},\\
&\mu_5 = \lambda + \mu_{52} + \mu_{54},\ \mu_6 = \lambda + \mu_{63} + \mu_{67},\\
&\mu_7 = \lambda + \mu_{76},\ \mu_8 = \lambda + \mu_{83},\ \mu_9 = \lambda + \mu_{93}.
\end{aligned} \tag{2}$$

Translated from Atomnaya Énergiya, Vol. 58, No. 3, pp. 171-174, March, 1985. Original article submitted May 10, 1984.

0038-531X/85/5803-0199$09.50  

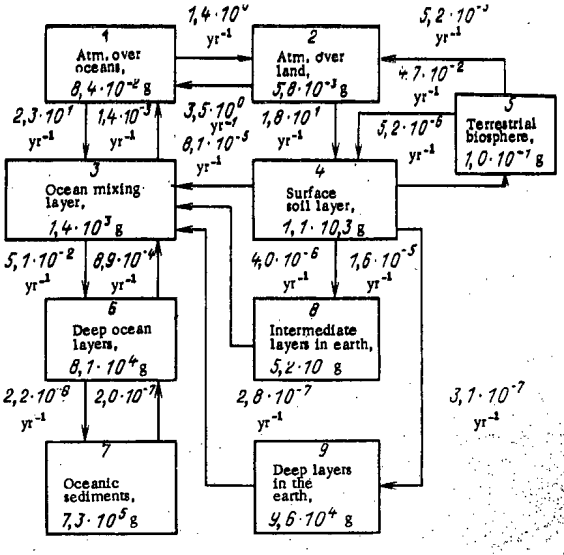


Fig. 1. Scheme for the global biogeochemical circulation of $^{129}I$ (1-9 are the pools).

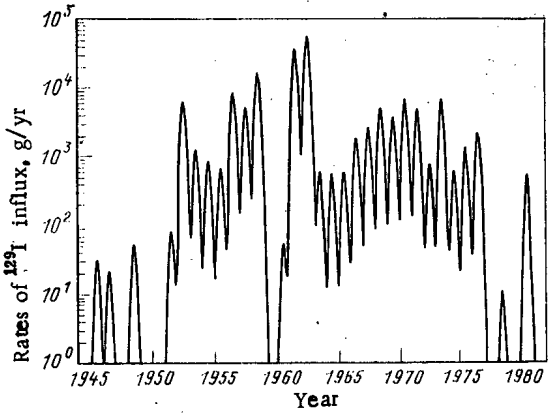


Fig. 2. Rates of $^{129}I$ influx due to nuclear tests.

The values of the $\mu_{ij}$ were taken as for stable iodine [2, 3]. System (1) was solved numerically, and Fig. 1 gives the results.

Here it should be borne in mind that the earth's crust contains 240 TBq of $^{129}I$ [6], but only about 6 TBq is involved in the circulation. The man-made $^{129}I$ perturbs the stationary distribution and began to enter the environment in 1945. In [7], the irregular fluctuations in the entry of $^{129}I$ due to nuclear tests were smoothed by a method as used here. The influx $y_j$ in year i was converted to an influx rate q(t) in g/yr at a time t by means of a sum of Gaussian functions: $q(t) = (1/\sqrt{2\pi}\sigma) \sum_i y_i \exp\{-(t - t_i - 1/2)^2/(2\sigma^2)\}$ with its maximum in the middle of year $t_i$. The parameter $\sigma$ was taken as 1/6 year, as in [7]. Figure 2 shows the graph for this function. In the case of our value of $\sigma$, the sum of Gaussian functions in q(t) can be replaced by a Gaussian function for each year $q_i(t)$, with the assumption that the discharge in year i does not make a substantial contribution to subsequent years.

It was further assumed that the $^{129}I$ formed by nuclear tests enters pool 10 in the earth's stratosphere, which is not shown in Fig. 1, with a half-deposition time from this pool of about one year. Then the $^{129}I$ enters the troposphere, with a half-deposition time of 15 days.

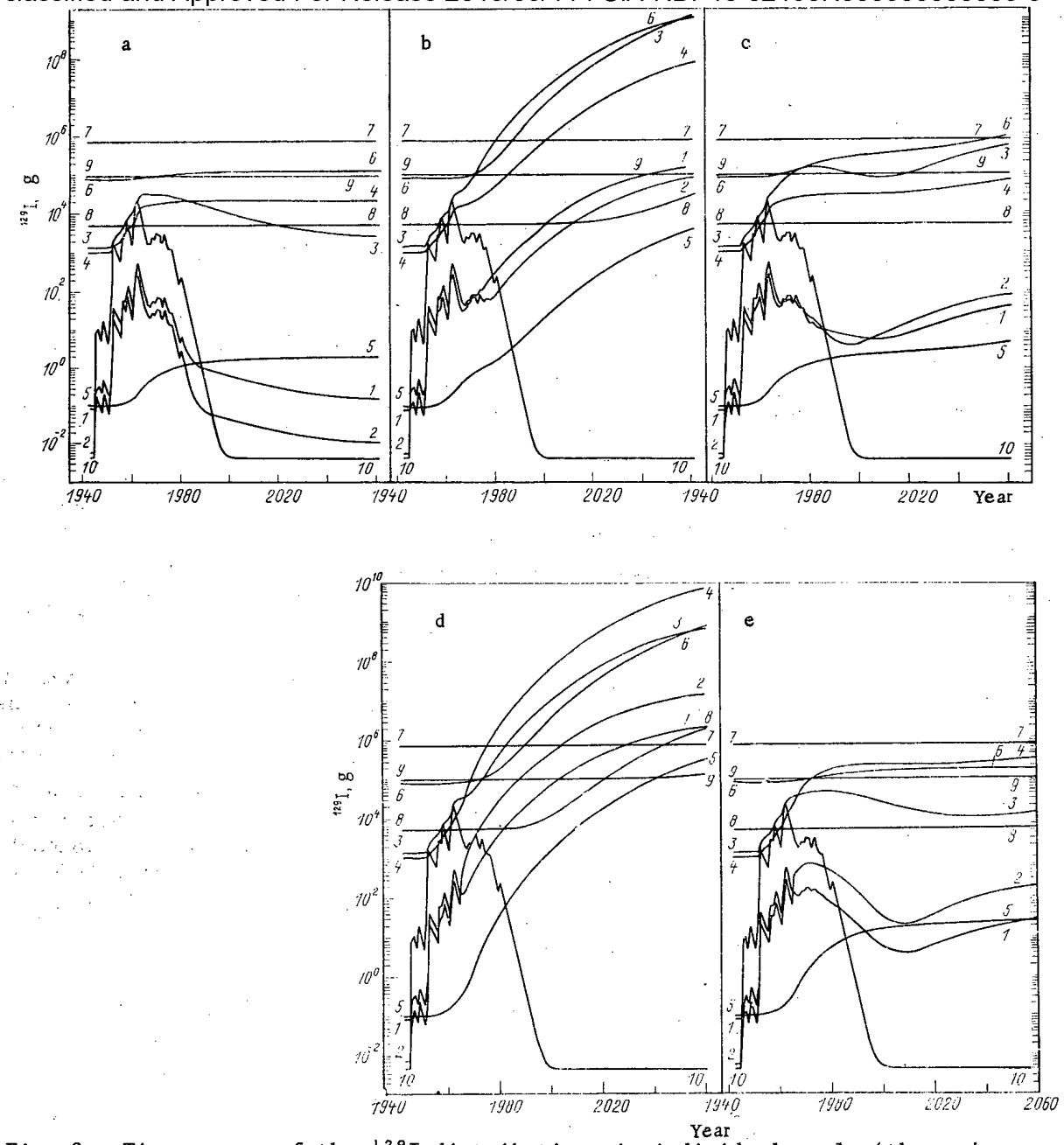


Fig. 3. Time course of the $^{129}$I distributions in individual pools (the numbers on the lines are those of the pools in Fig. 1): a) due to natural processes and nuclear tests; b, d) due to natural processes, nuclear explosions, and the operation of FPF provided that current level is maintained for the purification coefficient and the entry of $^{129}$I into the environment in accordance with the first and second models correspondingly; c, e) the same as in the previous case but on increasing the purification coefficient in accordance with Fig. 4 for the first and second models correspondingly.

Then the $^{129}$I distribution in the environment can be determined by solving a system of differential equations:

$$\frac{dC_1}{dt} = -\mu_1 C_1 + \mu_{21} C_2 + \mu_{31} C_3 + 0.708\mu_{10.1} C_{10} + Q_1;$$

$$\frac{dC_2}{dt} = \mu_{12} C_1 - \mu_2 C_2 + \mu_{52} C_5 + 0.292\mu_{10.2} C_{10} + Q_2;$$

$$\frac{dC_3}{dt} = \mu_{13} C_1 - \mu_3 C_3 + \mu_{43} C_4 + \mu_{63} C_6 + \mu_{83} C_8 + \mu_{93} C_9 + Q_3;$$

$$\frac{dC_4}{dt} = \mu_{24}C_2 - \mu_4 C_4 + \mu_{54}C_5 + Q_4;$$
$$\frac{dC_5}{dt} = \mu_{45}C_4 - \mu_5 C_5 + Q_5; \qquad (3)$$
$$\frac{dC_6}{dt} = \mu_{36}C_3 - \mu_6 C_6 + \mu_{76}C_7 + Q_6;$$
$$\frac{dC_7}{dt} = \mu_{67}C_6 - \mu_7 C_7 + Q_7;$$
$$\frac{dC_8}{dt} = \mu_{48}C_4 - \mu_8 C_8 + Q_8; \qquad \frac{dC_9}{dt} = \mu_{49}C_4 - \mu_9 C_9 + Q_9;$$
$$\frac{dC_{10}}{dt} = -(\lambda + \mu_{10.1})C_{10} + q(t) + Q_{10}.$$

The initial $^{129}I$ content in each pool was taken as the amount obtained by solving (1). The solution to (3) was obtained by the fourth-order Runge–Kutta method with a BÉSM-6. In the case of the nuclear tests, the time course of the $^{129}I$ distribution in each of the pools was as shown in Fig. 3a. It is evident that the $^{129}I$ quite rapidly reaches the earth's surface and enters the ocean mixing layer, and then enters the biosphere (pool 5). It is also evident that the $^{129}I$ contents in the atmosphere and ocean mixing layer decrease rapidly, whereas the soil and biosphere retain the accumulated $^{129}I$ much longer, which is due to the smaller values of the transition constants. There is a certain tendency for the $^{129}I$ contents to increase in the deep ocean layers, while the levels in the oceanic sediments and in the middle and deep layers of the earth vary only very slowly. Also, the amounts of $^{129}I$ in the biosphere and soil exceed the natural stationary $^{129}I$ levels by more than an order of magnitude.

To calculate the global $^{129}I$ distribution due to FPF, we solved (3) with allowance for the rate of entry of $^{129}I$ from FPF. The calculations were performed for two extreme cases: the first model for discharges entering the ocean mixing layer 25 times the discharges entering the atmosphere [8], while the second model has the corresponding ratio of 90 [9].

The incorporation of $^{129}I$ into the circulation is shown in parts b and d of Fig. 3 on the assumption that the purification coefficient in future remains at the current level. These calculations show that on entry to the atmosphere (second model), the $^{129}I$ concentration in pools 4 and 5 during the next decade will be larger by an order of magnitude or more than for passage to the ocean mixing layer (first model). This is because $^{129}I$ spends a long time in the deep-ocean layers. If the FPF work under these conditions, the $^{129}I$ concentrations in the atmosphere, ocean mixing layer, soil, and deep-ocean layers (pools 1-6) increase exponentially. The $^{129}I$ concentration in the biosphere in the year 2000 will exceed the natural level by four or five orders of magnitude for the first and second models correspondingly.

This raises the questions of how far the purification coefficient should be increased at FPF to keep the changes in $^{129}I$ concentration in the environment within an order of magnitude. Figure 4 indicates these recommendations. The data of [2] have been used here. In the first case, the purification coefficient should attain $0.8\text{-}1\cdot10^4$ by the year 2000, while in the second it should be larger by an order of magnitude. Figure 4 also indicates the amounts of $^{129}I$ entering the environment if the purification alters in accordance with the first and second models. Figure 3c (first model) and Fig. 3e (second model) show the $^{129}I$ distributions occurring with time-varying purification coefficient as obtained by solv-

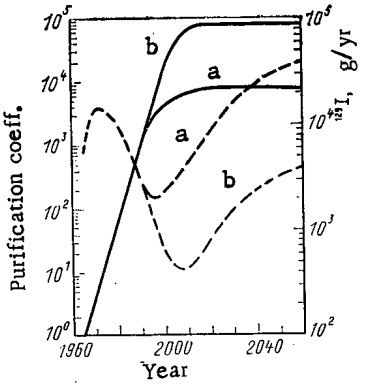


Fig. 4. Recommended increase in the purification coefficient (solid line) and corresponding course of the rate of entry of $^{129}I$ into the environment (dashed line) for the first model (a) and the second one (b).

ing (3). There is a minimum due to the reduced entry of $^{129}I$ from FPF in 1990 in connection with the supposed improvement in the purification system.

These calculations show that $^{129}I$ entering the environment is dispersed in accordance with the laws of iodine circulation. Therefore, to avoid accumulation in any medium or near FPF it is necessary that this rate of entry should be less than or equal to the natural dissipation rate.

In the current level of purification, the $^{129}I$ entering the environment by the year 2000 will virtually all be present in the mixing layer and deep layers of the ocean together with the soil and biosphere. As indicated previously, the levels in the earth's biosphere will increase by 4-5 orders of magnitude. For this reason, it is necessary to improve FPF purification plants in order that by the year 2000 the purification coefficient should attain $1 \cdot 10^4$ or $1 \cdot 10^5$ when most of the $^{129}I$ enters the ocean mixing layer or the atmosphere correspondingly.

In relation to the problem of storing $^{129}I$, it should be borne in mind that it is a migrating global nuclide, and the disposal of it in the oceans, as suggested in [10], may cause considerable accumulation in other pools (in the ocean mixing layer, atmosphere, and soil) and entry into the earth's biosphere.

## LITERATURE CITED


1. B. I. Styro, D. V. Butkus, and K. K. Zemkayus, in: Atmospheric Physics, Vol. 7, Problems in Researching Atmospheric Pollution [in Russian], Mokslas, Vilnius (1981), p. 164.
2. D. Kocher and J. Till, Trans. Am. Nucl. Soc., 33, 1957 (1979).
3. D. Kocher, in: Environmental Migration of Long-Lived Radionuclides, IAEA, Vienna (1982), p. 669.
4. É. V. Sobotovich, E. N. Bartnitskii, O. V. Tsyn', and L. V. Kononenko, Handbook on Isotope Geochemistry [in Russian], Énergoizdat, Moscow (1982), p. 241.
5. V. I. Filistovich, T. N. Nedvetskaite, and V. Yu. Luyanas, in: Atmospheric Physics, Vol. 9, Local and Global Impurities in the Atmosphere [in Russian], Mosklas, Vilnius (1984), p. 171.
6. C. Keller, Naturwissenschaft Rundsch., 30, No. 8, 293 (1977).
7. G. Kilough, Health Phys., 38, No. 3, 269 (1980).
8. I. Ya. Vasilenko and Yu. I. Moskalev, "Biosphere contamination with $^{129}I$," At. Energ., 52, No. 3, 155-158 (1982).
9. J. Russel and P. Hahn, Radiol. Health Data Rep., 12, No. 4, 189 (1971).
10. "Radioiodine removal in nuclear facilities. Methods and techniques for normal and emergency situations," in: Techn. Rep. Ser. No. 201, IAEA, Vienna (1980), p. 98.

# BACKGROUND LIMITATIONS IN X-RAY FLUORESCENCE ANALYSIS

V. V. Berdikov, E. A. Zaitsev, and B. S. Iokhin

UDC 543.426

For the x-ray fluorescence analysis of solutions formed in the technological processes of the nuclear fuel cycle, a method of preliminary selection was developed for the content of heavy elements [1, 2] according to the radiation energy of the sample, by means of a cylindrical pyrographite Bragg reflector, located between the sample and an Si(Li) detector. This method allows the background created by scattered perturbing radiation to be reduced. Limits of detection ~0.15 ppm were achieved for uranium and neighboring elements in solution with quasimonochromatic excitation of a transmission x-ray tube with a 25-W power; the loading of the spectrometric channel for this amounted to less than 300 $sec^{-1}$.

This paper reports on the attempts to reduce the limits of detection, due to the use of a powerful tube for excitation. Values were obtained for the limits of detection of $\sim 10^{-8}$. In addition to the background components discussed earlier [1], two further effects were found to be significant in the background generation: bremsstrahlung of photoelectrons in the sample and Compton scattering by the bound electrons in it.

Experimental Facility. The layout of the facility is shown in Fig. 1. The scattering chamber is similar to that which was described in detailed earlier [1, 3]. The maximum of the transmission function of the scattering chamber (Fig. 2) is tuned to an energy of 14.0 keV for the optimum recording of the $L_\alpha$-lines of Th, U, Np, and Pu. Excitation is provided by a BKhV-7 x-ray tube (50 kV, 70 mA) with a cylindrical Pd-anode and with water cooling. The average angle $\theta_0$ between the primary and secondary beams in the facility amounts to 90° or 113°. In the latter case (see Fig. 1), the average distance anode–sample is equal to 36 mm. An anode of Pd instead of Ag [1] was chosen because of the lower transmission efficiency of scattered $K_\alpha$ radiation of the anode through the chamber in the second order of reflection. In order to record the fluorescent radiation, an Si(Li) detector with an area of 25 $mm^2$ and with a resolution of 300 eV (at the $UL_\alpha$ 13.6-keV line) used. In order to reduce the detector background in the spectrometric channel, a discriminator is introduced with respect to the front of the pulse rise (DFR) which prohibits recording if the duration of the leading front of the pulse with preamplifier exceeds 150 nsec. It was shown in [4] that the DFR provides a sixfold reduction of the steady detector "tail" of the photopeak, without loss in the counting rate of the peak.

Limits of Detection. The measurements were conducted with aqueous solutions containing uranium to the amount of a few ppm. The limit of detection was determined as the mass fraction corresponding to the area of the peak $p = 233 \cdot b^{1/2}$, where p and b correspond to the time of measurement of 1 h. The background b was measured on a pure sample (cell with water) in an energy window with a width of 2.6 × (PShPV of the $UL_\alpha$ peak).

Just as in [1], the curves of the $UL_\alpha$ count rate, the ratios of peak/background and the limit of detection versus the thickness of the palladium filter (f) and the diameter of the inlet collimator of the chamber (d) were plotted. The main part of the backgrond comprises the residual bremsstrahlung of the tube. Its contribution becomes negligible with f = 350 μm (see Fig. 2). But in this case, because of the large loss in the count rate, the limit of detection increases by a factor of two. Losses in intensity in the general case can be compensated with a more powerful excitation source (a tube with a rotating anode with a power of $\sim 10^5$ W or synchrotron radiation).

Four Components of the Background above the Analytical Peak. The data given here about the background were obtained with the following conditions: tube operating regime 40 kV, 50 mA; f = 350 μm, d = 6 mm, $\theta_0$ = 90° (unless otherwise stated). The total background below the $UL_\alpha$ peak amounts to B = 1.8 $sec^{-1}$. The contribution of the residual bremsstrahlung of the tube ($B_t$) in this case is estimated from the value of $B_t$ with filtration f = 200 μm by multi-

Translated from Atomnaya Énergiya, Vol. 58, No. 3, pp. 174-178, March, 1985. Original article submitted May 28, 1984.

 0038-531X/85/5803-0204$09.50 

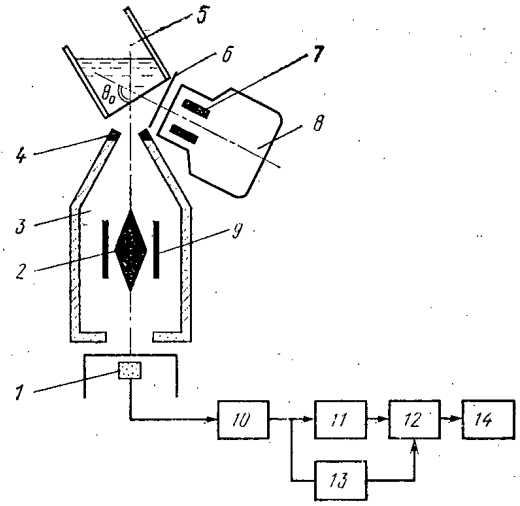


Fig. 1. Diagram of the experimental facility: 1) Si(Li) detector; 2) screen (W); 3) scattering chamber; 4) collimator (W); 5) cell; 6) Pd-filter; 7) cylindrical Pd-anode; 8) x-ray tube; 9) cylindrical pyrographite Bragg reflector; 10) preamplifier; 12) analog–digital converter (ADC); 14) minicomputer.

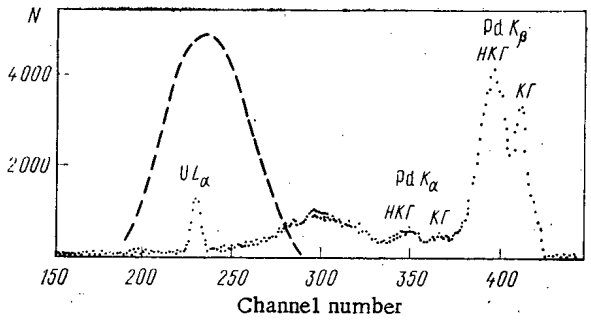


Fig. 2. Spectrum obtained during measurement of a uranium solution ($C_U$ = 6.6 ppm) in the case of intense filtration of the exciting beam (f = 350 μm); the time of collection 600 sec. The dashed line is the transmission function of the scattering chamber (only the first order of reflection is shown).

plying by the factor $\exp(-\mu\rho\Delta x)$, which gives $B_t = 0.01$ sec$^{-1}$. Another component of the background ($B_x$), related with the residual x-factor of the detector, is determined by the part of the spectrum with almost uniform background (in the 10-keV range): $B_x = 0.3$ sec$^{-1}$. Thus, we obtain $B_x + B_t \ll B$, i.e., the remaining part of the background $B_y = 1.5$ sec$^{-1}$ must be explained by some other physical mechanism. We note that special prolonged measurements were made on a pure sample in order to verify the absence, in the region of the background being considered, of the K- or L-lines of any other elements (their intensity is much less than $B_y$). In these control measurements, in order to exclude the possible contribution of the Kr Kβ line from the krypton in the air around the sample and in the scattering chamber, a helium atmosphere was used.

It is supposed that the mechanisms explaining the main part of the background are the bremsstrahlung of the photoelectrons knocked out in solution of the sample by quanta of the exciting Pd K-radiation and also Compton scattering of the exciting Pd K-radiation by bound electrons of light elements in the solution.

We shall estimate the component of the background $B_p$, due to the bremsstrahlung of the photoelectrons. The following expression [5] is derived for the probability of generation of a quantum with energy in the range ($E_x$, $E_x + dE_x$) by an electron with energy $E_0$ moving in a medium with atomic number Z, from Heitler and Bethe–Bloch's formulas:

$$dP = 2.5 \cdot 10^{-6} Z \frac{dE_x}{E_x} (E_0 - E_x), \tag{1}$$

where the energy is expressed in keV. Calculations of the absolute value of $B_p$ require a knowledge of the geometrical factors and corrections for self-absorption. It is more convenient to calculate the ratio $B_p/J_U$, where $J_U$ is the $UL_\alpha$ count rate of the fluorescent radiation from the uranium present in solution. The ratio of the total background B to $J_U$ can be determined easily and experimentally.

For an aqueous solution with a mass uranium fraction $C_U$, we have

$$\frac{B_p}{J_U} = \frac{2.5 \cdot 10^{-6} \Delta E_x (E_0 - E_x) \tau_Z C_Z}{E_x \tau_{UL_{III}} \omega_{UL_{III}} f_\alpha C_U}, \tag{2}$$

where Z, the mass coefficient of photoelectric absorption $\tau_Z$ and the mass fraction $C_Z$ are taken for oxygen; $\tau_{UL_{III}}$ is the mass coefficient of photoelectric absorption for the $UL_{III}$ subshell; $\omega_{UL_{III}}$ is the fluorescence yield; $f_\alpha$ is the fraction of $L_{\alpha 1,2}$ lines among the L-lines, corresponding to transformations in the $UL_{III}$ subshell.

Formula (2) gives $B_p/J_U = 0.33$ (for $C_U = 1$ ppm) if for $E_0$ we substitute the energy of $PdK_\alpha$ and $PdK_\beta$ in the proportion 0.55/0.45, which is achieved after filtration with f = 350 μm; $J_U = 1.5$ sec$^{-1}$ (for $C_U = 1$ ppm), i.e., we obtain $B_p < B_y$. Two corrections should be considered for expression (2). The first is related with inelastic scattering of the secondary emission in the sample, which is significant for the fluorescent radiation but insignificant for the bremsstrahlung (because of their different spectral distribution). It is easy to show that the correction for this effect can be introduced by means of a coefficient, estimated as $k = 1 + \sigma R$, where σ is the linear scattering coefficient; R is the effective radius of the working volume of the sample. Assuming R = 0.5 cm, we obtain k = 1.15.

The second correction is related with the angular distribution of the photoelectron bremsstrahlung. This distribution relative to the primary beam can be obtained as the contraction of the angular distribution of the photoelectrons and the angular distribution of the flight of bremsstrahlung quanta. Both these functions have the form $\sin^2 \varphi$ with a maximum of the first in the direction normal to the primary beam (for low energies), and the maximum of the second at an angle of approximately 50° to the photoelectron pulse with an energy of about 30 keV [6]. Assuming that for an energy of 21 keV this angle is equal to ∿60°, after contraction and normalizing, we obtain

$$f(\theta) \approx \frac{6}{11} \left( \frac{3}{2} + \cos^2 \theta \right), \tag{3}$$

where θ is the angle between the primary and secondary beams of x rays. In this formulation, the angle θ is not strictly fixed, because the anode of the tube and the Bragg reflector have identical shape. Taking into account that the function $f(\theta)$ for $\theta \approx \pi/2$ is weak, we can take 0.85 as the average value of $f(\theta)$. After inserting both corrections, the value of $B_p/J_U$ becomes equal to 0.32.

Let us pass on to consideration of the Compton scattering of PdK radiation by the K-electrons of oxygen atoms in the solution. Scattering by the L-electrons of oxygen can be neglected if we are concerned with the energy losses by scattering of the order of 7 keV, in view of their small binding energy. In order to calculate the cross sections of processes of this type, the momentum approximation [7, 8] can be used:

$$\frac{d^2\sigma}{d\Omega \, d\omega'} = \left( \frac{d\sigma}{d\Omega} \right)_T \frac{\omega'}{\omega} \frac{m}{k} J(q). \tag{4}$$

Here $\left( \frac{d\sigma}{d\Omega} \right)_T = \frac{1}{2} \left( \frac{e^2}{mc^2} \right)^2 (1 + \cos^2 \theta)$ is the Thomson cross section; $k = |\mathbf{k}_1 - \mathbf{k}_2|$ is the absolute value of the change of the wave vector of the photon; ω and ω' are the initial and final energy of the photon; J(q) is the Compton profile for the K-shell:

$$J(q) = \frac{16}{3\pi} \frac{1}{q_K} \left( 1 + \left( \frac{q}{q_K} \right)^2 \right)^{-3}, \tag{5}$$

TABLE 1. Experimental and Calculated Background Values for an Aqueous Solution

| Bkgd. component | Calc. value | Meas. value |
|---|---|---|
| Residual bremsstrahlung ($B_t/J_U$) | 0,007 | Not determ. for f = 350 μm |
| Detector bkgd. (residual x-factor) ($B_t/J_U$) | Same exptl. value is used | 0,2 |
| Bremsstrahlung of photoelectrons in sample ($B_t/J_U$) | 0,32 | $B_y/J_U = 1,0-1,4$ |
| Compton scattering by bound electrons ($B_c/J_U$) | 0,55 ($\theta_{eff}=105°$)<br>0,8 ($\theta_{eff}=115°$) | |
| Total bkgd. ($B/J_U$) | 1,08—1,33 | 1,2—1,6 |

TABLE 2. Experimental and Calculated Background Values for Solutions with Different Matrices ($C_U$ = 1 ppm)

| Solution matrix | $\theta_0$ | Calc. values | | | Meas. value |
|---|---|---|---|---|---|
| | | $B_p/J_U$ | $B_c/J_U$ | $B_{\Sigma}/J_U$ | $B_y/J_U$ |
| $H_2O$; 1,13 % Fe | 90° | 0,71 | 0,72 | 1,43 | 1,75 |
| $H_2O$; 12,6 % Cs | 113° | 3,7 | 4,3 | 8,0 | 5,8 |
| $H_2O$; 9,0 % Co | 113° | 2,3 | 3,2 | 5,5 | 3,2 |

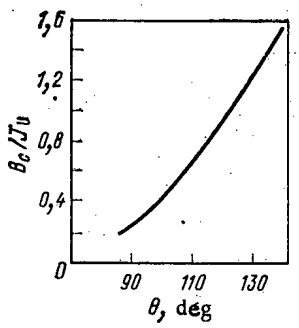


Fig. 3. Calculated angular dependence for the ratio $B_c/J_U$ ($C_U$ = 1 ppm).

where

$$q = \frac{m}{\hbar k}(\omega_0' - \omega); \tag{6}$$

$$\omega_0' = \omega\left(1 - \frac{2\omega}{mc^2}\sin^2\frac{\theta}{2}\right), \tag{7}$$

$$q_K = Zmc/137.$$

From the expressions derived for the effective mass coefficient of scattering of this type, we obtain

$$\sigma_c(\theta) = C_Z \frac{N_0}{A_Z}\left(\frac{e^2}{mc^2}\right)^2 \frac{\omega'}{\omega}(1+\cos^2\theta)\frac{m}{k}\frac{16}{3\pi q_K}\left(1+\left(\frac{q}{q_K}\right)^2\right)^{-3}, \quad (8)$$

where the mass number $A_Z$ and the mass fraction $C_Z$ are taken for oxygen; $N_0 = 6.02\cdot10^{23}$. The strong functions $k(\theta)$ and, as a consequence, $q(\theta)$ lead to a strong angular dependence for $\sigma_c$ for $q/q_K \geqslant 1$. Operating just as the same as for the derivation of formula (2), we can write for the component $B_c$ corrresponding to the Compton scattering

$$\frac{B_c}{J_U} = \frac{4\pi\sigma_c(\theta)\,\Delta E_x}{\tau_{UL_{III}}\omega_{UL_{III}} f_\alpha C_U}. \quad (9)$$

Because of the strong angular dependence (Fig. 3) in this case, we cannot simply substitute $\theta = \pi/2$ in Eq. (9) for comparison with the experimental data. In the facility (taking account of conversion processes of radiation in the Pd-filter between the tube and the sample), a range of angles $\theta$ = 57-123° is achieved. It is obvious that for this, the effective value of $\theta_{eff} > 90°$. Moreover, $\theta_{eff}$ can vary with time. This effect is due to the nonuniform and, probably, unstable distribution of the electron beam over the cylindrical surface of the tube anode.

The calculated and measured background ratios are given in Table 1 for an aqueous solution of uranium ($C_U$ = 1 ppm). Ratios of $B/J_U$ from 1.2 to 1.6 were observed for the total background (the relative statistical errors did not exceed 8%). These variations can be explained by the above-mentioned effect. The calculated $B_c/J_U$ ratios are given for two values of $\theta_{eff}$: $\theta_{eff}$ = 105°, corresponding to a uniform distribution of the electron beam, and $\theta_{eff}$ = 115° illustrates the increase of $B_c$ for a small increase of $\theta_{eff}$. Taking account of the indeterminacy of certain parameters and constants used in the calculation ($\omega_{UL_{III}}$, $\theta_{eff}$, etc.), it can be concluded that the agreement between the calculated and experimental data in Table 1 is satisfactory. In order to verify this, additional experiments were carried out. Firstly, the increase of $B_y/J_U$ was measured for rotation of the tube axis, shown in Fig. 1 ($\theta_0$ = 113°). Ratios of $B_y/J_U$ from 1.6 to 2.3 were observed, i.e., the average increment amounted to 0.75 (expected was 0.7).

A second series of measurements was carried out with solutions differing strongly from water with respect to macrocomposition. It can be seen from formulas (2) and (8) that the background components $B_p$ and $B_c$ depend on the effective Z number of the sample. The contributions to $B_c$ are additive for the different elements in the sample, but when calculating $B_p$ averaging must be carried out separately:

$$B_p \sim \langle\tau_Z\rangle\langle Z\rangle, \quad (10)$$

as the processes of photoelectric absorption and bremsstrahlung generation are independent. The results of the measurements, and also the calculated values for solutions containing large amounts of Cs, Fe, and Co (and several ppm of U), are given in Table 2. The tendency to increase of $B_y/J_U$ with increase of Z is confirmed. The discrepancies between calculation and experiment probably can be explained by the rough assumptions in the method of momentum approximation used for the calculation of $B_c$.

Thus, the four mechanisms of background generation considered apparently are sufficient for explaining the background in the noncrystal version with quasimonochromatic excitation. The components $B_p$ and $B_c$ are determined by processes in the sample itself, and therefore impose a limitation on the peak/background ratio which can be achieved for given mtrix of a "thick" sample. The component $B_c$, in principle, can be reduced either by means of polarized beams for excitation (but this is associated with loss of intensity by three to four orders) or by means of a reduction of the angle of take-off. However, the component $B_c$ depends weakly on $\theta$ and is not related with polarization. Consequently, the limits of detection in reality can be improved only by an increase of the intensity of the exciting beam. Values on the order of $2\cdot10^{-9}$ can be achieved, obviously, for the analysis of heavy elements in a light matrix, if a tube with a power of $\sim10^5$ W is used for excitation, with a rotating anode and with an anode–sample distance at 30-40 mm.

Thus, the method of preliminary selection with respect to the energy of the emission from the sample ensures the highest peak/background ratio in the case of noncrystal x-ray fluorescence analysis of thick samples. These maximally attainable ratios are determined by processes in the sample itself, and can be estimated by the method described above. With the use for excitation of commercially manufactured x-ray tubes with a power of a few kW, the heavy elements in light materials with a content on the order of $10^{-8}$ can be analyzed. It

may be supposed that there will be a similar situation in the case of noncrystal analysis of elements with average and, possibly, low Z number and also in the crystal-diffraction version of x-ray fluorescence analysis.

## LITERATURE CITED


1. V. Berdikov, O. Grigor'ev, and B. Iokhin, Nucl. Instrum. Methods, 155, 313 (1978).
2. V. Berdikov, O. Grigor'ev, and B. Iokhin, J. Radioanal. Chem., 68, 181 (1982).
3. V. Berdikov, O. Grigor'ev, and B. Iokhin, J. Radioanal. Chem., 58, 123 (1980).
4. V. V. Berdikov, E. A. Zaitsev, B. S. Iokhin, Preprint of the V. G. Khlopin Radium Institute, RI-166 [in Russian], Leningrad (1983).
5. F. Goulding and J. Jaklevic, Nucl. Instrum. Methods, 142, 323 (1977).
6. A. Compton and S. Alison, X-Ray Beams, Theory and Experiment [Russian translation], Gostekhizdat, Leningrad–Moscow (1941).
7. P. Eizenberger and P. Platzman, Phys. Rev., A2, 415 (1970).
8. V. A. Bushuev and R. N. Kuz'min, Usp. Fiz. Nauk, 122, 81 (1977).


# METHOD OF INVESTIGATION OF γ-RAY CASCADES FROM THE MULTIPLICITY SPECTRUM AND LOW-ENERGY γ-TRANSITIONS


B. V. Danilin, B. V. Efimov,
G. V. Muradyan, F. N. Belyaev,
and V. P. Bolotskii


UDC 539.17 + 539.122

The study of γ-ray cascades that arise during the resonance capture of neutrons is of great interest for the investigation of the properties of nuclear levels. If the cascade does not pass through an isomeric state, it can be considered as a process that distinguishes a certain generality of properties of the nuclear levels through which it passes. The study of a large number of neutron resonances, therefore, makes it possible to compare their quantum characteristics with different types of γ-ray cascades. For a complete examination of a γ-ray cascade it is necessary to establish its passage through all the intermediate levels. The solution of this problem in the general case involves a large number of technical difficulties. It thus becomes necessary to use methods of investigation that give only partial information.

The principal feature of cascades in an (n, γ) reaction is a considerable change in its nature on passing from the neutron-capturing state to the ground state. The density of the nuclear levels drops and their structure becomes simpler in the process. As the cascade begins there are a large number of ways in which it can proceed while toward the end it is contracted abruptly. This allows the cascade to be divided arbitrarily into two stages, initial and final. In the first approximation, in the initial stage a γ-ray cascade is characterized by the number of γ-ray quanta emitted (their multiplicity) and their average energy. The specific levels through which the cascade passes are less significant. It is more important to know in how many stages the nucleus released the excitation energy and changed its moment and parity. The range of levels of the final stage can be chosen so that when a cascade enters it the further fate of the cascade can already be predicted in the main. Thus, the multiplicity of γ-ray quanta in the initial stage and the level from which the final stage begins can characterize the cascade.

For the experimental execution of the program it was natural to use multisectional 4π-detectors, based on NaI crystals, which are applied in the study of (n, γ) and (n, f) reactions [1]. They can be used directly to study the initial stage of the cascade. In our program such a detector had to be supplemented with one more, making it possible to establish the final stage. From the methodological point of view the final stage can be isolated easily if it contains γ-ray quanta of lower energy than the first stage does. In this case we can use a thin detector that can effectively detect the low-energy γ-ray quanta of the final stage and freely transmit the γ-ray quanta of the initial stage. This treatment is applicable to nuclei that have intense low-energy transitions at the end of the cascade. A

Translated from Atomnaya Énergiya, Vol. 58, No. 3, pp. 178-183, March, 1985. Original article submitted March 16, 1984.

0038-531X/85/5803-0209$09.50  

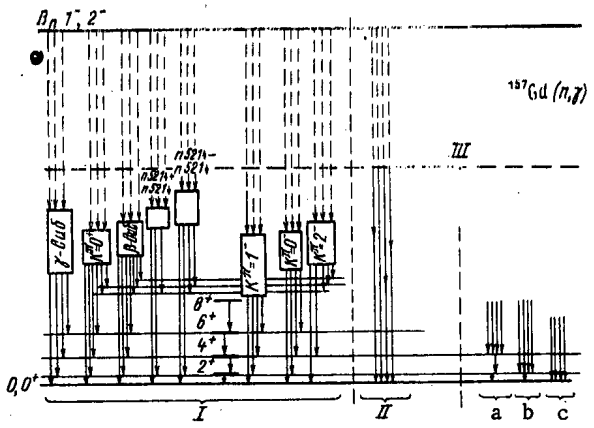


Fig. 1. Classification of γ-ray cascades on the example of $^{158}$Gd compound-nuclei. Cascades that include levels of the rotational band of the ground state (I) pass simultaneously through a series of collective excitations (γ-vibrational, $K^{\pi} - 0^{+}$, etc.). Cascades that do not include the rotational band of the ground state (II) most probably bypass these bands as well. On the right (a, b, c) we show the classification of γ-ray cascades of our experiment. III denotes the boundary of the region of known levels.

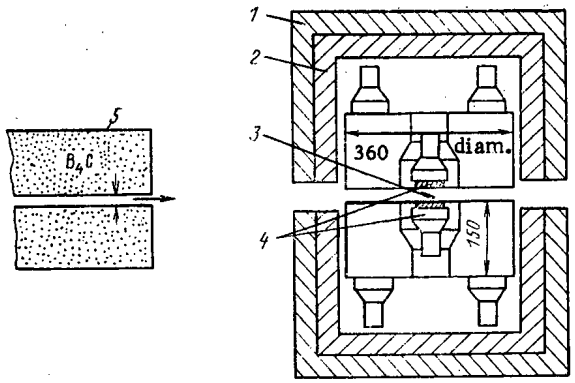


Fig. 2. Detector arrangement: 1) boron polyethylene; 2) lead; 3) specimen; 4) detector of low-energy γ-ray quanta; 5) slit collimator.

typical example of such transitions is that of intense E2 transitions in the fundamental $4^{+} - 2^{+} - 0^{+}$ rotational band for even-even deformed nuclei (Fig. 1). Most γ-transitions from the vibrational and other collective bands that lie in the region $E_x$ = 0.5-2 MeV pass through these levels. Detection of $4^{+} - 2^{+} - 0^{+}$ transitions with an energy of 70-200 keV will denote passage of the cascade through these bands and the absence of these transitions will indicate with a considerable degree of probability that the cascade had bypassed the collective bands. The compound nuclei $^{156}$Gd, $^{158}$Gd, $^{162}$Dy, $^{164}$Dy, $^{168}$Er, $^{172}$Yb, $^{174}$Yb, $^{178}$Hf, $^{180}$Hf, $^{184}$W, and $^{190}$Os are suitable for study by the indicated method and are formed in an (n, γ) reaction.

General Scheme of the Experiment. In the experiment γ-ray cascades in an (n, γ) reaction are studied on the basis of the number of γ-ray transitions and the characteristic of the passage of the cascade through chosen levels in its final stage, using the time-of-flight technique. The Fakel linear electron accelerator serves as a pulsed source of neutrons. The path length is 45 m and the time resolution is 2.2 nsec/m.

The setup consists of the following main elements:

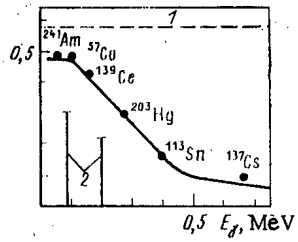


Fig. 3. Efficiency of detection of γ-ray quanta (with discrimination of the total energy) in the detector for low-energy γ-ray quanta, measured with the aid of standard γ-ray sources: 1) geometric efficiency; 2) γ-ray transitions measured in $^{156}$Gd.

a 12-section γ-ray detector based on NaI crystals, dubbed "Romashka";

a spectrometric detector of low-energy γ-ray quanta, with a high detection efficiency for an energy of up to 200 keV;

electronic equipment to receive signals from the detectors and carry out the preliminary processing of the signals prior to transmission to a computer;

an SM-4 computer which sorts and stores the data input from the detector system.

For each detected (n, γ) reaction event the computer records the neutron time of flight T, the multiplicity K of coincidences on signals of γ-ray quanta in the "Romashka" detector, as well as information obtained from the spectrometric detector about the detection of γ-ray quanta in the final stage of the cascade, viz., the amplitude characteristic A. From these data for cascades with a specified type of end we can get the relative intensity (per neutron capture) and the spectrum of multiplicity of the emitted γ-ray quanta. These data form an ensemble over the neutron resonances studied.

Detector Arrangement and Its Characteristics. The detector arrangement in the operating position on a neutron beam is shown in Fig. 2. The design and main properties of the Romashka detector were described in [2]. The twelve sections of the detector are scanned by an FÉU-110 photomultiplier. During traditional use the two blocks are in tight contact with each other and the neutron beam passes along their axis. In our case, we changed the geometry so as to place a spectrometric detector of low-energy γ-ray quanta in the internal cavity. The blocks were moved apart by 2.5 cm and the neutral beam was passed through the slit so formed. This resulted in a loss of efficiency by the detector, viz., its geometric efficiency decreased from 0.96 to 0.87. The probability of detection of γ-ray quanta with an energy of ∿1.2 MeV lay within the limits 0.82-0.85. It was determined by measurement of the complete spectrum of $^{60}$Co quanta, carried out for the total signal from all 12 sections.

The spectrometric detector of low-energy γ-ray quanta consists of two scintillation blocks with NaI(Tl) crystals of diameter 63 mm and height 20 mm and an FÉU-110 photomultiplier. On the specimen side the crystals are covered with a thin layer of MgO and an aluminum foil of thickness 0.1 mm. The specimen is placed between the scintillation blocks. Its design ensures a yield of low-energy γ rays and allows a few grams of the substance to be used. The size of the crystals was chosen so that γ-ray quanta with an energy of less than 200 keV would be detected with a high efficiency while high-energy quanta from the cascade, which should pass freely through the detector and be detected in Romashka, would be detected with a low efficiency. On the basis of measurements with calibrated sources of γ-ray quanta we obtained the dependence of the detector efficiency on $E_\gamma$ for total absorption of the energy of the γ-ray quantum (Fig. 3). The efficiency was 36 and 46%, respectively, for γ-ray quanta corresponding to $4^+ - 2^+$ and $2^+ - 0^+$ transitions in $^{156}$Gd.

The spectrometric characteristics of the detector of low-energy γ-ray quanta are given in Fig. 4 (the spectra shown were measured with the aid of several standard γ-ray sources). The resolution of the detector varies from 30 to 15% in the range from 60 to 280 keV. Such a resolution is sufficient, e.g., for the study of $4^+ - 2^+$ and $2^+ - 0^+$ transitions in the fundamental rotational bands of $^{156,158}$Gd.

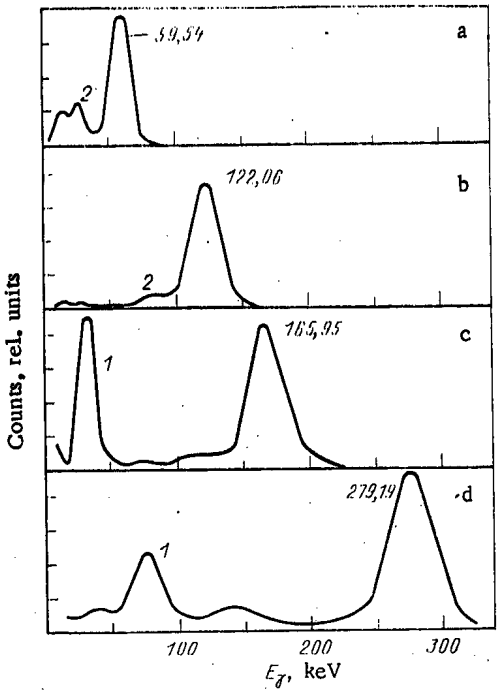


Fig. 4. Spectra of standard γ-ray sources, obtained on the detector of low-energy γ-ray quanta: a) $^{241}$Am, resolution 31.3%; b) $^{57}$Co, resolution 20.5%; c) $^{139}$Ce, resolution 19.6%; d) $^{203}$Hg, resolution 15%; 1) x-ray peak; 2) escape peak.

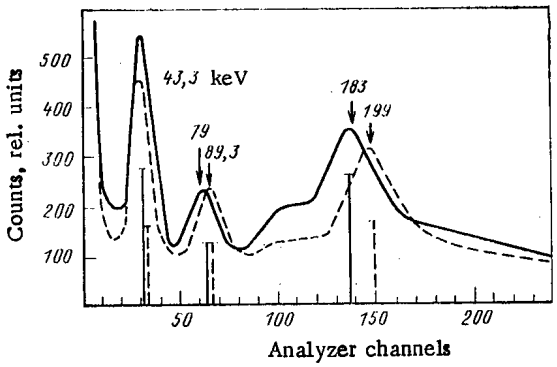


Fig. 5. Spectra obtained on the detector of low-energy γ-ray quanta for the $^{155}$Gd (n, γ) reaction (---) and $^{157}$Gd (n, γ) reaction (——). The columns beneath the peaks indicate the calculated intensities of the γ-ray lines.

In the energy range up to 160 keV the "escape" peak, which is a satellite to the main peak and appears in $^{241}$Am and $^{57}$Co spectra, is of major importance. This peak is connected with the escape, from the surface layer of the NaI crystal, of an x-ray quantum when the K-shell, which is ionized by the γ-ray quanta under study, is occupied by L electrons.

Figure 5 shows the γ-ray spectrum in the energy range up to 300 MeV measured for $^{155}$Gd (n, γ) and $^{157}$Gd (n, γ) reactions in coincidence with the detector Romashka. These spectra are characterized by a peak at 43.3 keV caused by the x-ray quanta that are formed as a result of the internal conversion for the $4^+ - 2^+ - 0^+$ transitions. The internal conversion coefficient for the $4^+ - 2^+$ transition is 15-20% while for the $2^+ - 0^+$ transition it is 60-

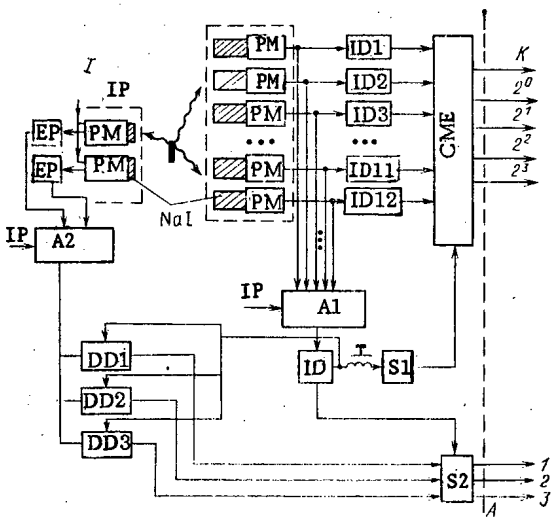


Fig. 6. Schematic of electronics.

70%. It must be pointed out that the ratio of the areas of the peaks, determined by subtracting the smoothed base beneath them, in the spectra in Fig. 5 coincides with the estimates obtained with the aid of the known intensities of the γ-ray transitions [3], the detection efficiency, the internal conversion coefficients [4], and the probability of the escape of γ-ray quanta from the specimens. The bases beneath the peaks are caused by the Compton scattering of high-energy γ-ray quanta from the capture of neutrons in structural materials. Experiments and estimates showed that the main contribution to the base ($\geqslant$50%) is made by the first component. The contributions of the other components is smaller and depends on the specific conditions.

In order to select the cascades that pass through the separate lower-lying states of the nucleus and to suppress the background of the (n, γ) reaction events studied we made the selection on the basis of the following criteria:

1) the existence of a coincidence between the signals in Romashka and in the detector of low-energy γ-ray quanta;

2) discrimination of an energy $E_\gamma \geqslant 60$ keV in one section of the detector Romashka;

3) discrimination, in all the sections of Romashka, of a total energy $E_\Sigma$ above the threshold established within the limits 0.5-1.5 MeV;

4) correspondence between the total amplitude (from both scintillation blocks) from the detector of low-energy γ-ray quanta and the energy of the distinguished lower transitions.

The existence of coincidences between the two detectors is the main factor in the suppression of the background in the arrangement. Because a low threshold $E_\Sigma$ was used the coincidences made it possible to increase the detection efficiency and also to do without the shielding usually employed to absorb the neutrons scattered by the specimen. The influence of the coincidences leads to a sharp reduction of the background to about 1.5 MeV in the region of $E_\gamma$.

Beam-Collimation System and Detector Shielding. The collimation system ensures that the beam from the entire area of the moderator is converged to an 8 × 1-cm cross section in the region of the specimen. This is accomplished by the application of four collimators in the evacuated tube of the neutron guide and regulated-slit collimator set up in front of the detector Romashka. The four collimators are filled with boric acid, boron carbide, and iron shot. The regulated-slit collimator is made of thin-walled steel boxes filled with boron carbide.

Lead "shadow" shielding of diameter 50 mm and length 400 mm, set up in front of the target of the accelerator, protects the detector from the γ-ray quanta that are formed in the uranium target of the accelerator.

A boron carbide filter, which effectively absorbs neutrons of less than 2 eV, is used to eliminate the influence of "recycled" neutrons.

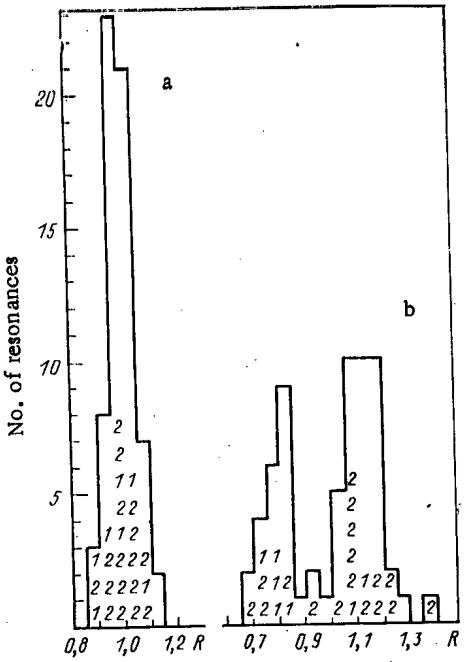


Fig. 7. Resonance distribution of intensities of cascades passing through the $2^+$ state (a) and the $4^+$ state (b). The values of the spins 1 and 2 for the resonances in which they were determined are indicated and the relative values of R are normalized so that their average is 1.

Electronics. The schematic of the electronics is shown in Fig. 6. It ensures that the conditions for the detection of (n, γ) reaction events are satisfied.

Signals from the sections of Romashka are fed into integral discriminators $ID_i$ (i = 1, 2, 3, ..., 12) and simultaneously to a linear adder A1. The operation thresholds of the discriminators are set at the same level, corresponding to $E_\gamma \approx 60$ keV. The amplitudes of the signals at the inputs of adder A1 are also set at one level with the aid of regulators integrated into them. Pulses from the output of adder A1 travel to an integral discriminator ID on which a threshold $E_\Sigma$ is set. The pulses thus generated serve as control pulses for a number of circuit elements.

The values of the coincidence multiplicity in Romashka are generated by a circuit called a coincidence multiplicity encoder (CME). The same circuit also generates (for single signals) the codes of the numbers of the sections in Romashaka that are used to monitor the operation of the detector. Signals are fed into the encoder from the discriminators $ID_i$. The encoder is triggered by control pulses from the ID. The coincidence multiplicity or section number codes enter the computer input.

Pulses from the detector of low-energy γ-ray quanta enter the circuit of the linear adder A2. The addition of signals from the scintillation blocks of the detector lead to a loss of information about the place of detection of γ-ray quanta and about their number but does make it possible to establish the arrival of a cascade at the $4^+$ or $2^+$ level of the fundamental rotational band. The signals are selected according to amplitude by three differential discriminators DD that are designed for the range of amplitudes of pulses from the γ-ray transitions under study and the range of the background for higher energies. The differential discriminators operate in coincidence with the control signals from the discriminator ID. After passing through the shaper S2 the signals from the differential discriminators enter the computer as an amplitude attribute A.

In order to reduce the consequences from the initial burst of γ-ray quanta in the accelerator target all the amplification channels and the scintillation blocks of the detector of low-energy γ-ray quanta are blocked for the duration of the burst (inhibit pulses IP in the schematic of Fig. 6).

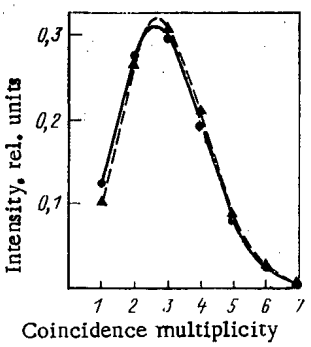


Fig. 8. Coincidence multiplicity spectra, averaged over the resonances, for the $^{155}$Gd (n, $\gamma$) reaction.

Program for Data Acquisition and Recording on an SM-4 Computer. A stream of events of different types passes through the SM-4 computer during the experiment. The tasks of the program is to isolate the necessary events and to sort them and record them in the computer memory.

The code of an event includes the time of flight T of the neutron, the amplitude attribute A, and the multiplicity K of coincidences of pulses in Romashka. The maximum number of channels in which encoding occurs is 16,384 for T, up to 5 for A, and up to 12 for K. The necessary memory capacity thus comes to 960K, which is much larger than the internal memory of the SM-4 computer. This was decreased by reducing the 16,384 time channels to 256 time channels, correspnding to selected neutron resonances. The range of multiplicities of coincidences was also reduced to eight (seven values of the multiplicity of coincidences and one value corresponding to the total effect for multiplicities of 8 to 12). This reduction was subtantiated by the fact that the effects for $K \geqslant 7$ were already small. As a result the necessary capacity of the internal memory was reduced to 16K. The conditions for the selection of events thus were: $16{,}384 \geqslant T > 0$, $5 \geqslant A > 0$, and $12 \geqslant K > 0$. Events that did not satisfy these conditions were discarded.

The complete spectrum consists of regions that correspond to different A, each of which contains eight subspectra that correspond to different K. A 256-channel time spectrum is contained in each subspectrum. A control time spectrum 4096 channels long, located in the most informative region of the neutron flight time, is also formed.

After the experiment the information is rewritten onto magnetic tape for subsequent processing on another computer.

Study of $\gamma$-Ray Cascades of $^{155}$Gd Neutron Resonances. The capabilities of the method were tested during the study of $\gamma$-ray cascades on neutron resonances of the $^{155}$Gd (n, $\gamma$) reaction [5]. Intense E2 transitions between $4^+$, $2^+$, and $0^+$ levels in the fundamental rotational band served as the $\gamma$-ray transitions by which the $\gamma$-ray cascades under study were distinguished. Results were obtained for 64 neutron resonances in the energy range up to 220 eV. The experimental data made it possible to obtain the following information for each of the resonances studied: intensity of the $\gamma$-ray cascades passing through $4^+$ and $2^+$ states (in relative numbers of $\gamma$-ray cascades per neutron capture) and coincidence multiplicity spectra. The intensity I ($4^+$) of the $\gamma$-ray cascades formed two groups, the average values for which differed by a factor of 1.3. At the same time the intensities I ($2^+$) grouped around one average value (Fig. 7).

The measured coincidence multiplicity spectra gave the following picture. Their changes from resonance to resonance turned out to be small and did not reveal a tendency toward grouping. Figure 8 presents the experimental spectra averaged over all the resonances studied for cascades that passed through the $2^+$ state (●) and the $4^+$ state (Δ). The average values of the numbers of $\gamma$-ray quanta in the first stage of a cascade can be estimated to be close to three.

The experimental data are consistent with the results of computer simulation (by the Monte Carlo method) of cascades in the $^{155}$Gd (n, $\gamma$) reaction. The calculations were per-

formed on a model based on generally accepted assumptions [6-10]. The calculated intensities I ($4^+$) formed two separate groups, corresponding to resonance spins of $1^-$ and $2^-$ with average values in a ratio of 1.46, which is in agreement with the experiment. The calculated values of I ($2^+$) also formed two groups for two spin systems of resonances but with average values in a ratio of 1.05. For this value of the ratio the experimental fluctuations can easily lead to mixing of the two groups. Comparison of our data with the known values of the spins [11] indicates that for 16 of the 23 resonances the observed grouping of intensities of cascades can be attributed to the spin dependence. For the other seven resonances there is a distinct deviation, whose cause is not yet clear.

The example of measurements described here indicates that the method developed for the study of $\gamma$-ray cascades can yield interesting physical results.

In conclusion, the authors wish to thank V. F. Gerasimov and A. N. Pastukhov for collaboration and assistance in the automation of the experiments.

LITERATURE CITED

1. G. V. Muradyan, At. Energ., 59, No. 6, 394 (1981).
2. Yu V. Adamchuk et al., in: Neutron Physics [in Russian], Part 3, TsNII-atominforma, Moscow (1977), p. 113.
3. Nuclear Data Tables, A5, No. 1, 162 (1968).
4. Atomic Data and Nuclear Data Tables, 21, Nos. 2-3 (1978).
5. V. V. Danilin et al., Neutron Physics [in Russian], Part 3, TsNII-atominforma, Moscow (1983), p. 25.
6. W. Ponitz, Z. Physik, 197, 262 (1966).
7. D. Sperber, Nucl. Phys., A90, 665 (1967).
8. C. Coceva et al., Nucl. Phys., A117, 586 (1968).
9. R. Clark and D. Gill, Nucl. Phys., A213, 349 (1974).
10. E. Nardy et al., Nucl. Phys., A237, 419 (1975).
11. Neutron Cross Sections, BNL-325, Vol. 1 (4th ed.) (1981).

# RADIATIVE CAPTURE CROSS SECTION OF FAST NEUTRONS BY $^{197}$Au, $^{236}$U AND $^{237}$Np NUCLEI

A. N. Davletshin, A. O. Tipunkov, S. V. Tikhonov, and V. A. Tolstikov

UDC 539.125.5

Introduction. The necessity for investigating the radiative capture reactions of fast neutrons, studied by us, is determined mainly by the requirements of nucler power generation based on fast reactors. In the buildup chains of $^{232}$U, $^{236}$Pu, and $^{238}$Pu, a knowledge of the amount of which is important for the conditions of reprocessing the recycled fuel of fast reactors, $\sigma_{n,\gamma}$ of fast neutrons for $^{236}$U and $^{237}$Np plays an important role. The requirements on the accuracy of the estimated values of these cross sections are given in Table 1.

Obviously, it should be assumed that information about the errors of the estimated values of these cross sections is not sufficiently accurate, since the estimates are made on the results of one or two experimental works, the data of which do not agree between themselves.

$^{236}$U. In the range 0.3-3.0 MeV, the data of [1, 2] obtained by the activation method gave poor agreement between themselves. For $E_n < 20$ keV, there are the data of [3], obtained by the time of flight method. Finally, work was published recently [4], carried out by the method of moderation time in lead, the results of which relate to the range $E_n < 50$ keV.

$^{237}$Np. The energy range >0.2 MeV was investigated in [5, 6], the results of which disagree by 20-250%. For $E_n < 0.2$ MeV, data of unpublished papers by M. Hofman (1971) and P. Weston (1979), differing by a factor of 2 approximately, are given in graphical form in [7].

Translated from Atomnaya Énergiya, Vol. 58, No. 3, pp. 183-188, March, 1985. Original article submitted June 18, 1984.

 0038-531X/85/5803-0216$09.50 

TABLE 1. Required and Achieved Errors in the Estimated Values of the Radiative Capture Cross Sections

| Nuclide | Energy range, keV | Error, % | | Application |
|---|---|---|---|---|
| | | required | attained | |
| $^{197}$Au | 200—500 | 2 | 6,1 | Nuclear standard |
| | 500—1000 | 2 | 4,1 | |
| | 1000—2500 | 2 | 20 | |
| $^{236}$U | 500—5000 | 4 | 40 | Fuel cycle |
| $^{237}$Np | 500—5000 | 10 | 40 | Fuel cycle |

This brief review shows that at the present time there is not a sufficient number of published results for obtaining reliable estimated data about the radiative capture cross sections of neutrons by $^{236}$U and $^{237}$Np. An experimental estimate of the errors of the one-group radiative capture cross section of $^{236}$U and $^{237}$Np by averaging over a fast reactor spectrum amounts to ±40% [8].

The $\sigma_{n,\gamma}$ cross section of $^{197}$Au is used as a nuclear standard in measurements of the neutron cross sections of other nuclei. For $E_n > 0.1$ MeV the cross section obtained in experiments with moderate resolution depends quite smoothly on $E_n$ and is known with satisfactory accuracy, and therefore its measurement is a good verification of the procedure used. On the other hand, the errors of the estimated values of this cross section [9] are considerably greater than rquired. Moreover, analysis shows that data about the errors must be assumed to be insufficiently substantiated and, consequently, additional information about $\sigma_{n,\gamma}$ $(E_n)$ for $^{197}$Au will prove to be useful. These circumstances also have led to the appearance of the present paper.

Measurement Procedure. The cross sections of the reactions $^{236}$U (n, $\gamma$)$^{237}$U and $^{237}$Np (n, $\gamma$)$^{238}$Np are measured by the activation method. The experiment was conducted in such a way that during the irradiation of the uranium (or neptunium) sample the neutron flux was measured simultaneously by the reactions $^{197}$Au (n, $\gamma$)$^{198}$Au (disk sample) and $^{1}$H (n, n)$^{1}$H (proportional counter). It is clear that in this experiment there existed the possibility of determining the $\sigma_{n,\gamma}$ cross section for $^{197}$Au relative to the $\sigma_{n,p}$ cross section. The activity of the irradiated sample was measured by the accompanying $\gamma$-radiation in a Ge(Li) detector.

The radiative neutron capture cross section $\sigma_{n,\gamma}$ measured relative to the $\sigma_{n,p}$ cross section, was determined from the relation

$$\sigma_{n,\gamma}(E_n) = \frac{N_\gamma A_\gamma f(\lambda, t) N_c G_c}{\eta N_{in} N_s G_s} \sigma_{n,p}(E_n). \quad (1)$$

Here $E_n$ is the averge energy of the irradiating neutrons; $N_\gamma$, number of events recorded by the Ge(Li) detector; $f(\lambda, t)$, a factor taking account of the time of irradiation of the sample, the measurement of the induced activity and the decay constant [11]; $A_\gamma$, a correction for the activity by scattered neutrons; $\eta$, recording efficiency by the Ge(Li) detector of the corresponding $\gamma$-quanta; $N_{in}$, number of interactions in the proportional counter during irradiation of the sample [10]; N and G, number of nuclei and the geometric factors for the counter and sample; $\sigma_{n,p}$ $(E_n)$, elastic scattering cross section of the neutrons by protons [9].

The geometric factors for the counter and sample have identical form:

$$G = \frac{\nu}{N\sigma(E_n)}. \quad (2)$$

In this expression, $\nu$ is the absolute efficiency of the corresponding detector for the case of a disk isotropic source of neutrons; $\sigma$ $(E_n)$ = $\sigma_{n,p}$ $(E_n)$ [$\sigma_{n,\gamma}$ $(E_n)$] for the counter (sample), and their values are taken from any estimate. In both cases the values of $\nu$ were calculated by the Monte Carlo method for a disk isotropic neutron source and a cylindrical uniform detector, located coaxially at a certain distance from one another.

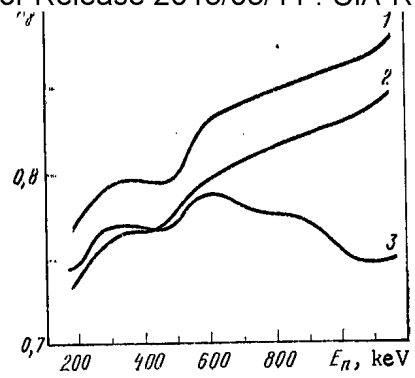


Fig. 1. Dependence of the correction $A_\gamma$ on the neutron energy for samples of $U_3O_8$ (1), Au (2) and $NpO_2$ (3)

The radiative neutron capture cross sections $\sigma_{n,\gamma}$ measured relative to the $^{197}Au$ $\sigma_{n,\gamma}$ cross section were determined from the relation

$$\sigma^x_{n,\gamma}(E_n) = \left[\frac{N_\gamma A_\gamma f(\lambda, t)}{N_s G_s}\right]_x \Big/ \left[\frac{N_\gamma A_\gamma f(\lambda, t)}{N_s G_s}\right]_{st} \times \frac{\eta_{st}}{\eta_x}\sigma^{st}_{n,\gamma}(E_n), \quad (3)$$

where the suffix x refers to the sample being investigated, and the suffix st to the standard (sample of $^{197}Au$); the values of $\sigma_{n,\gamma}$ $(E_n)$ are taken from [9] and are averaged over the energy range of the irradiating neutrons (50-100 keV). The other symbols have the same meaning as in expression (1).

Irradiation of Samples. Activity Measurement. Irradiation of the samples was conducted on the KG-2.5 accelerator, using the T (p, n) $^3He$ and $^7Li$ (p, n) $^7Be$ reactions. The target was water-cooled. The sample under investigation and the standard were positioned close to one another at a distance of 4 cm from the target in a cadmium container. The samples of $U_3O_8$ and $NpO_2$ powder were packed into stainless-steel containers. The neutron flux density at the center of the samples amounted to $(4\text{-}8)\cdot10^6$ $cm^{-2}\cdot sec^{-1}$, and the mass of the gold, uranium, and neptunium samples was 1 g, 1 g and 0.57 g, respectively.

A cylindrical proportional counter [12], just like the samples, was located coaxially with the accelerator proton beam. The front end of the counter was located at a distance of 70 cm from the target (neutron source). The counter housing was made of stainless steel and the end sections had the form of hemispheres. The internal volume was equal to 180.5 $cm^3$, the filling was pure hydrogen and the gas pressure was $1.235\cdot10^5$ Pa. During irradiation (12-20 h), the area of the recoil proton spectrum amounted to $(2\text{-}4)\cdot10^7$ pulses. The number of interactions of neutrons with protons was determined from the relation [10]:

$$N_{in} = \frac{N(x)}{\varepsilon(x) T_d A_\varepsilon(x)}. \quad (4)$$

Here N (x) is the area of the measured spectrum of the recoil protons with threshold $x = E_p/E_n$, where $E_p$ is the energy of the recoil protons; $\varepsilon$ (x), corresponding area of the normalized recoil proton spectrum, calculated by the Monte Carlo method; $T_d$, correction for the "dead" time of the spectrometric channel; $A_\varepsilon$ (x), correction to the recoil proton spectrum for the effect of scattered neutrons. This correction is measured experimentally and its value varies appreciably, depending on the value of x; in the range x = 0.2-1.0, the correction amounts to approximately 1.0-0.9. The effect of neutrons scattered at the walls of the room, the structure of the target holder, the sample and its holder, the structure of the counter, and in the air [11] is taken into consideration in it.

The induced activity was measured with respect to the line $E_\gamma$ = 208 keV for $^{237}U$ ($T_{1/2}$ = 6.75 days), with respect to the line $E_\gamma$ = 412 keV for $^{198}Au$ ($T_{1/2}$ = 2.7 days) and with respect to the line $E_\gamma$ = 984 keV for $^{238}Np$ ($T_{1/2}$ = 2.12 days). We note one special feature of the measurement of the $^{238}Np$ activity in the sample of $NpO_2$: it is necessary to take special measures to eliminate overloading of the spectrometric channel by the intense background emission of the sample. For this purpose, a filter with a thickness of 0.7 cm of mercury was used, for which the $\gamma$-quanta absorption curve has a discontinuity close to the en-

ergy of the background γ-quanta of maximum intensity. In addition, in order to reduce the loading of the amplitude–digital converter, the threshold for the analysis of the spectrum was set at the level of 770 keV.

The total correction $A_\gamma$ is introduced into the measured values of the activity in accordance with expressions (1) and (3), by which account is taken of the effects leading to an additional increase or decrease of the sample activity with respect to the main isotropic neutron source. The effects leading to an increase of activity are: scattering of neutrons at the walls of the room, in the sample, in the containers (cadmium and stainless steel), in the target holder (stainless steel and water), in the sample holder, and in the other sample being irradiated simultaneously. The effect of nonisotropicity of the neutron source was taken into account: as the samples are located at a distance of 4 cm from the target, this effect leads to a reduction of activity by 4-5%. The correction for the target holder (4-16% of the induced activity) is measured when carrying out the experiments described. The other corrections are measured in experiments [13] similar to those described in the present paper. The corrections for scattering in the samples are calculated by the Monte Carlo method.

Figure 1 shows the correction $A_\gamma$ for samples of Au, $U_3O_8$ and $NpO_2$ as a function of the neutron energy. The errors of the corrections vary from 2.7 to 1.8% with increase of the neutron energy. Attention should be paid to the significantly different energy dependences of the corrections for the samples of Au and $NpO_2$, despite the similar energy dependences of $\sigma_{n,\gamma}$ for $^{197}Au$ and $^{237}Np$ in the range of neutron energies investigated. This is due first and foremost to the difference in the energy dependences of the corrections for the target holder for the gold and neptunium samples. The energy of the neutrons scattered in the water-cooled target holder is appreciably less than the energy of the primary neutrons entering the sample. The energy dependence of the corrections is determined by the energy curve of the $\sigma_{n,\gamma}$ (E) cross section in both the energy range being investigated and in the energy range of the scattered neutrons. For the gold and neptunium samples, the dependences of the corrections on the neutron scattering in the sample holder are found to be significantly different. On the other hand, despite the fact that the energy curve of the $\sigma_{n,\gamma}$ (E) cross section for $^{238}U$ and $^{197}Au$ in the energy range investigated is different, these corrections have an identical energy curve although they are different in value. The examples considered show that taking account of the scattered neutrons, especially when their spectra differ significantly from the spectrum of the primary neutrons, is a complex problem. It can only be solved by measuring the additional activity or by performing the appropriate calculations by the Monte Carlo method for a realistic configuration of the experimental facility. In view of the complex relation between the values of the activity induced by the primary and scattered neutrons, approximate estimates or experiments may give inaccurate results.

Measurements of the Ge(Li)-Detector Efficiency. In order to calculate the cross sections by relations (1) and (3), it is nessary to know the values of the recording efficiency for γ-quanta, or their ratio, for samples of different configuration and mass, located nonidentically relative to the Ge(Li)-detector crystal. The method used for calibration of the detector with respect to efficiency did not require quantitative data about the decay schemes and quantum yields of the radiations.

$^{197}Au$. The efficiency η was determined from the ratio of the activity values of samples with identical specific activity, which were obtained with fission spectrum neutrons:

$$\eta = \frac{Am}{\alpha M}. \tag{5}$$

The activity A of a sample with mass M, identical to the samples used for irradition in the accelerator, was measured in the Ge(Li) detector. The absolute activity $\alpha$ of a foil with mass m was determined by the $4\pi\beta$–γ coincidence method. A value of $\eta = 3.05 \cdot 10^{-2} \pm 1.5\%$ was obtained.

$^{237}Np$. The ratio of the recording efficiency $\eta_{st}/\eta_x$ was determined in the following way. Samples of Au and $NpO_2$, which were used in the accelerator experiments, were obtained with thermal neutrons. Irradiation of the samples was conducted separately and the flux was monitored with gold foils. The activity of the samples was measurd with a Ge(Li) detector and $\eta_{st}/\eta_x$ was determined from the ratio

$$\eta_{st}/\eta_x = \left(\frac{AK}{\sigma^T}\right)_{st} \Big/ \left(\frac{AK}{\sigma^T}\right)_x, \tag{6}$$

TABLE 2. Results of Cross Section Measurements for U, Np, and Au

| Neutron energy, keV | $\sigma_{n,\gamma}$ $^{236}$U, mb | | $\sigma_{n,\gamma}$ $^{237}$Np, mb | | $\sigma_{n,\gamma}$ $^{197}$Au, mb, rel. to $\sigma_{n,p}$ | Ref. cross section | |
|---|---|---|---|---|---|---|---|
| | rel. to $\sigma_{n,\gamma}$ $^{197}$Au | rel. to $\sigma_{n,p}$ | rel. to $\sigma_{n,\gamma}$ $^{197}$Au | rel. to $\sigma_{n,p}$ | | rel. to $\sigma_{n,\gamma}$ $^{197}$Au, mb | $\sigma_{n,p}$, b |
| 166±37 | 223±10,7 | — | — | — | — | 253,1±10 | — |
| 168±35 | 213±10,7 | 254±4,1 | — | — | 300±4,1 | 251,5±10 | 10,45±1 |
| 174±30 | 208±10,7 | 251±4,1 | 791±11,9 | — | 295±4,1 | 247,1±10 | 10,29±1 |
| 206±26 | 205±7,1 | — | 751±8,8 | — | — | 245,5±6,1 | — |
| 240±24 | 194±7,1 | — | 687±8,8 | — | — | 234,4±6,1 | — |
| 354±41 | 174±6,9 | 188±3,8 | 555±8,8 | 594±6,9 | 194±3,7<br>192±3,7 | 179,6±6,1 | 7,36±1 |
| 459±36 | 153±6,8 | — | — | — | — | 142,7±6,1 | — |
| 472±38 | — | — | 374±8,7 | 403±6,8 | 151±3,6 | 140,4±6,1 | 6,33±1 |
| 483±38 | — | — | 383±8,7 | 403±6,8 | 145±3,6 | 138,0±6,1 | 6,25±1 |
| 551±51 | 161±5,1 | 158±3,6 | 326±7,4 | 326±6,8 | 122±3,6<br>125±3,6 | 124,7±4,1 | 5,84±1 |
| 718±44 | 177±5,1 | — | 217±7,4 | 214±6,8 | 96,4±3,5 | 99,0±4,1 | 5,08±1 |
| 890±43 | 163±5,1 | 178±3,5<br>178±3,5 | 159±7,3<br>— | 175±6,8<br>171±6,8 | 93,2±3,5<br>94,3±3,5<br>— | 85,8±4,1<br>— | 4,53±1<br>— |
| 897±31 | — | — | — | — | — | — | 4,51±1 |
| 1046±45 | 149±7,7 | 153±3,6 | 119±7,7 | 119±6,8 | 82,8±3,5<br>80,9±3,5 | 81,3±7 | 4,16±1 |
| 1146±38 | 126±7,7 | 132±3,6 | 106±7,7 | 110±6,8 | 80,9±3,5<br>80,9±3,5 | 77,8±7 | 3,97±1 |

Note. The error is given in percentages.

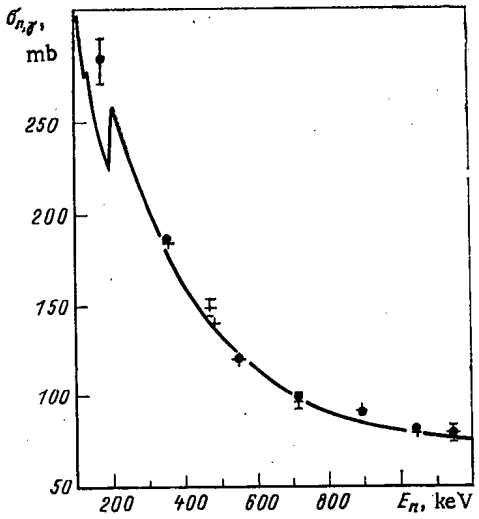


Fig. 2. Radiative neutron capture cross section of $^{197}$Au: ●) experiment (with irradiation with samples of $U_3O_8$; +) experiment (with irradiation with samples of $NpO_2$); ——) ENDF/BV estimate [9].

where A is the activity of the sample, corrected for activation by epicadium neutrons; K, a correction for self-screening of the thermal neutron flux in the sample; $\sigma^T$, activation cross section by thermal neutrons. Values of the cross sections $\sigma^T$ ($^{237}$Np) = 181 ± 9 b [7], $\sigma^T$ ($^{197}$Au) = 98.8 ± 0.3 b [14] were used. As a result, $\eta_{st}/\eta_x$ = 49.75 ± 5.5% was obtained.

The recording efficiency η was calculated from the measured values of $\eta_{st}/\eta_x$ and $\eta_{st}$ ($\eta_{st}$ is the recording efficiency for samples of Au). The value of η determined from these data is $6.13 \cdot 10^{-4}$ ± 5.7%.

$^{236}$U. The recording efficiency was found from the ratio of the values of the activity of known volumes of a solution in which the concentration of $^{237}$U is identical:

$$\eta = \frac{Av}{aV} \qquad (7)$$

In order to determine the absolute activity $a$ of the volume v, the $4\pi\beta-\gamma$ coincidence method was used. A solution of $^{237}U$ in $HNO_3$ deposited on plastic film, metallized with gold, was used. The thickness of the film was $\sim$10 $\mu g/cm^2$ and the thickness of the active layer was $\sim$1.0 $\mu g/cm^2$. The coincidence of the $^{237}U$ $\beta$-particles with $\gamma$-quanta with $E_\gamma$ = 208 keV and the KX-quanta of $^{237}Np$ with $E_\gamma$ = 103 keV was investigated. This version of the method for determining the absolute activity of $^{237}U$ was used for the first time. Almost coincident values of the absolute activity were obtained.

A sample, the activity of which was measured in the Ge(Li) detector, was prepared from $^{238}U$ in the form of $U_3O_8$ contained in the dry residue of a solution with $^{237}U$ with a volume V. It was placed in the same container in which there was a sample of $^{236}U$ in the form of $U_3O_8$, having been irradiated in the accelerator. As a result of the measurements made, $\eta = 1.40 \cdot 10^{-2} \pm 1.6\%$.

The ratio of the recording efficiency values $\eta_{st}/\eta_x$ was determined by two methods. The first method is similar to that used for the neptunium samples. For this, the values of the thermal cross sections $\sigma^T$ ($^{236}U$) = 5.2 ± 0.3 b and $\sigma^T$ ($^{197}Au$) = 98.8 ± 0.3 b [14] were used. In the second method, $\eta_{st}/\eta_x$ was calculated from the independently measured values of $\eta_{st}$ and $\eta_x$ (see above). In this case, $\eta_{st}/\eta_x$ = 2.18 ± 2.2%. When processing the experimental data, the latter value was used, as, for this method, possible systematic errors are less random.

Measurements Results. Table 2 gives the values of the radiative neutron capture cross sections for the nuclei $^{236}U$ and $^{237}Np$, measured relative to $\sigma_{n,p}$ and $\sigma_{n,\gamma}$ for $^{197}Au$, and for nuclei of $^{197}Au$ relative to $\sigma_{n,p}$. The spread of the energy values shown in the table is the spread of the energies of the outgoing neutrons from the target at an angle of 0°. The reference values of the $^{197}Au$ $\sigma_{n,p}$ cross sections are averaged over the corresponding range of neutron energies of the cross section, and $\sigma_{n,p}$ are obtained by interpolation for the average value of the neutron energy.

The errors of the measured cross sections given in Table 2 are obtained by quadratic summation of the errors of the quantities in expressions (1) or (3): $\delta N_\gamma$ for the gold, uranium, and neptunium samples are equal to 0.7, 1.4, and 2%, respectively; $\delta N_{in}$ = 2.0, $\delta N_C$ = 1.1, $\delta N_S$ = 0.1, $\delta G_C$ = 0.3, and $\delta G_S$ = 0.6%. For the other parametes, the error values are given earlier in the text.

Discussion of Results. Conclusions. $^{197}Au$. The measured values of $\sigma_{n,\gamma}$ $^{197}Au$ and the total errors for certain energy values are shown in Fig. 2. They agree satisfactorily with the ENDF/BV estimate within the limits of error, with the exception of individual values. This can be taken as proof of the absence of significant systematic errors in the measurement procedure for the cross sections $\sigma_{n,\gamma}$ $^{236}U$ and $^{237}Np$. The spread of the cross section values, obtained for identical energies in independent series of measurements, shows that the estimates of the random errors given above for $\delta N_\gamma$ and $\delta N_{in}$ are completely objective.

The energy $E_n$ = 200 keV delimits the regions in which the procedures for obtaining the estimated data were different. If account is taken of the coincidence of our results with the ENDF/BV estimate for other neutron energy values, then the marked difference between the measured cross section value and the estimated value for $E_n$ = 168 keV, in our opinion, confirms that the estimate of the cross section in the vicinity of this energy value has been performed unsatisfactorily.

$^{236}U$. Figure 3 shows the existing experimental data, the estimated data, and the results of a theoretical calculation for the $\sigma_{n,\gamma}$ cross section of $^{236}U$, for the range of energies studied. Our experimental data, measured relative to $\sigma_{n,\gamma}$ for $^{197}Au$ and $\sigma_{n,p}$, agree well between themselves. Differences appear only to the same degree as our measured values of $\sigma_{n,\gamma}$ for $^{197}Au$ differ from the ENDF/BV estimate (see Fig. 2). The values of the cross sections obtained by us are a factor of 1.6-2 less than the estimated values, which were determined on the basis of the results of [1, 2].

For the purpose of analyzing the complicated situation, calculations were performed of the cross sections based on the statistical theory of nuclear reactions described in detail in [15]. For this, values of the distance between levels $D_{obs}$ (see Fig. 3) were used, which are close to the recent estimates of the experimental data: 15 ± 1 eV [16] and 16.2 ± 0.8 eV [17]. Satsisfactory agreement was obtained with our results and also with the results of [4] for $E_n < 50$ keV. The description of the experimental data from [1, 2] is achieved with $\bar{D}_{obs}$ less by a factor of 2 than the values given previously. Thus, the values of $\sigma_{n,\gamma}$ ($E_n$) for $^{236}U$ obtained by us confirm that the existing estimates of this cross section in the region of fast neutrons clearly are over-estimated by 40-50% and require revision.

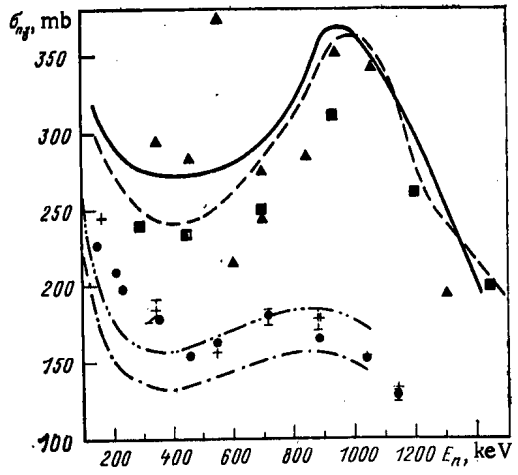


Fig. 3. Radiative neutron capture cross section of $^{236}U$: •, +) experimental data of the present paper relative to $\sigma_{n,\gamma}$ of $^{197}Au$ and $\sigma_{n,p}$ respectively; ■) data of [1]; ▲) data of [2]; —— ,---) ENDF/BV and ENDL-78 estimates; —·—, —··—) calculation from [15] for $\bar{D}_{obs}$ = 18 eV and 15 eV.

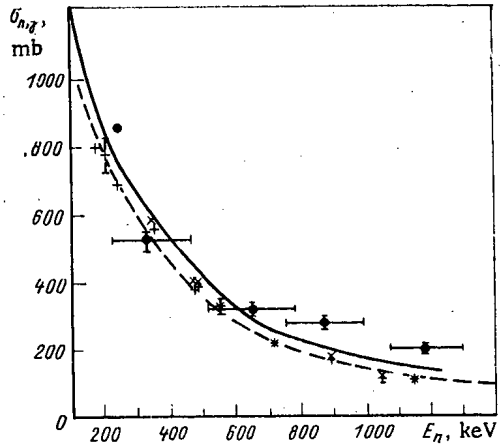


Fig. 4. Radiative neutron capture cross section of $^{237}Np$: +, ×) experimental data of the present paper, relative to $\sigma_{n,\gamma}$ and $\sigma_{n,p}$ respectively; •) data of [18]; ——, ---) estimates of [7] and ENDF/BV.

$\frac{^{237}Np}{^{237}Np}$. Figure 4 shows the results of our experiments and the existing estimates of the $\sigma_{n,\gamma}$ cross section. The total random error of the experiment, indicated in the figure, amounts to 6.5-6.1% with a change of neutron energy from 0.16 to 1.15 MeV. The degree of agreement and difference of the results of the measurement relative to $\sigma_{n,\gamma}$ for $^{197}Au$ and $\sigma_{n,p}$ are just the same as for $\sigma_{n,\gamma}$ $^{236}U$.

Our results, over almost the whole range, agree well with the ENDF/BV estimate but are 6-33% less than the estimate from [7]. We note that in this estimate, in place of the experimental data computed in ENDF/BV, information is used from an unpublished paper by P. Weston and J. Todd (1979), the results of which refer to the neutron energy range 1-500 keV.

The results of [18], which is similar in procedure to ours for carrying out the experiment, also are shown in Fig. 4. Samples of smaller mass are located at the same solid angles

but differ slightly in composition [$NpO_2(NO_3)_2$]. The neutron sources are identical but the target is three times as thick. Calibration of the Ge(Li) detector for efficiency was carried out with a standard γ-radiation source. It is not clear from the text of the paper how the correction was applied for absorption of quanta with $E_\gamma$ = 984.4 keV in the lead-cadmium filter used. We note that in our calibration procedure the introduction of this correction is not required. The contribution to the activation of the samples from scattered neutrons is determined in an indirect way. The considerable difference between our data and the results of [18], in our opinion, can be explained by any difference in the procedural details mentioned above, but first and foremost by the method of introducing the correction for scattered neutrons.

The analysis carried out of the experimental and estimated data for the radiative neutron capture cross sections investigated by us leads to a conclusion about the necessity for conducting new experiments. In this case, a wide overlap of the energy ranges of the measurements is desirable, based on the activation and time of flight procedures. Particular attention should be paid to the elimination and reduction of the systematic errors of the experiment. For the activation measurements, this means the use of variants of the procedure with reduction of the effect of scattered neutrons and the use of different reference cross sections.

The authors thank V. V. Tuzhilov for active participation in carrying out the measurements and processing the results.

## LITERATURE CITED

1. D. Stupegia et al., J. Nucl. Energy, 15, No. 4, 200 (1961).
2. J. Barry et al., Proc. Phys. Soc., 78, 503, 801 (1961).
3. A. Carlson et al., Nucl. Phys., A141, 577 (1970).
4. A. A. Bergman et al., Problems of Nuclear Science and Technology, Series Nuclear Constants [in Russian], No. 1 (45) (1982), p. 3.
5. D. Stupegia et al., Nucl. Sci. Eng., 29, No. 2, 218 (1967).
6. M. Lindner et al., Nucl. Sci. Eng., 59, 381 (1976).
7. H. Derrien and E. Fort, in: Proc. Int. Conf. on Neutron Cross Sections and Technology, Knoxville (1980), p. 872.
8. A. I. Voropaev et al., Problems of Nuclear Science and Technology, Series Nuclear Constants [in Russian], No. 3 (34) (1979), p. 34.
9. Nuclear Data Standard for Nuclear Measurements, 1982, in: Tech. Rep. Ser. N 227, IAEA, Vienna (1983), p. 37.
10. A. Lorenz, INDC(NDC)-108/N, IAEA, Vienna (1979).
11. A. N. Davletshin and V. A. Tolstikov, At. Energ., 42, No. 1, 43 (1977).
12. S. N. Baikalov et al., in: Metrology of Neutron Radiation in Reactors and Accelerators, Proceedings of the Second All-Union Conference [in Russian], Moscow, Vol. 1 (1974), p. 58.
13. A. N. Davletshin et al., At. Energ., 48, No. 2, 113.
14. S. Mughabghab and D. Garber, Neutron Cross Sections, Resonance Parameters, BNL-325, Vol. 1 (1973).
15. O. T. Grudzevich et al., Problems of Nuclear Science and Technology, Series Nuclear Constants [in Russian], No. 2 (51) (1983), p. 3.
16. V. Benzi, in: Proc. Int. Conf. on Neutron Physics and Nuclear Data for Reactors and Other Applied Purposes, Harwell (1978), p. 288.
17. G. V. Antsipov et al., Preprint No. 2, Izd. Akad. Nauk Belorus. SSR, A. V. Lykov Institute of Theoretical and Mathematical Problems, Minsk (1982).
18. Yu. N. Trofimov and Yu. A. Nemilov, in: Neutron Physics [in Russian], TsNIIatominform, Moscow (1984), pp. 142-146.

# A MATHEMATICAL MODEL FOR CALCULATING STRESSES IN THE MICROFUEL ELEMENTS

V. S. Eremeev, E. A. Ivanova,
V. N. Mikhailov, A. P. Putilova,
and A. S. Chernikov

UDC 621.039.548

The efficiency of the spherical microfuel elements of the VTGR depends to a large extent on the stress (stress-strain) state of the coatings of the microfuel elements [1-3]. A stringent formulation of the problem of stress computation consumes a lot of computer time [2]. In the less general modes of treatment (see, for example, [3-5]) certain restrictions are imposed on the number of layers, the type of the rheological model, and the method of assigning the physicomechanical properties and the service conditions. In this note, we present a mathematical model of the stress state of the microfuel elements with an arbitrary number of layers that requires a relatively less computation time.

In view of the fact that the buffer layer in the microfuel elements is usually not considered, the problem reduces to the stress analysis in a sphere consisting of M layers. Let us assume that the physicomechanical properties of the material remain unchanged within the bounds of each layer, and that there is a strong bond between the layers. Each layer is characterized by a certain number of properties including Young's modulus E, Poisson's ratio $\nu$, the radiation creep constant $K_p$, the coefficient of thermal expansion $\alpha^{(i)}$, and the shrinkage of the material under the action of neutron radiation $\eta^{(i)}$. The superscript i indicates the radial direction (i = r) or the direction perpendicular to it (i = $\theta$).

Let us assume that the stress sources include the gas pressure $p_1$ transmitted to the internal surface of the first dense layer and the pressure $p_2$ acting from the graphite matrix of the fuel element on the external surface of the M-th layer, and that the temperature T remains constant within the boundaries of the layer. We consider that we know the time dependences of the fluence $\Phi(t)$, the temperature T(t), and the parameters E, $\alpha^{(i)}$, and $\eta^{(i)}$.

In the spherical coordinate system (r, $\theta$), the magnitude of the stress-induced strains is determined by the following equations:

$$\varepsilon_\theta = \frac{1-\nu}{E}\sigma_\theta - \frac{\nu}{E}\sigma_r + \alpha_\theta (T - T_*) + \eta_\theta + \int_0^{\Phi_0} [K_p (1-\nu_p)\sigma_\theta - K_p \nu_p \sigma_r]\, d\Phi; \quad (1)$$

$$\varepsilon_r = -\frac{2\nu}{E}\sigma_\theta + \frac{1}{E}\sigma_r + \alpha_r (T - T_*) + \eta_r + \int_0^{\Phi_0} (-2K_p \nu_p \sigma_\theta + K_p \sigma_r)\, d\Phi,$$

where $\nu_p$ is a constant characterizing the degree of radiation creep in the direction normal to the loading direction; and T* is the deposition temperature of the layer. Introducing the notation $\Gamma^{(i)} = \eta^{(i)} + \alpha^{(i)}(T - T^*)$ and $z = (1/2)r^2 d^2\sigma_r/dr^2 + 2r d\sigma_r/dr$, we obtain a system of M − 1 (according to the number of layers) equations of the type

$$\frac{1-\nu}{E} z + \int_0^{\Phi_0} K_p (1-\nu_p)\, z\, d\Phi + \Gamma^{(\theta)} - \Gamma^{(r)} + r\frac{d\Gamma^{(\theta)}}{dr} = 0. \quad (2)$$

In view of the fact that according to the condition of the problem $\Gamma^{(i)}$ does not depend on r, the quantity z, which is the solution of Eq. (2), also does not depend on r, and owing to this, the stresses are described by the equations published earlier [5]:

$$\sigma_r^{(k)} = C_1^{(k)} + \frac{C_2^{(k)}}{r^2} + \frac{2}{3} z^{(k)} \ln r;$$

Translated from Atomnaya Énergiya, Vol. 58, No. 3, pp. 189-190, March, 1985. Original article submitted December 19, 1983.

 0038-531X/85/5803-0224$09.50 

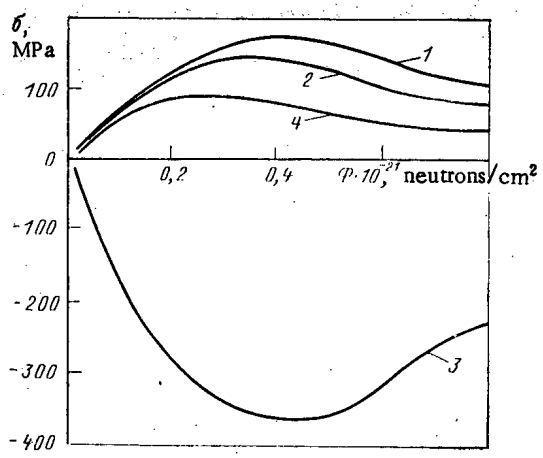


Fig. 1. Dependence of the circumferential stresses on the internal surface of different coating layers of the microfuel element on the fluence of fast neutrons: 1) the second layer of PyC; 2) the third layer of PyC; 3) the fourth layer of SiC; 4) the fifth layer of PyC.

$$\sigma_\theta^{(k)} = \sigma_r^{(k)} - \frac{3}{2}\frac{C_2^{(k)}}{r^3} + \frac{1}{3}z^{(k)}. \qquad (3)$$

Let the coordinate r in the layer k vary from $r_{r-1}$ to $r_k$. Let us denote the radial stresses on the interlayer boundaries through $\varkappa_{k-1} = \sigma_r^{(k)}(r_{k-1})$, $\varkappa_k = \sigma_r^{(k)}(r_k)$. From the obtained system of algebraic equations and Eq. (3), we determine the constants $C_i^{(k)}$ as a function of $C_i^{(k)}(\varkappa_{k-1}, \varkappa_k)$. According to the definition of the problem, $\varkappa_1 = -p_1$, and $\varkappa_M = -p_2$. We shall find the other values of $\varkappa_i$ by examining the first one of Eqs. (1) for two successive (neighboring) values of the fluence $\Phi_s$ and $\Phi_{s-1}$. Subtracting one equation from the other and replacing the integral using the trapezoid formula, we obtain an expression of the type

$$\frac{u^{(s+1)} - u^{(s)}}{r} = A^{(s+1)}\sigma_\theta^{(s+1)} - B^{(s+1)}\sigma_r^{(s+1)} - \overline{A}^{(s)}\sigma_\theta^{(s)} + \overline{B}_r^{(s)}\sigma_r^{(s)} + \Gamma_\theta^{(s+1)} - \Gamma_\theta^{(s)}, \qquad (4)$$

where $A^{(i)}$, $\bar{A}^{(i)}$, $B^{(i)}$, $\bar{B}^{(i)}$ are the known functions at a fluence $\Phi_s$ (i = s) and $\Phi_{s+1}$ (i = s + 1).

We shall write down Eq. (4), which is valid for each layer, for the points r = $r_k$, subsequently expressing $\sigma_i$ through $\varkappa_k$ taking the equality of radial displacements on the boundary of the successive layers into account We then obtain a system of "chart"-type equations with regard to the unknown radial stresses for the fluence $\Phi_{s+1}$ at the known stresses for the fluence $\Phi_s$.

A numerical solution of the problem was obtained using the NAP computer program written in the FORTRAN IV language. The computation was carried out for a five-layer microfuel element having the following parameters: a $UO_2$ core measuring 500 μm in diameter; the first buffer layer made of pyrocarbon PyC ($\rho$ = 1.1 g/cm³) with a thickness of 90 μm; the second layer made of PyC ($\rho$ = 1.5 g/cm³) – 35 μm; the third layer made of PyC ($\rho$ = 1.8 g/cm³) – 45 μm; the fourth layer made from a high (Young's) moduus material – 50 μm; and the fifth layer made of PyC ($\rho$ = 1.8 g/cm³) – 60 μm. The dependence of Young's modulus on the fluence was taken into account in the calculations. Other material properties and the radiation conditions were taken close to those used in similar calculations [3, 5].

Based on the calculations made for the microfuel elements incorporating different materials in the fourth layer (oxides, nitrides, and carbides), we conclude that the stresses $\sigma_\theta$ are maximum when oxides (MgO, BeO, $ZrO_2$, $Al_2O_3$) are used, and are somewhat reduced when nitrides (ZrN, TiN) are used. A significant stress reduction is observed in the microfuel elements having a carbide layer (SiC, ZrC, NbC, TiC, VC) in that the minimum values of $\sigma_\theta$ are obtained when SiC and ZrC are used. Figure 1 shows the variation of stresses in different layers of a coated microfuel element. All the three PyC layers are under tension (stretched

state), whereas the SiC layer is under compression. Similar dependences were noted earlier [2, 5]. The maximum compressive state (370 MPa) is well below the ultimate strength of SiC. As seen from the calculations, the possible destruction of the PyC layers leads to the redistribution of stresses, which, however, are not dangerous from the standpiont of (bond) failure of the entire coating. This fact is also confirmed by the reactor tests [1].

Thus, the developed method of calculating the stresses in the multilayer coatings of the microfuel elements permits one to take into account the complex effect of the thermal and the radiation loads without restricting the number of the layers to be studied. Besides this, the method takes account of the change in the physicomechanical properties of the materials during the irradiation process.

## LITERATURE CITED


1. A. S. Chernikov, V. S. Kolesov, L. N. Permyakov, et al., "The design and the basic characteristics of the VTGR fuel elements," Vestn. Akad. Nauk BSSR, Ser. Fiz.-Energ. Nauk, No. 3, 77-82 (1982).
2. H. Walter, "On mathematical models for calculating the mechanical behavior of coated fuel particles," Nucl. Eng. Design, 18, 11-39 (1972).
3. J. Kaae, "A mathematical model for calculating stresses in a four-layer carbon–silicon carbide coated fuel particle," J. Nucl. Mater., 32, 322-329 (1969).
4. S. A. Balankin, L. P. Gorbachev, E. G. Grigor'ev, et al., "Mechanical stresses in the shells of the microfuel elements under nonlinear creep law," At. Energ., 45, 205-206 (1978).
5. N. N. Ponomarev-Stepnoi, T. A. Sazykina, and N. I. Tikhonov, "Methods of calculating the stress state of the VTGR microfuel elements and their design criteria," At. Energ., 56, No. 2, 77-81 (1984).


# METHOD FOR THE DETERMINATION OF THE PROCESSES OF PLURAL MUON CATALYSIS

V. G. Zinov, L. N. Somov, and V. V. Fil'chenkov

UDC 539.189.1

A characteristic feature of muon catalysis of the reaction of fusion of hydrogen isotopes is its multiplicity [1, 2]. This makes it possible to contemplate a complete cycle of measurements of constants that determine the kinetics of the process. The kinetics of the catalysis was considered theoretically in [3] in which expressions were derived for the yields and time distributions of the products of synthesis reactions in muon molecules.

For example, the time distribution of acts of catalysis of the reaction*

$$t\mu + t \to tt\mu \to {}^4\mathrm{He} + 2n + \mu \tag{1}$$

has the form

$$dn/dt = \lambda_{tt\mu} \exp\left[-(\lambda_0 + \omega_{tt}\lambda_{tt\mu})\, t\right], \tag{2}$$

and their average multiplicity is

$$\bar{n} = \lambda_{tt\mu}/(\lambda_0 + \omega_{tt}\lambda_{tt\mu}). \tag{3}$$

Expressions (2) and (3) are normalized to the number of muons that induced the reaction. In the derivation of these expressions allowance was made for the fact that the (t + t) nuclear reaction takes place instantaneously, i.e., its rate is $\lambda_{tt}^{t} \gg \lambda_0, \lambda_{tt\mu}$ [4].

*Henceforth we shall use the generally accepted notation: $\lambda_0 = 4.55 \cdot 10^5$ sec$^{-1}$ is the muon decay rate, $\lambda_{tt\mu}$ is the formation rate of ttμ molecules, and $\omega_{tt}$ is the probability of a muon sticking to a helium nucleus in reaction (1).

Translated from Atomnaya Énergiya, Vol. 58, No. 3, pp. 190-192, March, 1985. Original article submitted January 3, 1983.



0038-531X/85/5803-0226$09.50 

Under real experimental conditions the products of muon catalysis reactions are detected with an efficiency $\varepsilon < 1$. It can be shown easily that the time distribution of all (i.e., obtained without the introduction of auxiliary selection criteria) detected catalysis events will have the form

$$dn^{\exp}/dt = \lambda_{tt\mu}\varepsilon \exp[-(\lambda_0 + \omega_{tt}\lambda_{tt\mu})t], \tag{4}$$

and their yield ("experimental multiplicity") is

$$\bar{n}^{\exp} = \varepsilon\lambda_{tt\mu}/(\lambda_0 + \omega_{tt}\lambda_{tt\mu}), \tag{5}$$

i.e., they coincide with "physical" expressions (2) and (3) to within the normalizing factor.

As can be seen from expressions (4) and (5), their use in analysis of the experimental data allows only the products $\omega_{tt}\lambda\lambda_{tt\mu}$ and $\varepsilon\lambda_{tt\mu}$ to be found, i.e., the detection efficiency must be known for the independent determination of $\omega_{tt}$ and $\lambda_{tt\mu}$. Direct determination of $\varepsilon$ is an extremely complex problem. As a rule, in such cases the efficiency is calculated by the Monte Carlo method with allowance for the parameters of the process under study and the geometry of the experimental setup. For reaction (1) such calculations are further complicated by the fact that the neutron energy spectrum is extended in nature. Moreover, the information about the form of the neutron energy distribution from expression (1) is indeterminate because of contradictory information about the contribution of the (nn) and (n$\alpha$) interactions in the final state [5].

It seems obvious that the yield and time distribution of all the neutrons by no means reflect the total information about the process of successive muon catalysis. Additional measurements can be made of the time distribution of the "first," "second," etc., neutrons and their yield or the yield of single, double, etc., neutrons. It turns out that if such additional information is used it becomes unnecessary to have a prior knowledge of $\varepsilon$ (it can be found from the experimental data). In this case in order to determine $\omega_{tt}$ and $\lambda_{tt\mu}$ independently it is sufficient to use only data about the yield and the time distribution of the "first" detected neutrons and about the yield of "second" detected neutrons.

The scheme of the successive muon catalysis of reaction (1) is given in Fig. 1. A muon liberated in reaction (1) forms a t$\mu$ atom "instantaneously" ($\lambda_a \gg \lambda_0, \lambda_{tt\mu}$) and then forms a tt$\mu$ molecule at the rate $\lambda_{tt\mu}$. By $N_i$ we denote the number of t$\mu$ atoms that survive until the i-th fusion reaction event. The functions satisfy the systems of equations

$$dN_1/dt = -\lambda N_1;$$
$$dN_2/dt = -\lambda N_2 + (1-\omega_{tt})\lambda_{tt\mu}N_1;$$

$$dN_i/dt = -\lambda N_i + (1-\omega_{tt})\lambda_{tt\mu}N_{i-1},$$

where $\lambda \equiv \lambda_0 + \lambda_{tt\mu}$.

The solution of this problem for the boundary condition $N_1(0) = 1$ has the form

$$N_i(t) = [(1-\omega_{tt})\lambda_{tt\mu}]^{i-1}t^{i-1}e^{-\lambda t}/(i-1)!$$

Since the reaction (1) proceeds at the rate $\lambda_{tt}^f \gg \lambda_{tt\mu}, \lambda_0$, the time distribution of neutrons from the i-th fusion reaction event is

$$f_i(t) = dn_i/dt = \lambda_{tt\mu}N_i(t) =$$
$$= \lambda_{tt\mu}^i(1-\omega_{tt})^{i-1}t^{i-1}e^{-\lambda t}/(i-1)! \tag{6}$$

The yield of neutrons from the i-th event is

$$n_i = \int_0^\infty f_i(t)\,dt = (1-\omega_{tt})^{i-1}(\lambda_{tt\mu}/\lambda)^i. \tag{7}$$

With the aid of expression (7) we can also get a relation for the yield of single, double, etc., reactions:

$$n(i) = n_i - n_{i-1} = (1-\omega_{tt})^{i-1}\lambda_{tt\mu}^i(\lambda_0 + \omega_{tt}\lambda_{tt\mu})/\lambda^{i+1}. \tag{8}$$

It can be easily shown that the time distribution of all events coincides with expression (2), and the yield of all fusion reaction events

$$\bar{n} = \sum_{i=1}^{\infty} n_i = \int_0^\infty n(t)\,dt = \lambda_{tt\mu}/(\lambda_0 + \omega_{tt}\lambda_{tt\mu})$$

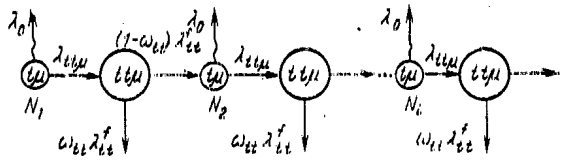

Fig. 1. Scheme of successive moun catalysis of the ttμ fusion reaction.

coincides with expression (3).

Next we take into account the final detection efficiency $\varepsilon < 1$. In this case it becomes possible that the neutron from the i-th catalysis event will be detected first on condition that the neutrons from the preceding $i-1$ reaction events will not be detected. When this is taken into account the time distribution of the first detected neutrons can be represented as a sum

$$f_i^{\exp}(t)=\varepsilon f_1(t)+(1-\varepsilon)\{\varepsilon f_2(t)+(1-\varepsilon)[\varepsilon f_3(t)+\ldots]\}=\varepsilon[f_1(t)+(1-\varepsilon)f_2(t)+(1-\varepsilon)^2 f_3(t)+\ldots]=\varepsilon\sum_{i=1}^{\infty}(1-\varepsilon)^{i-1}f_i(t). \quad (9)$$

On substituting expression (6) for $f_i(t)$ into Eq. (9), we get an explicit formula for this time distribution:

$$f_1^{\exp}(t)=\varepsilon\lambda_{tt\mu}\exp\{-[\lambda_0+(\varepsilon+\omega_{tt}-\varepsilon\omega_{tt})\lambda_{tt\mu}]t\}. \quad (10)$$

The yield of the first detected neutrons is

$$n_1^{\exp}=\int_0^{\infty}f_1^{\exp}(t)\,dt=\varepsilon\lambda_{tt\mu}/[\lambda_0+(\varepsilon+\omega_{tt}-\varepsilon\omega_{tt})\lambda_{tt\mu}]. \quad (11)$$

This expression can be obtained with the aid of formula (9) if in it we replace $f_i(t)$ by $n_i$ in accordance with relation (8).

When deriving an expression for the yield of second detected reaction events, we must take into account the fact that neutrons from the pairs of catalysis events

$$(1,2),(1,3)\ldots(1,i);(2,3),(2,4),\ldots,(2,i);\ldots$$

can be detected. Therefore, the yield is

$$\begin{aligned}n_2^{\exp}&=\varepsilon^2 n_2+\varepsilon^2(1-\varepsilon)n_3+\ldots+\varepsilon^2(1-\varepsilon)^{i-2}n_i+\ldots+\\&+\varepsilon^2(1-\varepsilon)n_3+\ldots=\varepsilon^2[n_2+2(1-\varepsilon)n_3+3(1-\varepsilon)^2 n_4+\\&+\ldots+(i-1)(1-\varepsilon)^{i-2}n_i+\ldots]=\varepsilon^2(1-\omega_{tt})\times\\&\times(\lambda_{tt\mu}/\lambda)^2\sum_{i=2}^{\infty}[(1-\varepsilon)/(1-\omega_{tt})\lambda_{tt\mu}/\lambda]^{i-2}(i-1)=\\&=\varepsilon^2\lambda_{tt\mu}^2(1-\omega_{tt})/[\lambda_0+(\varepsilon+\omega_{tt}-\varepsilon\omega_{tt})\lambda_{tt\mu}]^2.\end{aligned} \quad (12)$$

We note that expression (12) can be derived with the aid of a expression analogous to (8) for i = 1,

$$n_1^{\exp}-n_2^{\exp}=n^{\exp}(1), \quad (13)$$

where $n^{\exp}(1)$ is the yield of singly detected events. In actual fact, the formula for the yield of m events can be written as

$$n^{\exp}(m)=\sum_{i=1}^{\infty}n(i)P_i^m, \quad (14)$$

where $P_i^m$ is the binomial probability of detection of m events out of i events,

$$P_i^m=C_i^m\varepsilon^m(1-\varepsilon)^{i-m}, \quad (15)$$

and $C_i^m$ are the binomial coefficients.

When into formula (14) we substitute for n(i) from (8) and for $P_i^m$ from (15), we get

$$n^{\exp}(m) = \varepsilon^m (1-\omega_{tt})^{m-1} \frac{(\lambda_0+\omega_{tt}\lambda_{tt\mu})\lambda_{tt\mu}^m}{[\lambda_0+(\varepsilon+\omega_{tt}-\varepsilon\omega_{tt})\lambda_{tt\mu}]^{m+1}}. \quad (16)$$

For m = 1 we have

$$n\exp(1) = \frac{\varepsilon\lambda_{tt\mu}(\lambda_0+\omega_{tt}\lambda_{tt\mu})}{[\lambda_0+(\varepsilon+\omega_{tt}-\varepsilon\omega_{tt})\lambda_{tt\mu}]^2}. \quad (17)$$

Substituting expressions (17) and (11) into formula (13), we get Eq. (12) for $n_2^{\exp}$.

Expressions (10)-(12) and (16) are entirely sufficient for use in the analysis of experimental data for the purpose of independently determining $\omega_{tt}$ and $\lambda_{tt\mu}$. It seems most appropriate to use the following algorithm.

1. From analysis of the time distribution (10) of the first detected events we determine

$$a \equiv \lambda_0+(\omega_{tt}+\varepsilon-\varepsilon\omega_{tt})\lambda_{tt\mu}.$$

2. Using the measured values of $a$, $n_1^{\exp}$, and $n_2^{\exp}$ with the aid of the relation $n_1^{\exp}$ $(\lambda_0 + \omega_{tt}\lambda_{tt\mu})/a = n_1^{\exp}(1) = n_1^{\exp} - n_2^{\exp}$, we get

$$b \equiv \lambda_0+\omega_{tt}\lambda_{tt\mu}.$$

3. From the relation

$$1-\omega_{tt} = n_2^{\exp}/(n_1^{\exp})^2$$

we determine $\omega_{tt}$.

4. Substituting this value into the expression for the already known value of $b = \lambda_0 + \omega_{tt}\lambda_{tt\mu}$, we find $\lambda_{tt\mu}$.

Thus, the desired $\omega_{tt}$ and $\lambda_{tt\mu}$ can be found with use of the detection efficiency. Clearly, the efficiency itself can also be obtained on the basis of the analysis carried out and this is of interest in itself. Comparing this value with the corresponding calculations in which different assumptions are made as to the nature of the energy distribution of neutrons from the t + t reaction, we can obtain information about the contribution of (nn) and (nα) interactions in the final state.

It must be pointed out that a necessary condition for the correct determination of $\omega_{tt}$ and $\lambda_{tt\mu}$ in process (1) is that the neutron detection threshold be set properly for each detector; the energy threshold should be below the minimum possible value (from the kinematics of the reaction t + t → $^4$He + 2n) of the total energy of two neutrons.

The expressions (10)-(12) and (16) obtained here can easily be generalized to muon catalysis in pure deuterium. A general comment is that these expressions can be used effectively in the analysis of experimental data only if the experimental multiplicity $\bar{n}^{\exp} \geqslant 1$, i.e., as follows from formula (5), with $\varepsilon\lambda_{tt\mu}/\lambda_0 \geqslant 1$ (the value of $\omega_{tt}$ is small) or for deuterium with $\varepsilon\lambda_{dd\mu}/\lambda_0 \geqslant 1$. For muon catalysis of reaction (1) this condition can be observed for liquid tritium, where $\lambda_{tt\mu} \approx 3\cdot10^6$ sec$^{-1}$ [3], or gaseous tritium at a pressure $P \geqslant 10^4$ kPa.

The authors express their thanks to V. M. Bystritskii and A. D. Konin for useful discussions.

LITERATURE CITED

1. Ya. B. Zel'dovich and S. S. Gershtein, Usp. Fiz. Nauk, 71, 580 (1960); S. S. Gerstein and L. I. Ponomarev, in: Muon Physics, B. Hughes and C. Wu (eds.), Vol. III, New York (1975), p. 141.
2. S. I. Vinitskii, L. I. Ponomarev, I. V. Puzynin, et al., Zh. Eksp. Teor. Fiz., 74, 849 (1978); S. S. Gerstein and L. I. Ponomarev, Phys. Lett., 72B, 80 (1977).
3. S. S. Gershtein, Yu. V. Petrov, L. I. Ponomarev, et al., Zh. Eksp. Teor. Fiz., 78, 2099 (1980).
4. L. I. Ponomarev, in: Proceedings Sixth International Conference on Atomic Physics, Plenum Publ., New York (1978), p. 182.
5. B. Kuhn, A. Kumpf, S. Parzhitsky, and S. Tesh, Nucl. Phys., A183, 640 (1972); R. Larose-Poutisson, and H. Jeremie, Nucl. Phys., A218, 559 (1974).

# NONSTATIONARY MODERATION OF NEUTRONS FROM A POINT PULSED SOURCE IN A SYSTEM OF TWO MEDIA WITH A PLANAR INTERFACE

A. V. Zhemerev

UDC 621.039.512.4

Nonstationary moderation of neutrons in homogeneous and weakly inhomogeneous media has been investigated fairly well [1-4]. During the solution of a number of problems of great scientific and practical interest, it becomes necessary to determine the nonstationary distribution function in inhomogeneous media, in particular in a system of two different media in contact with each other along a planar interface. This problem has not been studied in sufficient detail. Thus, the nonstationary distribution function of neutrons from planar and point sources was investigated in [5] on the assumption that in each medium the mean free path of neutrons is inversely proportional to their velocity. The nonstationary moderation of neutrons with an energy-independent mean free path was considered in [6], but only for a planar source.

In this work on the basis of an age approximation we study the nonstationary distribution function of neutrons from a point pulsed isotropic source in a system consisting of two different media with a planar interface. It is assumed that the neutrons are moderated only as a result of elastic collisions, the neutron mean free path in each medium does not depend on the energy, and no absorption of neutrons occurs.

The Boltzmann kinetic equation for neutrons moderated as a result of elastic collisions with nuclei of the medium in the absence of absorption can be written in the age approximation as [7]

$$\frac{l}{v}\frac{\partial F(u, \mathbf{r}, t)}{\partial t}-\frac{l^2}{3(1-\bar{\mu})}\Delta F(u, \mathbf{r}, t)+\xi\frac{\partial F(u, \mathbf{r}, t)}{\partial u}=S(u, \mathbf{r}, t), \tag{1}$$

where $F(u, \mathbf{r}, t)=vN(u, \mathbf{r}, t)/l$ is the density of neutron collisions; $N(u, \mathbf{r}, t)\,dr\,du$, number of neutrons at the time t in the interval $(\mathbf{r}, \mathbf{r}+d\mathbf{r}; u, u+du)$; $u=\ln(E_0/E)$, lethargy; E, energy of the moderated neutrons; $E_0$, maximum energy of the neutrons of the source; v, neutron velocity; $l$, neutron mean free path up to elastic collision; $\xi$, average change in the lethargy as a result of a separate elastic collision; $\mu$, mean cosine of the angle of elastic scattering of neutrons in the laboratory coordinate system; and $S(u, \mathbf{r}, t)$, a function that characterizes the space-energy and time distributions of the neutron sources. For a point isotropic monoenergetic instantaneous source of neutrons we have

$$S(u, \mathbf{r}, t)=\delta(\mathbf{r})\,\delta(u)\,\delta(t). \tag{2}$$

Suppose that neutron moderation occurs in a system of two different media with the plane $z = 0$ as their interface and the neutron source (2) is on the z axis, perpendicular to the interface of the two media. Then Eq. (1) in a cylindrical coordinate system can be written as

$$e^{\frac{u}{2}}\frac{l_2}{v_0}\frac{\partial F_2}{\partial t}-\frac{l_2^2}{3(1-\bar{\mu}_2)}\left\{\frac{\partial^2 F_2}{\partial z^2}+\frac{1}{\rho}\frac{\partial}{\partial \rho}\left(\rho\frac{\partial F_2}{\partial \rho}\right)\right\}+\xi_2\frac{\partial F_2}{\partial u}=\frac{\delta(\rho)}{2\pi\rho}\delta(z-z_0)\,\delta(u)\,\delta(t), \quad z>0; \tag{3}$$

$$e^{\frac{u}{2}}\frac{l_1}{v_0}\frac{\partial F_1}{\partial t}-\frac{l_1^2}{3(1-\bar{\mu}_1)}\left\{\frac{\partial^2 F_1}{\partial z^2}+\frac{1}{\rho}\frac{\partial}{\partial \rho}\left(\rho\frac{\partial F_1}{\partial \rho}\right)\right\}+\xi_1\frac{\partial F_1}{\partial u}=0, \quad z<0, \tag{4}$$

where $v_0$ is the initial neutron velocity. In writing Eqs. (3) and (4) we assume that the first medium with the higher moderating power is at $z < 0$ while the neutron source is in the other medium or on the interface ($z_0 \geqslant 0$).

The solution of Eqs. (3) and (4) should be determined from the conditions of boundedness at infinity

Translated from Atomnaya Énergiya, Vol. 58, No. 3, pp. 192-194, March, 1985. Original article submitted October 1, 1984.

 0038-531X/85/5803-0230$09.50 

$$F_1(u, z, \rho, t) \to 0 \quad \text{for} \quad z \to -\infty;$$
$$F_2(u, z, \rho, t) \to 0 \quad \text{for} \quad z \to \infty; \tag{5}$$
$$F_{1,2}(u, z, \rho, t) \to 0 \quad \text{for} \quad \rho \to \infty;$$

as well as from the conditions of continuity of the neutron flux and current across the interface [7]

$$l_1 F_1 = l_2 F_2; \quad \frac{l_1^2}{1-\bar{\mu}_1}\frac{\partial F_1}{\partial z} = \frac{l_2^2}{1-\bar{\mu}_2}\frac{\partial F_2}{\partial z} \quad \text{for} \quad z = 0. \tag{6}$$

Making a change of variables,

$$t' = \frac{\xi_2 v_0 t}{l_2}; \quad z' = \frac{\sqrt{3(1-\bar{\mu}_2)\xi_2}}{l_2} z;$$
$$\rho' = \frac{\sqrt{3(1-\bar{\mu}_2)\xi_2}}{l_2} \rho; \tag{7}$$

$$\tau = 2\left(e^{\frac{u}{2}} - 1\right) - t', \tag{8}$$

Eqs. (3) and (4) can be represented in the following form (henceforth we omit the primes in t', z, ρ'),

$$-\frac{\partial^2 F_2}{\partial z^2} - \frac{1}{\rho}\frac{\partial}{\partial \rho}\left(\rho \frac{\partial F_2}{\partial \rho}\right) + \frac{\partial F_2}{\partial u} = s_i \frac{\delta(\rho)}{\rho}\delta(z - z_0)\delta(u)\delta(\tau), \quad z > 0; \tag{9}$$

$$(1-ab)\, e^{\frac{u}{2}} \frac{\partial F_1}{\partial \tau} - g^2 \frac{\partial^2 F_1}{\partial z^2} - \frac{g^2}{\rho}\frac{\partial}{\partial \rho}\left(\rho \frac{\partial F_1}{\partial \rho}\right) + \frac{\partial F_1}{\partial u} = 0, \qquad z < 0, \tag{10}$$

where

$$a = l_1/l_2; \quad b = \xi_2/\xi_1; \quad g^2 = a^2 b(1-\bar{\mu}_2)/(1-\bar{\mu}_1);$$
$$s_i = \frac{v_0}{2\pi l_2}\left[\frac{\sqrt{3(1-\bar{\mu}_2)\xi_2}}{l_2}\right]^3$$

We write the boundary conditions (6) in the form

$$aF_1 = F_2; \tag{11}$$

$$\frac{g^2}{b}\frac{\partial F_1}{\partial z} = \frac{\partial F_2}{\partial z}. \tag{12}$$

Using the Laplace transformation in the variable τ and the Bessel transformation in the variable ρ

$$F_{1,2}(u, z, \lambda, p) = \int_0^\infty d\rho \rho J_0(\lambda\rho) F_{1,2}(u, z, \rho, \tau),$$

we can write Eqs. (9) and (10) in the form

$$-\frac{\partial^2 F_2}{\partial z^2} + \lambda^2 F_2 + \frac{\partial F_2}{\partial u} = s_i \delta(z - z_0)\delta(u), \quad z > 0; \tag{13}$$

$$(1-ab)\, e^{\frac{u}{2}} pF_1 - g^2 \frac{\partial^2 F_1}{\partial z^2} + g^2\lambda^2 F_1 + \frac{\partial F_1}{\partial u} = 0, \quad z < 0. \tag{14}$$

The boundary conditions (9 and (10) remain unchanged.

The solution of Eq. (13) that satisfies the condition (5) can be written as the sum of two functions [8],

$$F_2(u, z, \lambda, p) = F_h(u, z, \lambda, p) + F(u, z, \lambda, p), \tag{15}$$

where the first function

$$F_h(u, z, \lambda, p) = \frac{s_i e^{-\lambda^2 u}}{2\sqrt{\pi u}}\left\{\exp\left[-\frac{(z-z_0)^2}{4u}\right] - \exp\left[-\frac{(z+z_0)^2}{4u}\right]\right\} \tag{16}$$

describes neutrons that are moderated only in the second medium, while the second function

$$F(u, z, \lambda, p) = \int_0^u \frac{\varphi(t, \lambda, p) \exp\left[-\lambda^2 (u-t) - \frac{z^2}{4(u-t)}\right]}{\sqrt{\pi (u-t)}} dt \qquad (17)$$

is the distribution function of neutrons that have been in the first medium at least once. In formula (17) the function $\varphi$ (u, $\lambda$, p) is a function that determines the boundary condition for the function F (u, z, $\lambda$, p) for z = 0:

$$\frac{\partial F(u, z, \lambda, p)}{\partial z} = -\varphi(u, \lambda, p). \qquad (18)$$

Applying the inverse Laplace and Bessel transformations [9] to formula (16), we get

$$F_h(u, z, \rho, \tau) = \frac{s_i \exp\left(-\frac{\rho^2}{4u}\right)}{4\sqrt{\pi u^3}} \left\{\exp\left[-\frac{(z-z_0)^2}{4u}\right] - \exp\left[-\frac{(z+z_0)^2}{4u}\right]\right\} \delta(\tau). \qquad (19)$$

According to formulas (8) and (19), in the case of neutrons that are moderated only in the second medium the moderation time is uniquely related to the lethargy by

$$t_h = 2\left(e^{\frac{u}{2}} - 1\right), \qquad (20)$$

which is a consequence of the age approximation [1].

The solution of Eq. (14) with the boundary condition for z = 0

$$\frac{\partial F_1}{\partial z} = -\frac{b}{g^2}\left[\varphi(u) - \frac{s_i z_0}{2\sqrt{\pi u^3}} \exp\left(-\lambda^2 u - \frac{z_0^2}{4u}\right)\right], \qquad (21)$$

obtained upon substitution of formula (15) into condition (12), becomes

$$F_1(u, z, \lambda, p) = \frac{bz_0}{2\pi g} \int_0^u \frac{\exp\left\{-\lambda^2 g^2 (u-t) - 2p(1-ab)\left(e^{\frac{u}{2}} - e^{\frac{t}{2}}\right) - \lambda^2 t - \frac{z_0^2}{4t} - \frac{z^2}{4g^2(u-t)}\right\}}{\sqrt{(u-t)\, t^3}} dt -$$

$$-\frac{b}{g_0} \int_0^u \frac{\exp\left\{-\lambda^2 g^2 (u-t) - 2p(1-ab)\left(e^{\frac{u}{2}} - e^{\frac{t}{2}}\right) - \frac{z^2}{4g^2(u-t)}\right\}}{\sqrt{\pi (u-t)}} \varphi(t)\, dt. \qquad (22)$$

Using condition (11), we obtain an integral equation for finding the function $\varphi$(u, $\lambda$, p)

$$\int_0^u \frac{\varphi(t)\, e^{-\lambda^2 (u-t)}}{\sqrt{\pi (u-t)}} dt + \alpha \int_0^u \frac{\exp\left\{-\lambda^2 g^2 (u-t) - 2p(1-ab)\left(e^{\frac{u}{2}} - e^{\frac{t}{2}}\right)\right\} \varphi(t)}{\sqrt{\pi (u-t)}} dt =$$

$$= \frac{\alpha z_0}{2\pi} \int_0^u \frac{\exp\left\{-\lambda^2 g^2 (u-t) - 2p(1-ab)\left(e^{\frac{u}{2}} - e^{\frac{t}{2}}\right) - \lambda^2 t - \frac{z_0^2}{4t}\right\}}{\sqrt{(u-t)\, t^3}} dt, \qquad (23)$$

where $\alpha = ab/g = \frac{\xi_2}{\xi_1}\sqrt{\frac{1-\bar{\mu}_1}{1-\bar{\mu}_2}}$.

Thus, the problem of determining the nonstationary distribution function of neutrons moderated in a system of two media reduces in space to the solution of the integral equation (23) at the interface for z = 0.

We look for the solution of Eq. (23) for the case when the moderating properties of the two media differ markedly ($g \ll 1$). In this case the term $g^2\lambda^2 F_1$ in Eq. (14) can be neglected and $\alpha$ can be assumed to be zero. This means that a stationary one-dimensional (in the variable z) solution can be used in the first medium. This approximation was substantiated in [5] for media with markedly different moderating properties. Equation (23) then takes on the form (g = 0, $\alpha$ = 0)

$$\int_0^u \frac{\varphi(t)\, e^{-\lambda^2 (u-t)}}{\sqrt{\pi (u-t)}} dt + \alpha \int_0^u \frac{\varphi(t) \exp\left[-2p\left(e^{\frac{u}{2}} - e^{\frac{t}{2}}\right)\right]}{\sqrt{\pi (u-t)}} dt = \frac{\alpha z_0}{2\pi} \int_0^u \frac{\exp\left[-2p\left(e^{\frac{u}{2}} - e^{\frac{t}{2}}\right) - \lambda^2 t - \frac{z_0^2}{4t}\right]}{\sqrt{(u-t)\, t^3}} dt. \qquad (24)$$

The solution of the integral equation (24) will be sought in the form of power series in p,

$$\varphi(u, \lambda, p) = \sum_{n=0}^{\infty} \frac{(-1)^n}{n!} p^n \varphi_n(u, \lambda). \tag{25}$$

We note that the functions $\varphi_n(u, \lambda)$ determine the "time" moments of the neutron distribution function [5, 6]:

$$\varphi_n(u, \lambda) = \int_0^{\infty} d\tau \tau^n \varphi(u, \lambda, \tau). \tag{26}$$

Substituting the expansions

$$\exp[-2p(e^{\frac{u}{2}} - e^{\frac{t}{2}})] = \sum_{n=0}^{\infty} \frac{(-1)^n}{n!} p^n [2(e^{\frac{u}{2}} - e^{\frac{t}{2}})]^n;$$

$$\varphi(t) \exp[-2p(e^{\frac{u}{2}} - e^{\frac{t}{2}})] = \sum_{n=0}^{\infty} \frac{(-1)^n}{n!} p^n \sum_{k=0}^{n} C_n^k \varphi_k(t) [2(e^{\frac{u}{2}} - e^{\frac{t}{2}})]^{n-k}$$

and Eq. (25) into (24) and equating the terms for the same power of n, we obtain the following system of integral equations to determine the functions $\varphi_n(u, \lambda)$:

$$\int_0^u \frac{\varphi_n(t) e^{-\lambda^2(u-t)}}{\sqrt{\pi(u-t)}} dt + \alpha \sum_{k=0}^{n} C_n^k \int_0^u \frac{\varphi_k(t) [2(e^{\frac{u}{2}} - e^{\frac{t}{2}})]^{n-k}}{\sqrt{\pi(u-t)}} dt =$$

$$= \frac{\alpha z_0}{2\pi} \int_0^u \frac{\exp\left(-\lambda^2 t - \frac{z_0^2}{4t}\right) [2(e^{\frac{u}{2}} - e^{\frac{t}{2}})]^n}{\sqrt{(u-t) t^3}} dt. \tag{27}$$

When we substitute the expansion

$$(e^{\frac{u}{2}} - e^{\frac{t}{2}})^{n-k} = e^{\frac{n-k}{2} u} \sum_{i=0}^{n-k} C_{n-k}^i (-1)^i e^{-\frac{i}{2}(u-t)}$$

into Eq. (27) and perform the Laplace transformation in the lethargy

$$\varphi_n(s, \lambda) = \int_0^{\infty} du e^{-su} \varphi_n(u, \lambda)$$

we get the following formula for the functions $\varphi_n(u, \lambda)$:

$$\varphi_n(s, \lambda) = \frac{\sqrt{s}\sqrt{s+\lambda^2}}{\sqrt{s}+\alpha\sqrt{s+\lambda^2}} \left[ F_n(s, \lambda) - \alpha \sum_{k=0}^{n-1} \sum_{i=0}^{n-k} C_n^k C_{n-k}^i (-1)^i 2^{n-k} \frac{\varphi_k\left(s - \frac{n-k}{2}, \lambda\right)}{\sqrt{s - \frac{n-k-i}{2}}} \right], \tag{28}$$

where $F_n(s, \lambda)$ is the Laplace transform of the right-hand side of Eq. (27):

$$F_n(s, \lambda) = \alpha 2^n \sum_{i=0}^{n} C_n^i (-1)^i \exp\left(-z_0 \sqrt{s+\lambda^2 - \frac{n}{2}}\right) \Big/ \sqrt{s + \frac{i}{2} - \frac{n}{2}}. \tag{29}$$

We point out that if we assume that $\lambda = 0$ in formulas (15), (22), (28), and (29), we get the solution for a planar source.

The author thanks V. V. Metelkin for useful discussions.

LITERATURE CITED

1. M. V. Kazarnovskii, "Theory of nonstationary elastic moderation of neutrons in a heavy medium," Trudy FIAN, 11, 176 (1959).

2. M. V. Kazarnovskii, in: Theoretical and Experimental Problems of Nonstationary Neutron Transport [in Russian], Atomizdat, Moscow (1972), pp. 10-45.
3. E. V. Metelkin and G. Ya. Trukhanov, At. Energ., 37, No. 6, 466 (1974).
4. E. V. Metelkin, At. Energ., 40, No. 1, 45 (1976).
5. A. V. Zhemerev, M. V. Kazarnovskii, Yu. A. Medvedev, and E. V. Metelkin, At. Energ., 50, No. 1, 29 (1981).
6. Yu. A. Medvedev and E. V. Metelkin, At. Energ., 48, No. 5, 308 (1980).
7. A. Weinberg and E. Wigner, Physical Theory of Neutron Chain Reactors, Univ. of Chicago Press, Chicago (1958).
8. B. M. Budak, A. A. Samarskii, and A. N. Tikhonov, Problems in Mathematical Physics [in Russian], Nauka, Moscow (1972).
9. G. Bateman and A. Erdélyi, Tables of Integral Transforms, McGraw-Hill.

# CONDUCTIVITY OF AN ELECTRICAL CERAMIC DURING REACTOR IRRADIATION

É. G. Ashirov, Kim Gen Chan,
N. S. Kostyukov, M. I. Muminov,
V. N. Sandalov, and Yu. S. Skripnikov

UDC 621.315.61:620.193.6

The studies on the variation of electrical conductivity of the industrial types of electrical ceramics during the reactor irradiation process [1-3] gave a basis to the postulate that the γ-component of the reactor irradiation determines the radiation-stimulated electrical conductivity during the initial stages, and that the effect of the neutron component starts after attaining a neutron fluence sufficient to cause structural damage that is quantitatively comparable to the number of preradiation defects. However, the role of the glass and the crystalline phases of the ceramic on the mechanism of electrical conducivity during reactor irradiation has not been studied. In view of this, in the range 60-700°C we measured the temperature dependence of the specific bulk electrical conductivity of the industrial ceramics MK, GB-7, and UF-46 having a crystalline phase of corundum and of the ceramics UF-46 and GB-7 containing a glass phase under the action of the $^{60}$Co γ radiation and the radiation from the active zone (core) of a VVR-SM reactor. Figure 1 shows the results obtained on the UF-46 ceramic. The trend is characteristic of the other experimental materials also. There are two distinct regions on the curves: the first one is a low-temperature region where the electrical conductivity is a slowly varying function of temperature, and the second one is a high-temperature region where the temperature dependence is significant and has an exponential character. During γ irradiation, in the first region the electrical conductivity increases in proportion to the absorbed-dose intensity ($P_\gamma$), and in the second region it is determined by the thermally activated conductivity which is ionic

TABLE 1. Values of the Coefficient Δ and the Material Characteristics

| Material | Content of crystalline phase, % | Total surface of the crystalline phase in 1 cm$^3$, cm$^2$ | Δ |
|---|---|---|---|
| Sapphire | 100 | — | 0,97 |
| MK | 99 | 14,5 | 0,74 |
| GB-7 | 92 | 7,4 | 0,91 |
| UF-46 | 70 | 18 | 0,74 |
| Glass phase of UF-46 | 0 | — | 0,48 |
| Glass phase of GB-7 | 0 | — | 0,59 |

Translated from Atomnaya Énergiya, Vol. 58, No. 3, pp. 195-196, March, 1985. Original article submitted February 22, 1984.

 0038-531X/85/5803-0234$09.50 

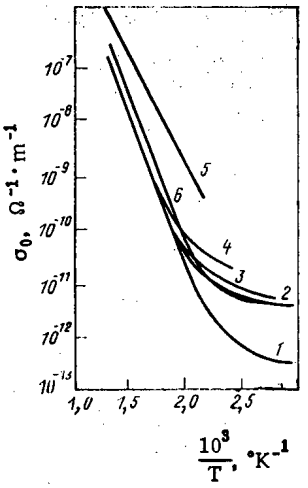


Fig. 1

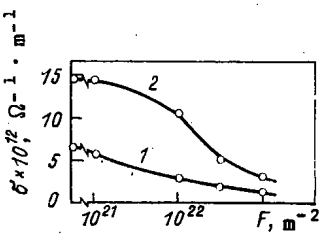


Fig. 2

Fig. 1. Temperature dependence of the electrial conductivity of ceramic UF-46 during reactor irradiation: 1) before irradiation; 2) $P_\gamma$ = 5.7 Gy/sec; 3) $P_\gamma$ = 10 Gy/sec; 4) $P_\gamma$ = 30 Gy/sec; 5) $\Phi = 2\cdot10^{16}$ m$^{-2}\cdot$sec$^{-1}$; 6) in the γ-radiation field of the stalled reactor.

Fig. 2. Effect of prior neutron irradiation on the electrical conductivity of UF-46 (1) and GB-7 (2).

TABLE 2. Values of u before and after Reactor Irradiation, eV

| Material | Before irradiation | At a neutron flux density $\varphi = 3\cdot10^{16}$ m$^{-2}\cdot$sec$^{-1}$ | Content of glass phase, % |
|---|---|---|---|
| UF-46 | 1,1 | 0,7 | 30 |
| GB-7 | 1,13 | 0,9 | 9 |
| MK | 1,2 | 1,1 | 1 |
| Glass phase of UF-46 | 2,4 | 1,2 | 100 |
| Glass phase of GB-7 | 1,7 | 1,25 | 100 |

TABLE 3. Change in the Coefficient Δ after Reactor Irradiation of the Ceramics

| Material | Before irradiation | After irradiation | Rel. change | Content of crystalline phase, % |
|---|---|---|---|---|
| MK | 0,74 | 0,59 | —0,20 | 99 |
| GB-7 | 0,91 | 0,69 | —0,24 | 92 |
| UF-46 | 0,74 | 0,64 | —0,10 | 74 |
| Glass phase of GB-7 | 0,59 | 0,60 | — | — |
| Glass phase of UF-46 | 0,48 | 0,64 | +0,24 | — |

in nature [4]. With increasing γ-radiation intensity, the boundary between these regions is shifted toward higher temperatures.

At a temperature of 70°C and in the range 0.18-50 Gy/sec, the electrical conductivity of all the experimental materials can be described by the Fowler–Rose model [5] and varies according to the following law:

$$\sigma = \sigma_0 P_\gamma$$

where $\sigma_0$ is a constant that does not depend on $P_\gamma$; and $\Delta$ is a coefficient that depends on the material (Table 1).*

It is seen from Table 1 that the magnitude of $\Delta$, characterizing the radiation sensitivity, is determined by the content of the crystalline phase in the ceramic. Based on the data obtained on the MK and GB-7 ceramics, it can be concluded that the dispersion of the crystalline phase affects the $\gamma$-stimulated electrical conductivity. The magnitudes of $\Delta$ and the radiation-induced electrical conductivity increase with increasing crystalline-phase content and decreasing dispersion.

During reactor irradiation, as in the case of $\gamma$ irradiation, in the low-temperature region the electrical conductivity is a slowly varying function of temperature, and apparently, it is mainly determined by the $\gamma$-component of the radiation acting on the crystalline phase. During reactor irradiation, in the high-temperature region the electrical conductivity is higher than that obtained under $\gamma$ irradiation at comparable absorbed dose intensities. The temperature dependence is given by the equation

$$\sigma_p = \sigma_1 \exp\left(-\frac{u}{kT}\right),$$

where $\sigma_p$ is the electrical conductivity during reactor irradiation; $\sigma_1$, a temperature-independent constant; k, Boltzmann constant; T, absolute temperature; and u, activation energy of the migration conductivity. The obtained values of u are seen to be smaller than those obtained during the out-of-reactor measurements and during $\gamma$ irradiation. This reduction in the activation energy can be correlated with the glass-phase content in the ceramic (Table 2).

We may assume that during reactor irradiation, the conductivity in the low-temperature region is due to the generated electron–hole pairs, whereas in the high-temperature region it is ionic in nature just as the conductivity of the glass phase. The reduction in the activation energy is probably related to the instantaneous action of the neutron component of the reactor radiation.

While the activation energy changes during the $^{60}$Co $\gamma$ irradiation process, under the reactor radiation (at comparable values of $P_\gamma$ = 50 Gy/sec) it decreases (see Fig. 1, curve 5), and after stopping the reactor it is restored to its previous value (see Fig. 1, curve 6).

As a rule, the ionic conductivity of glasses and ceramics is due to the presence of weakly bonded Na and K ions [4]. However, according to the results of electrolysis, in the UF ceramic the concentration of electrically active ions is only $7 \cdot 10^{24}$ m$^{-3}$ [6] at a total sodium-ion concentration of $2.7 \cdot 10^{26}$ m$^{-3}$. It is probable that the action of neutrons converts an additional number of ions into the electrically active state. Besides this, during the reactor-irradiation process at a temperaure corresponding to the upper limit of the low-temperature region, we observed an abnormally large increase of the permittivity in the frequency range 0.3-30 kHz. This is related to an increase in the number of the Frenkel' pairs which can make the migration of ions easy and can thereby increase the electrical conductivity.

After irradiating up to a neutron fluence of $10^{23}$ m$^{-2}$, the temperature dependences of the electrical conductivity of the experimental materials do not virtually change, but in some cases we observed an insignificant increase in the electrical conductivity in the low-temperature region. However, this effect quickly disappears after annealing at 300°C. These facts permit one to conclude that the number of defects formed during the irradiation process does not exceed the number of defects existing before irradiation. The crystalline phase of the ceramic must be particularly sensitive to the action of neutrons owing to its less defective structure.

In the $^{60}$Co $\gamma$-radiation field with an absorbed-dose intensity of 22 Gy/sec, we measured the electrical conductivity of the UF-46 and GB-7 ceramics which were previously subjected to neutron irradiation (Fig. 2). It was estabished that the electrical conductivity of the ceramics in the $\gamma$-radiation field decreases with increasing neutron fluence. A similar reduction in the electrical conductivity during the reactor-irradiation process was also noted earlier [2]. Table 3 gives the measured values of the coefficient $\Delta$ for the neutron-irradiated ceramics up to a fluence of $10^{23}$ m$^{-2}$.

*Obviously, this equation is incomplete in Russian original – Publisher.

An analysis of the obtained results gives the following picture with regard to the behavior of the reactor-irradiated ceramics. In the low-temperature region, the radiation-induced conductivity is due mainly to electron–hole pairs that form under the influence of the γ-component of the reactor radiation, and is determined by the content and the dispersion of the crystalline phase. In the high-temperature region there is no effect of the γ-component. During irradiation with a fast neutron flux, the ionic component of conductivity (determined by the content of glass phase in the ceramic) increases, and the activation energy decreases. In the high-temperature region, an increase in the neutron fluence up to $10^{22}$ $m^{-2}$ does not bring about changes in the temperature dependence of the electrical conductivity.

## LITERATURE CITED


1. N. S. Kostyukov, N. P. Antonova, M. I. Zil'berman, and N. A. Aseev, Behavior of Irradiated Electrical Materials [in Russian], Atomizdat, Moscow (1979).
2. N. A. Aseev, B. V. Samsonov, and V. A. Tsykanov, "A study of the conductivity of porcelain during irradiation in a high-flux reactor," Preprint NIIAR 17-125, Melekes (1971).
3. N. S. Kostyukov, V. V. Maslov, and M. I. Muminov, Radiation Stability of Dielectrics [in Russian], Tashkent Branch, Academy of Sciences of the USSR (1981).
4. V. I. Dmitriev, "A study of the nature of conductivity and the aging of some electrical ceramics and glasses over a wide temperature range," Ph.D. Thesis (Physical and Mathematical Sciences), V. I. Lenin VÉI (1968).
5. Rose, Fundamentals of the Theory of Photoconductivity [Russian translation], Mir, Moscow (1966).
6. É. G. Ashirov, L. N. Zyuz', M. I. Muminov, and Yu. S. Skripnikov, "Electrical aging and the nature of conductivity of the electrical ceramic M-23," Izv. Akad. Nauk Uzb. SSR, Ser. Fiz.-Mat. Nauk, No. 1, 52-55 (1983).


# USE OF WEIGHTED LINEAR REGRESSION MODEL TO IDENTIFY TOTAL-ABSORPTION PEAKS DURING PROCESSING OF COMPLEX γ-RAY SPECTRA

V. Badulin and T. Petkov*

UDC 535.33.001.57

Two problems are encountered in the general case during the identification of total-absorption peaks in complex γ-ray spectra (even when computers are employed):

1) the error in the determination of the energy of γ radiation correspnding to a single peak is such that the tabulated values of the energy of several γ-emitters fall within the chosen confidence interval;

2) the spectrum contains multiplet peaks which cannot be separated into the constituent components, either in principle or by virtue of the limited capabilties of the computational program used in the mathematical processing of the spectrum.

Usually a priori and/or posterior information about the composition of the γ-source is used in one way or other during the solution of these problems. The capabilities of this method are limited and the formal description in the form of an algorithm is fairly involved. The method does not, in the general case, make it possible to process all the total-absorption peaks present in the spectrum: the radionuclides in the source are identified and their content is estimated on the basis of reference peaks, the number of which is limited (often to one or two) [1-4]. This limitation on the use of the information contained in the spectrum leads to an increase in the random errors in the results from the processing of the spectrum and/or the appearance of systematic errors.

The information contained in the γ-ray spectrum can be extracted more completely when the generalized model of weighted linear regression is used to process it. The gist of the method is as follows. Each total-absorption peak satisfies the equality

*Scientific Institute of Roentgenology and Radiobiology, Sofia, Bulgaria.

Translated from Atomnaya Énergiya, Vol. 58, No. 3, pp. 196-197, March, 1985. Original article submitted April 27, 1984.

0038-531X/85/5803-0237$09.50  

$$A=\sum_{i}^{n} c_i X_i + e, \tag{1}$$

where A is the area of the peak [in pulses ($A \geqslant 0$)], $X_i$ is the activity of the i-th nuclide [in becquerels ($X_i \geqslant 0$)], $c_i$ are normalization factors [in pulses/becquerel], n is the number of nuclides whose γ radiation is recorded in the particular peak ($n \geqslant 1$), and e is a random quantity with zero average and final variance. For m peaks of the spectrum we have the system of equations

$$A_j=\sum_{i}^{N} c_{ij} X_i + e_j, \tag{2}$$

where N is the possible number of nuclides in the source; the random quantities $e_j$ are independent and their variances are different.

For $m > N$ the system of equations (2) meets all the conditions of the heteroscedastic model of linear regression [5]. In order to solve it by the method of least squares it is necessary to go on to a model with equal variance, making allowance for the difference in the variances of the random quantities $e_j$ with the aid of weighting coefficients:

$$\mathrm{Var}\,(e_j)=g_j^2 \cdot \mathrm{const}, \tag{3}$$

where const is an unknown constant and $g_j$ are known weights.

We consider the quantities

$$B_j=A_j/g_j, \quad d_{ij}=c_{ij}/g_j, \quad f_j=e_j/g_j;$$

which satisfy the equations

$$B_j=\sum_{i}^{N} d_{ij} X_i + f_j. \tag{4}$$

Since $f_j$ are random quantities with zero average variance and identical final variance, the system of equations (4) satisfies the conditions of the linear regression model [5]. An estimate of the weighted least squares of the parameters $X_i$ is provided by the solutions of the corresponding matrix equation

$$B=D\bar{X}, \tag{5}$$

which is an unbiased estimate with a uniformly minimum variance [5],

$$\bar{X}=[D'D]^{-1}D'B; \tag{6}$$

$$\mathrm{Cov}\,(\bar{X}_i, \bar{X}_j)=\frac{1}{m-N}\sum_{j}^{m}\left(B_j-\sum_{j}^{N} d_{ij}\bar{X}_i\right)[D'D]^{-1}, \tag{7}$$

where D' is the transpose of the matrix D. The elements of the matrix $\bar{X}$ constitute an estimate of the sought activity of the γ-ray emitters, and the diagonal elements of the matrix $\mathrm{Cov}(\bar{X}_i, \bar{X}_j)$ constitute an estimate of the variances of those estimates.

The weighted linear regression model for the processing of γ-ray spectra is used in accordance with the following algorithm.

1. Search for the total-absorption peaks. Determination of the main parameters of each peak (area corresponding to the γ-radiation energy, resolution) and the statistical errors of these parameters.

2. Identification of the radionuclides whose tabulated value of γ-ray energy falls within the preselected confidence interval around the detected peaks.

3. Selection of the tabulated values of the energy of all γ-ray quanta of the chosen nuclides.

4. Isolation of those parts of the spectrum outside the peaks in which the γ radiation of the chosen nuclides can be detected. Estimation of the areas of the presumed peaks and the errors of their determination.

5. Writing of the system of equations (2) for all real and presumed total-absorption peaks.

6. Choice of the weighting coefficients $g_j$ (e.g., $g_j = \mathrm{Var}(A_j)^{0.5}$). Writing of Eq. (5).

7. Solution of Eq. (5). Selection of the elements of the matrix $\bar{X}$ for which $\bar{X}_i > 0$ with the preselected confidence interval. Writing of the results.

The algorithm for the processing of a γ-ray spectrum can be executed as a program for computers, including minicomputers (with a reasonable restriction of the library of γ-ray emitter characteristics) with a 32-64K memory, e.g., for a programmable computerized multichannel pulse-height analyzer.

## LITERATURE CITED


1. A. Ya. Anikin et al., in: Applied Nuclear Spectroscopy [in Russian], No. 9, Atomizdat, Moscow (1979), p. 239.
2. L. N. Moskvin et al., At. Energ., 52, No. 1, 14 (1982).
3. V. I. Vinogradov, L. V. Stepanov, and V. I. Protasov, At. Energ., 52, No. 5, 338 (1982).
4. V. V. Filippov et al., in: Atomic Power Plants [in Russian], No. 5, Énergoatomizdat, Moscow (1983).
5. P. Bickel and K. Doxam, Mathematical Statistics [Russian translation], Nos. 1, 2, Finansy i Statistika, Moscow (1983).


# NEUTRON ABSORPTION CROSS SECTION OF $^{239}$Pu IN THE REGION OF RESOLVED RESONANCES

V. V. Kolesov and A. A. Luk'yanov

UDC 539.170.013

The complex energy structure of the $^{239}$Pu neutron cross sections in the region of resolved resonances is related to the important role of interresonance interference in shaping this structure (Fig. 1). Therefore, in the parametrization of the energy dependence of the cross sections in regions containing several resonance levels, various multilevel schemes are widely used to take correct account of the main characteristic features of the resonance structure and the interference of resonance states [1].

Good results in the parametrization of the cross sections were obtained in the region of resolved resonances by using S-matrix formulas [2] in which the energy dependence of the elements of the collision matrix $U^J(E)$ is described by the sum over the resonances m (J) with a definite value of the totl angular momentum J:

$$U^J_{nc}(E) = e^{-i\varphi_{nJ}}\left(\delta_{nc} + i\sum_{m(J)}\frac{\sqrt{\Gamma_{mn}\Gamma_{mc}}}{E_m - E}\right)e^{-i\varphi_{cJ}}, \quad (1)$$

where the $\varphi_{nJ}$ ($\varphi_{cJ}$) are the phases of the potential scattering in the channel n (c); $\Gamma_{mn} = \Gamma^0_{mn}\sqrt{E}$ and $\Gamma_{mc}$ are the resonance widths in the channel n (c), which are generally complex; and $E_m = \mu_m - i\nu_m$ is the characteristic energy of the resonance states [1].

The total cross section $\sigma_t(E)$ in the S-matrix formalism is written as the sum of Breit-Wigner terms [1, 2]:

$$\sigma_t(E) = 2\pi\lambda^2\sum_J g(J)\left[1 - \mathrm{Re}\,U^J_{nn}(E)\right] = \sigma_p + \frac{\pi}{k^2}\sqrt{E}\sum_J\sum_{m(J)}\frac{G_m\nu_m + H_m(\mu_m - E)}{(\mu_m - E)^2 + \nu_m^2}, \quad (2)$$

where

$$G_m + iH_m = 2g(J)\,\Gamma^0_{mn}e^{-2i\varphi_{nJ}}; \quad (3)$$

$\sigma_p = 4\pi\lambda^2\sum_J g(J)\sin^2\varphi_{nJ}$ is the cross section for potential scattering.

By using (2) to analyze data on the resonance structure of the total cross section, obtained with good resolution [3], we obtained a set of resonance parameters $\mu_m$, $\nu_m$, $G_m$, and $H_m$ for the whole region of resolved resonances of $^{239}$Pu up to energies $\leqslant 500$ eV [4]. Figure

Translated from Atomnaya Énergiya, Vol. 58, No. 3, pp. 197-198, March, 1985. Original article submitted August 23, 1984.

0038-531X/85/5803-0239$09.50  

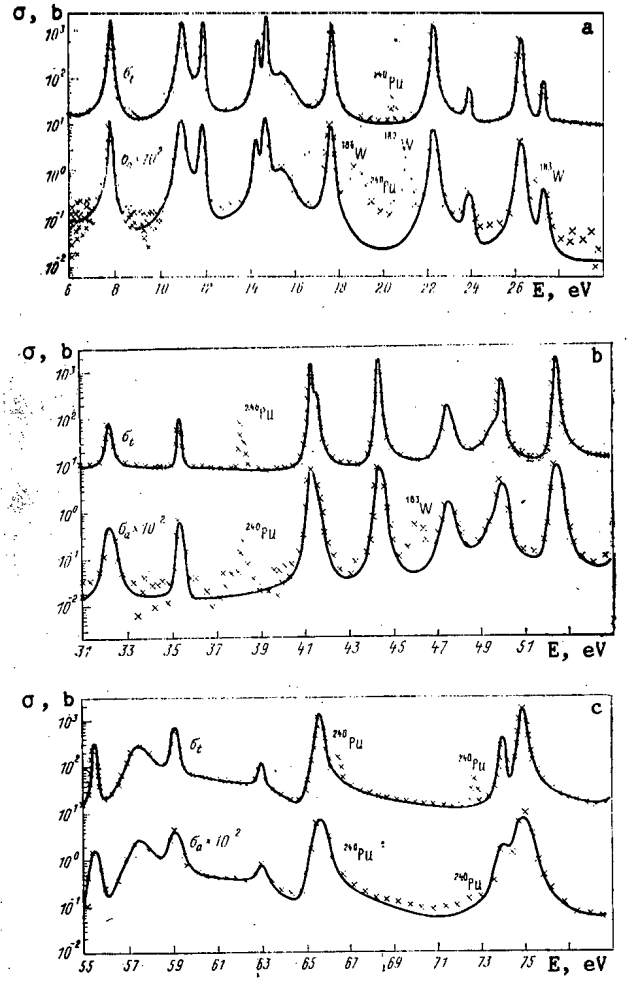


Fig. 1. Total cross section $\sigma_t$ and absorption cross section $\sigma_a$ of $^{239}Pu$ in the range 6-80 eV: ×) experiment [3, 5]; ——) calculation.

1 shows that the values of the cross sections calculated with these parameters are in good agreement with experiment.

By analyzing the total cross section it was possible to obtain the resonance widths $\Gamma^0_{mn}$ for the idenification of levels by spin (for $^{239}Pu$ at low energies these are the levels with $J = 0^+$ amd $1^+$). Knowing the phases of potential scattering $\varphi_{nJ}$ (under the assumption $\varphi_{n0} = \varphi_{n1} = \varphi$), we can also find directly the neutron resonance absorption cross section. By using the fact that the collision matrix is unitary, we can express the total reaction cross section in terms of the diagonal element $U^J_{nn}$ in the form [1]:

$$\sigma_a(E) = \pi k^{-2} \sum_J g(J)(1 - |U^J_{nn}(E)|^2) = \frac{\pi}{k^2} \sqrt{E} \sum_J \sum_{m(J)} \frac{G^a_m \nu_m + H^a_m (\mu_m - E)}{(\mu_m - E)^2 + \nu_m^2}, \quad (4)$$

where

$$G^a_m + iH^a_m = 2g(J) \left( \Gamma^0_{mn} - i \sqrt{E} \sum_{m'(J)} \frac{\Gamma^0_{mn} \Gamma^{0*}_{m'n}}{E^*_{m'} - E_m} \right). \quad (5)$$

Expressing $\Gamma^0_{mn}$ in terms of the parameters $G_m$ and $H_m$ (3) obtained from a multilevel analysis of the total cross section, we obtain a simple formula for calculating the resonance parameters of the absorption cross section:

$$G^a_m + iH^a_m = (G_m + iH_m) e^{2i\varphi} - i \frac{\sqrt{E}}{2g(J)} \sum_{m'(J)} \times \frac{(G_m G_{m'} + H_m H_{m'}) + i(H_m G_{m'} - H_{m'} G_m)}{(\mu_{m'} - \mu_m) + i(\nu_{m'} + \nu_m)}. \quad (6)$$

In order to compare our results with data on the direct measurements of the $^{239}$PU absorption cross section in the region of resolved resonances [5], we averged the cross section $\sigma_a(E)$ (4) calculated with the parameters $G_m^a$ and $H_m^a$ with a Gaussian distribution, taking account of both the actual experimental distribution and the Doppler broadening of the resonances [4]. The calculated and experimental values are in good agreement below 80 eV (Fig. 1).

We note that because of the relatively poor resolution in the direct experimental measurement of $\sigma_a(E)$, the resonance parameters determined from these data are appreciably less accurate than our values obtained by using only the total cross section, which was measured with high resolution. The method proposed can also be used to calculate the cross section for the elastic scattering of neutrons.

## LITERATURE CITED

1. A. A. Luk'yanov, The Structure of Neutron Cross Sections [in Russian], Atomizdat, Moscow (1978).
2. D. Adler and F. Adler, in: Proc. Conf. on Breeding in Large Fast Reactors, Argonne, ANL-6792 (1963), p. 695.
3. H. Derrien, J. Blons, C. Eggermann, et al., in: Proc. IAEA Conf. on Nuclear Data for Reactors, Vol. 2, Paris (1966), p. 195.
4. V. V. Kolesov, A. A. Lyk'yanov, "Parameters of a multilevel analysis of the $^{239}$Pu cross sections in the resonance region," Preprint FÉI-1404, Obninsk (1983).
5. R. Gwin, E. Silver, R. Ingle, and H. Weaver, Nucl. Sci. Eng., 59, No. 2, 79 (1976).

**MEASUREMENT TECHNIQUES**
*Izmeritel'naya Tekhnika*
Vol. 27, 1984 (12 issues) ..... $520

**MECHANICS OF COMPOSITE MATERIALS**
*Mekhanika Kompozitnykh Materialov*
Vol. 20, 1984 (6 issues) ..... $430

**METAL SCIENCE AND HEAT TREATMENT**
*Metallovedenie i Termicheskaya Obrabotka Metallov*
Vol. 26, 1984 (12 issues) ..... $540

**METALLURGIST**
*Metallurg*
Vol. 28, 1984 (12 issues) ..... $555

**PROBLEMS OF INFORMATION TRANSMISSION**
*Problemy Peredachi Informatsii*
Vol. 20, 1984 (4 issues) ..... $420

**PROGRAMMING AND COMPUTER SOFTWARE**
*Programmirovanie*
Vol. 10, 1984 (6 issues) ..... $175

**PROTECTION OF METALS**
*Zashchita Metallov*
Vol. 20, 1984 (6 issues) ..... $480

**RADIOPHYSICS AND QUANTUM ELECTRONICS**
*Izvestiya Vysshikh Uchebnykh Zavedenii, Radiofizika*
Vol. 27, 1984 (12 issues) ..... $520

**REFRACTORIES**
*Ogneupory*
Vol. 25, 1984 (12 issues) ..... $480

**SIBERIAN MATHEMATICAL JOURNAL**
*Sibirskii Matematicheskii Zhurnal*
Vol. 25, 1984 (6 issues) ..... $625

**SOIL MECHANICS AND FOUNDATION ENGINEERING**
*Osnovaniya, Fundamenty i Mekhanika Gruntov*
Vol. 21, 1984 (6 issues) ..... $500

**SOLAR SYSTEM RESEARCH**
*Astronomicheskii Vestnik*
Vol. 18, 1984 (6 issues) ..... $365

**SOVIET APPLIED MECHANICS**
*Prikladnaya Mekhanika*
Vol. 20, 1984 (12 issues) ..... $520

**SOVIET ATOMIC ENERGY**
*Atomnaya Énergiya*
Vols. 56-57, 1984 (12 issues) ..... $560

**SOVIET JOURNAL OF GLASS PHYSICS AND CHEMISTRY**
*Fizika i Khimiya Stekla*
Vol. 10, 1984 (6 issues) ..... $235

**SOVIET JOURNAL OF NONDESTRUCTIVE TESTING**
*Defektoskopiya*
Vol. 20, 1984 (12 issues) ..... $615

**SOVIET MATERIALS SCIENCE**
*Fiziko-khimicheskaya Mekhanika Materialov*
Vol. 20, 1984 (6 issues) ..... $445

**SOVIET MICROELECTRONICS**
*Mikroèlektronika*
Vol. 13, 1984 (6 issues) ..... $255

**SOVIET MINING SCIENCE**
*Fiziko-tekhnicheskie Problemy Razrabotki Poleznykh Iskopaemykh*
Vol. 20, 1984 (6 issues) ..... $540

**SOVIET PHYSICS JOURNAL**
*Izvestiya Vysshikh Uchebnykh Zavedenii, Fizika*
Vol. 27, 1984 (12 issues) ..... $520

**SOVIET POWDER METALLURGY AND METAL CERAMICS**
*Poroshkovaya Metallurgiya*
Vol. 23, 1984 (12 issues) ..... $555

**STRENGTH OF MATERIALS**
*Problemy Prochnosti*
Vol. 16, 1984 (12 issues) ..... $625

**THEORETICAL AND MATHEMATICAL PHYSICS**
*Teoreticheskaya i Matematicheskaya Fizika*
Vol. 58-61, 1984 (12 issues) ..... $500

**UKRAINIAN MATHEMATICAL JOURNAL**
*Ukrainskii Matematicheskii Zhurnal*
Vol. 36, 1984 (6 issues) ..... $500

**Send for Your Free Examination Copy**

**Plenum Publishing Corporation,** 233 Spring St., New York, N.Y. 10013
In United Kingdom: 88/90 Middlesex St., London E1 7EZ, England
Prices slightly higher outside the U.S. Prices subject to change without notice.

# RUSSIAN JOURNALS IN THE PHYSICAL AND MATHEMATICAL SCIENCES

## AVAILABLE IN ENGLISH TRANSLATION

**ALGEBRA AND LOGIC**
*Algebra i Logika*
Vol. 23, 1984 (6 issues) ..... $360

**ASTROPHYSICS**
*Astrofizika*
Vol. 20, 1984 (4 issues) ..... $420

**AUTOMATION AND REMOTE CONTROL**
*Avtomatika i Telemekhanika*
Vol. 45, 1984 (24 issues) ..... $625

**COMBUSTION, EXPLOSION, AND SHOCK WAVES**
*Fizika Goreniya i Vzryva*
Vol. 20, 1984 (6 issues) ..... $445

**COSMIC RESEARCH**
*Kosmicheskie Issledovaniya*
Vol. 22, 1984 (6 issues) ..... $545

**CYBERNETICS**
*Kibernetika*
Vol. 20, 1984 (6 issues) ..... $445

**DIFFERENTIAL EQUATIONS**
*Differentsial'nye Uravneniya*
Vol. 20, 1984 (12 issues) ..... $505

**DOKLADY BIOPHYSICS**
*Doklady Akademii Nauk SSSR*
Vols. 274-279, 1984 (2 issues) ..... $145

**FLUID DYNAMICS**
*Izvestiya Akademii Nauk SSSR, Mekhanika Zhidkosti i Gaza*
Vol. 19, 1984 (6 issues) ..... $500

**FUNCTIONAL ANALYSIS AND ITS APPLICATIONS**
*Funktsional'nyi Analiz i Ego Prilozheniya*
Vol. 18, 1984 (4 issues) ..... $410

**GLASS AND CERAMICS**
*Steklo i Keramika*
Vol. 41, 1984 (6 issues) ..... $590

**HIGH TEMPERATURE**
*Teplofizika Vysokikh Temperatur*
Vol. 22, 1984 (6 issues) ..... $520

**HYDROTECHNICAL CONSTRUCTION**
*Gidrotekhnicheskoe Stroitel'stvo*
Vol. 18, 1984 (12 issues) ..... $385

**INDUSTRIAL LABORATORY**
*Zavodskaya Laboratoriya*
Vol. 50, 1984 (12 issues) ..... $520

**INSTRUMENTS AND EXPERIMENTAL TECHNIQUES**
*Pribory i Tekhnika Eksperimenta*
Vol. 27, 1984 (12 issues) ..... $590

**JOURNAL OF APPLIED MECHANICS AND TECHNICAL PHYSICS**
*Zhurnal Prikladnoi Mekhaniki i Tekhnicheskoi Fiziki*
Vol. 25, 1984 (6 issues) ..... $540

**JOURNAL OF APPLIED SPECTROSCOPY**
*Zhurnal Prikladnoi Spektroskopii*
Vols. 40-41, 1984 (12 issues) ..... $540

**JOURNAL OF ENGINEERING PHYSICS**
*Inzhenerno-fizicheskii Zhurnal*
Vols. 46-47, 1984 (12 issues) ..... $540

**JOURNAL OF SOVIET LASER RESEARCH**
*A translation of articles based on the best Soviet research in the field of lasers*
Vol. 5, 1984 (6 issues) ..... $180

**JOURNAL OF SOVIET MATHEMATICS**
*A translation of Itogi Nauki i Tekhniki* and *Zapiski Nauchnykh Seminarov Leningradskogo Otdeleniya Matematicheskogo Instituta im. V. A. Steklova AN SSSR*
Vols. 24-27, 1984 (24 issues) ..... $1035

**LITHOLOGY AND MINERAL RESOURCES**
*Litologiya i Poleznye Iskopaemye*
Vol. 19, 1984 (6 issues) ..... $540

**LITHUANIAN MATHEMATICAL JOURNAL**
*Litovskii Matematicheskii Sbornik*
Vol. 24, 1984 (4 issues) ..... $255

**MAGNETOHYDRODYNAMICS**
*Magnitnaya Gidrodinamika*
Vol. 20, 1984 (4 issues) ..... $415

**MATHEMATICAL NOTES**
*Matematicheskie Zametki*
Vols. 35-36, 1984 (12 issues) ..... $520

*continued on inside back cover*